

Pedro V. Marcal · Nobuki Yamagata
Editors

Design and Analysis of Reinforced Fiber Composites

Design and Analysis of Reinforced Fiber Composites

Pedro V. Marcal • Nobuki Yamagata
Editors

Design and Analysis of Reinforced Fiber Composites

 Springer

Editors

Pedro V. Marcal
Oak Park
California, USA

Nobuki Yamagata
Yokohama, Japan

ISBN 978-3-319-20006-4 ISBN 978-3-319-20007-1 (eBook)
DOI 10.1007/978-3-319-20007-1

Library of Congress Control Number: 2015946984

Springer Cham Heidelberg New York Dordrecht London
© Springer International Publishing Switzerland 2016

This work is subject to copyright. All rights are reserved by the Publisher, whether the whole or part of the material is concerned, specifically the rights of translation, reprinting, reuse of illustrations, recitation, broadcasting, reproduction on microfilms or in any other physical way, and transmission or information storage and retrieval, electronic adaptation, computer software, or by similar or dissimilar methodology now known or hereafter developed.

The use of general descriptive names, registered names, trademarks, service marks, etc. in this publication does not imply, even in the absence of a specific statement, that such names are exempt from the relevant protective laws and regulations and therefore free for general use.

The publisher, the authors and the editors are safe to assume that the advice and information in this book are believed to be true and accurate at the date of publication. Neither the publisher nor the authors or the editors give a warranty, express or implied, with respect to the material contained herein or for any errors or omissions that may have been made.

Printed on acid-free paper

Springer International Publishing AG Switzerland is part of Springer Science+Business Media
(www.springer.com)

Preface

In the summer of 2014, and at the WCCM in Barcelona, we tried to capture the current state of the art in the “Design and Analysis of Reinforced Fiber Composites”. We were hoping to draw together a set of authors who would guide practitioners as well as researchers toward an integrated view of the subject. The international response to our call for papers exceeded our wildest expectations by addressing the important questions that we wanted to learn about and that was not widely discussed in the literature. Thus, we had papers concerned with the causes of delamination during buckling, manufacturing with natural fibers, the design of composite Pressure Vessels, analysis of large strain fiber and matrix behavior in tires, Macro Models for efficient analysis of Fracture, and application of SPH methods combined with MRI in model preparation, respectively.

The discussions to the presentations showed a large degree of interest. We wish that we could have collected the discussions and included it as an appendix to this volume. Alas my secretarial skills were not up to the task. We are indebted to our colleagues who kindly agreed to contribute to this Collection and who have modified their papers to reflect the points raised in the discussions.

We are indebted to Ms Silvia Schilgerius and Ms Kay Stoll, both of Springer, for originally suggesting this Collection and invaluable assistance throughout the publication process.

Los Angeles, CA
Yokohama, Japan

Pedro V. Marcal
Nobuki Yamagata

Contents

Buckling Analysis of Grid-Stiffened Composite Shells	1
Dan Wang and Mostafa Abdalla	
Three-Dimensional Image Processing Applied to the Characterization of Lightweight Mortar Reinforced with <i>Piassaba</i> Fibers	19
Susana M. Iglesias, Helder C. Almeida, Dany S. Dominguez, and Jorge F.L. Santos	
Computational Modeling of Fiber Composites with Thick Fibers as Homogeneous Structures with Use of Couple Stress Theory	25
Svitlana Fedorova, Tomáš Lasota, and Jiří Burša	
Towards Fiber Bundle Models for Composite Pressure Vessels	49
Jörg B. Multhoff	
A Macro Model for 3D Fiber-Reinforced Polymer Composites	67
Pedro V. Marcal, Jeffrey T. Fong, and Nobuki Yamagata	
Modeling and SPH Analysis of Composite Materials	87
Nobuki Yamagata, Yuzuru Sakai, and Pedro V. Marcal	

Buckling Analysis of Grid-Stiffened Composite Shells

Dan Wang and Mostafa Abdalla

Abstract There is a renewed interest in grid-stiffened composite structures; they are not only competitive with conventional stiffened constructions and sandwich shells in terms of weight but also enjoy superior damage tolerance properties. In this chapter, both global and local structural instabilities are investigated for grid-stiffened composite panels using homogenization theory. Characteristic cell configurations with periodic boundary constraints are employed for orthogrid- and isogrid-stiffened shells in order to smear the stiffened panel into an equivalent unstiffened shell. Homogenized properties corresponding to classical lamination theory are obtained by matching the strain energy of the stiffened and equivalent cells. Global buckling analysis is carried out based on the homogenized shell properties. Bloch wave theory is adopted to calculate the local buckling load of grid-stiffened shells, where the interaction of adjacent cells is fully taken into account. Moreover, instead of considering skin buckling and stiffener crippling separately, as is commonly done, the skin and stiffeners are assembled together at the level of the characteristic cell. The critical instabilities can be captured whether they are related to the skin or stiffener or their interaction. The proposed combination of global/local models can also be used to predict the material failure of a structure. Numerical examples of orthogrid- and isogrid-stiffened isotropic panels show that the local buckling loads predicted by the proposed method match finite element calculations better than semi-analytical methods based on assumptions and idealizations. The proposed method is further validated using typical configurations of flat composite panels and circular composite cylinders.

1 Introduction

Due to the advantages of lightweight, small manufacturing cost, high strength, high stability, great energy absorption, and superior damage tolerance [1–4], grid-stiffened composite panels have been applied in aerospace engineering for payload

D. Wang (✉) • M. Abdalla
Delft University of Technology, 2629 HS Delft, The Netherlands
e-mail: d.wang@tudelft.nl; m.m.abdalla@tudelft.nl

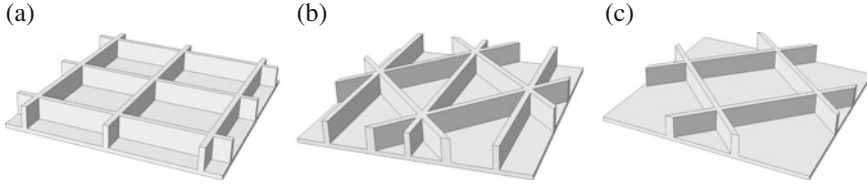


Fig. 1 Basic types of grid-stiffened panels. (a) Orthogrid. (b) Isogrid. (c) Anglegrid

fairings of launch vehicles and for load-bearing structures of satellites. Usually, three basic types of grids, i.e., isogrid, orthogrid, and angle grid, as shown in Fig. 1, are used in practical applications.

Many researchers have devoted themselves to studying grid-stiffened composite panels [5–9]. The discrete stiffener and the smeared stiffener methods are two main methods used to study behavior of such structures. With the detailed geometry retained, the discrete stiffener method, where the skin and stiffeners are modeled separately with the compatibility maintained at the interface [7], has the ability to capture both global and local behavior and guarantee high accuracy [8]. However, using the detailed geometry is not only computationally expensive for large structures but also precludes the application of the discrete method in downstream design optimization due to the difficulty of automatic remeshing for changeable geometry. Instead, the smeared stiffener method, where a grid-stiffened structure is represented by an equivalent homogeneous panel, only involves simple geometry without any detailed geometric information and therefore leads to better computational efficiency and provides a flexible and suitable interface with design optimization. However, as proved by researchers [8], the smeared stiffener method is only accurate for calculating global buckling and deficient for local buckling.

Homogenization theory has been widely used in calculating effective properties of a heterogeneous medium. By using asymptotic expansions and the assumption of periodicity, physical quantities can be evaluated on two different levels: the macroscopic and microscopic, where the former implies slow variation and the latter implies rapid oscillations [10]. Two different families of numerical methods based on Finite Element Method and Fast Fourier Transforms, respectively, were compared to obtain the effective properties of composites with periodic microstructure [11]. In this work, two specific features of periodic homogenization including periodicity conditions and strain or stress control were presented in detail. As an extension of a homogeneous Love–Kirchhoff model [12], a homogenized Reissner–Mindlin model with the shear effects of thick plates taken into account was proposed, where the shear constants were determined by an auxiliary 3D boundary value problem [13]. Using the full gradient of the bending moment instead of only the mixed shear forces, the Bending-Gradient theory [14, 15] took advantage of the higher accuracy of both deflection and local stresses than the Reissner–Mindlin theory for heterogeneous plates and was further applied to a folded core sandwich panel [16] and a periodic beam lattice [17].

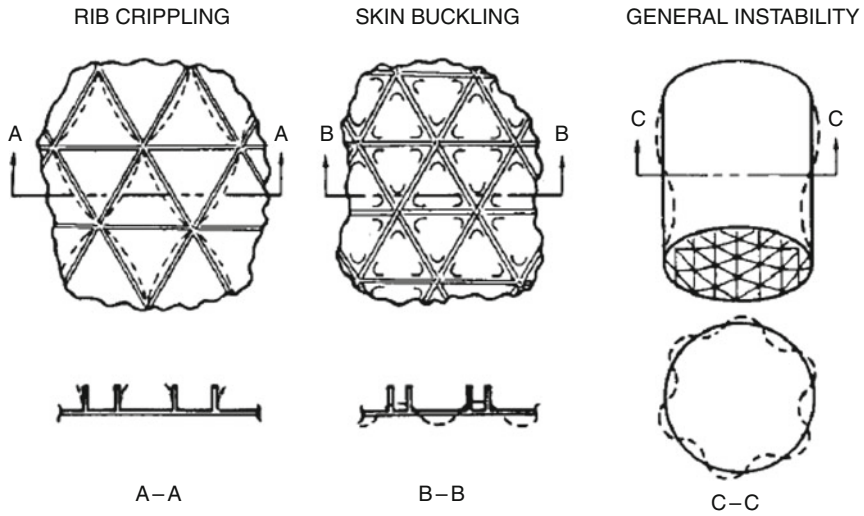


Fig. 2 Buckling modes of grid-stiffened panels [6]

Grid-stiffened panels may fail in three different modes of rib/stiffener crippling, skin buckling, and global buckling, as shown in Fig. 2, where the former two are known as local buckling. To increase its service life, a grid-stiffened structure is usually designed to localize buckling to ensure that global buckling happens after local buckling. Practically, global buckling loads of grid-stiffened panels are usually assessed using the smeared method, while local buckling loads are predicted approximately with boundary conditions properly assumed at the interface of skin and stiffeners. The global buckling load for an axial compressed cylinder was obtained in a closed form for classical simply supported ends, while for the case of a combined axial compression and torsion, the global buckling problem was formulated using the Galerkin approach [6]. Moreover, with the assumption of a simple support at the stiffener/skin attachment, the skin buckling was calculated with the skin cell simply supported along its edges, and the stiffener crippling was calculated with a clamped fixity condition imposed at the nodes. Weber and Middendorf [18] integrated the interaction between adjacent skin fields into the calculation of the local skin buckling load by applying periodic boundary conditions at opposite panel edges. Both global and local buckling behaviors were considered in a weight-minimum design for grid-stiffened panels and cylinders using a genetic algorithm [19, 20]. In the work, an improved smeared theory with the offset effect of stiffeners included [21] was employed for the global analysis, while the local skin buckling was assessed by the Rayleigh–Ritz method which accounts for material anisotropy, and stiffener crippling was assessed using the method provided in Reddy’s work [6]. Then, this method was applied to optimization design of grid-stiffened panels with variable curvature, which were modeled as assemblies of panels with constant curvature [22]. To carry out an optimization design for

aircraft wing rib panels, global bucking, stiffener crippling, and material failure were evaluated using the Lagrange multiplier method, the assumption that the stiffener blade was an axially loaded rectangular plate and a maximum strain failure criterion, respectively [23]. A hybrid model was proposed [24] with elements around the loading node of a smeared panel replaced by the detailed rib and skin elements to obtain a refined stress analysis, which could also take hygrothermal behavior and local buckling into account.

A different approach to calculate local instability in periodic media is furnished by Bloch's wave theory. In the Bloch wave theory, the displacement of a particle in a periodic medium could be represented as a product of a periodic component with the same periodicity as the medium and periodic function with an arbitrary wavelength. According to this special representation, wave propagation in periodic beams and stiffened plates was evaluated [25, 26]. Then, it was proved that the Bloch wave theory had the ability to determine the onset of instability in periodic solids [27]. A great body of related work was done by Triantafyllidis and coworkers [4, 28–31] to investigate critical material instability in periodic solids. In their work, concepts of a micro-failure surface and a macro-failure surface were introduced to describe the locus of first microscopic bifurcation points and points with a macroscopic loss of ellipticity, respectively. The distinction between onsets of microscopic and macroscopic material instability is whether the wavelength is commensurate with the unit cell dimension or not. Research has showed that the micro-failure surface of an infinite perfectly periodic structure is a lower bound of that of a finite structure and an upper bound of that of a finite structure with imperfections [30]. Applications of the Bloch wave theory in two-dimensional periodic composites showed that the interstitial stiffness had an important influence on the nature of the critical failure mode [28]. Similar work has been done by Ohno and coworkers [32, 33] to establish the critical states for square honeycombs and Kelvin cell foams under compression loadings.

As clearly illustrated in references [34, 35], existing methods based on the Bloch wave theory focus on material failure where the material deforms inside the plane as a failure mode. In this chapter, the out-of-plane instability of grid-stiffened panels is characterized by the Bloch wave theory. In contrast to the existing methods used to detect material failure, only local instability can be investigated in this case, while global instability is evaluated using the equivalent unstiffened panel with average material properties.

The rest of this chapter is devoted to a description of the homogenization approach and the use of Bloch's wave theory in detecting local instability of grid-stiffened structure. Section 3 presents an overview of the homogenization approach and the smearing process of a grid-stiffened panel. Section 4 develops the Bloch wave theory and reduces the computation to a symmetric generalized eigenvalue problem. Section 5 presents a number of numerical examples of flat and curved grid-stiffened structures and comparison to published results and detailed finite element calculations. Finally, Sect. 5 provides conclusions.

2 Homogenization of a Grid-Stiffened Composite Panel

2.1 Homogenization Theory

According to the homogenization theory for media with periodic structures [10], the grid-stiffened panel can be investigated using a double-scale scheme. From the macroscopic perspective, the whole structure can be treated as a homogenous panel without any stiffener. Displacements are assumed to be smooth and change slowly over one cell from the macroscopic perspective. From the microscopic perspective, the displacement will have a significant, but smaller amplitude, variation over one cell. Therefore, the displacement can be represented in the following expression as a function of two scales. For the out-of-plane deflection, we have:

$$w(\mathbf{x}) = w_0(\mathbf{x}) + \eta w_1(\mathbf{x}, \mathbf{y}) + \eta^2 w_2(\mathbf{x}, \mathbf{y}) + \dots \quad (1)$$

where $\mathbf{y} = \mathbf{x}/\eta$, and η is a small parameter representing the ratio of cell dimension to the dimension of the solid.

Correspondingly, the curvature vector can be expressed as:

$$w_{,xx}(\mathbf{x}) = \frac{1}{\eta} w_{1,yy}(\mathbf{x}, \mathbf{y}) + (w_{0,xx}(\mathbf{x}) + w_{2,yy}(\mathbf{x}, \mathbf{y})) + \eta (w_{1,xx}(\mathbf{x}, \mathbf{y}) + w_{3,yy}(\mathbf{x}, \mathbf{y})) + \dots \quad (2)$$

For the above equation, if $w_{1,yy} \neq \mathbf{0}$, the first item in the right part of that equation will become unbounded as $\eta \rightarrow 0$. Therefore, we require $w_1 = 0$ and Eq. (2) can be rewritten as:

$$\boldsymbol{\kappa}(\mathbf{x}) = \boldsymbol{\kappa}_0(\mathbf{x}) + \boldsymbol{\kappa}_1(\mathbf{x}, \mathbf{y}) + \eta \boldsymbol{\kappa}_2(\mathbf{x}, \mathbf{y}) + \dots \quad (3)$$

where $\boldsymbol{\kappa}_0$ is the curvature due to the macroscopic variation and $\boldsymbol{\kappa}_1$ due to the microscopic variation. Higher order terms will not be considered in this work.

Similarly, the in-plane displacement is represented as:

$$\mathbf{u}(\mathbf{x}) = \mathbf{u}_0(\mathbf{x}) + \eta \mathbf{u}_1(\mathbf{x}, \mathbf{y}) + \eta^2 \mathbf{u}_2(\mathbf{x}, \mathbf{y}) + \dots \quad (4)$$

and the corresponding strains:

$$\boldsymbol{\varepsilon}(\mathbf{x}) = \boldsymbol{\varepsilon}_0(\mathbf{x}) + \boldsymbol{\varepsilon}_1(\mathbf{x}, \mathbf{y}) + \eta \boldsymbol{\varepsilon}_2(\mathbf{x}, \mathbf{y}) + \dots \quad (5)$$

The displacement fields $w_2(\mathbf{x}, \mathbf{y})$ and $\mathbf{u}_1(\mathbf{x}, \mathbf{y})$ are assumed to be periodic in \mathbf{y} .

2.2 Smearing Based on the Conservation of the Strain Energy

In the smeared stiffener method, a grid-stiffened panel is replaced with an equivalent homogeneous panel with uniform properties. The homogenization process is performed by equating the strain energy of the equivalent model to be the same as that of the detailed cell configuration.

For simplicity, consider a cell configuration periodic along the y_1 and y_2 directions. The cell average in-plane strains are given by:

$$\begin{cases} \varepsilon_{01} = u_{01,y_1} \\ \varepsilon_{02} = u_{02,y_2} \\ \gamma_{01y_2} = u_{01,y_2} + u_{02,y_1} \end{cases} \quad (6)$$

Therefore, these displacements can be represented analytically.

$$\begin{cases} u_{01} = \varepsilon_{01}y_1 + \frac{1}{2}\gamma_{012}y_2 + c_1 \\ u_{02} = \varepsilon_{02}y_2 + \frac{1}{2}\gamma_{012}y_1 + c_2 \end{cases} \quad (7)$$

Similarly, following compatible relations hold between average curvatures and the corresponding deflection u_{03} :

$$\begin{cases} \kappa_{01} = u_{03,y_1y_1} \\ \kappa_{02} = u_{03,y_2y_2} \\ \kappa_{012} = 2u_{03,y_1y_2} \end{cases} \quad (8)$$

The slowly varying out-of-plane deflection may be represented as follows:

$$\begin{aligned} u_{03} &= \frac{1}{2} \{y_1 \ y_2\} \begin{bmatrix} \kappa_{01} & \kappa_{012}/2 \\ \kappa_{012}/2 & \kappa_{02} \end{bmatrix} \begin{Bmatrix} y_1 \\ y_2 \end{Bmatrix} + c_3y_1 + c_4y_2 + c_5 \\ &= \frac{1}{2}(\kappa_{01}y_1^2 + \kappa_{02}y_2^2 + \kappa_{012}y_1y_2) + c_3y_1 + c_4y_2 + c_5 \end{aligned} \quad (9)$$

In the above expressions of Eqs. (7) and (9), items including constants c_1 , c_2 , and c_5 denote rigid body translations and items including constants c_3 and c_4 denote rigid body rotations, which have no contribution to the strain energy. Therefore, all these constants could be set to zero to simplify the expressions.

The rotations $\theta_{01} = u_{03,y_2}$, $\theta_{02} = -u_{03,y_1}$ are given by:

$$\begin{cases} \theta_{01} = \kappa_{02}y_2 + \frac{1}{2}\kappa_{012}y_1 \\ \theta_{02} = -\kappa_{01}y_1 - \frac{1}{2}\kappa_{012}y_2 \end{cases} \quad (10)$$

The periodic part of the displacement vector does not contribute to the difference in total displacement between corresponding nodes on opposite sides of a characteristic cell. Thus, the following boundary conditions apply:

$$\begin{cases} \Delta u_1 = \varepsilon_{01} \Delta y_1 + \frac{1}{2} \gamma_{012} \Delta y_2 \\ \Delta u_2 = \varepsilon_{02} \Delta y_2 + \frac{1}{2} \gamma_{012} \Delta y_1 \\ \Delta u_3 = \frac{1}{2} \kappa_{012} \Delta(y_1 y_2) \\ \Delta \theta_1 = \kappa_{02} \Delta y_2 + \frac{1}{2} \kappa_{012} \Delta y_1 \\ \Delta \theta_2 = -\kappa_{01} \Delta y_1 - \frac{1}{2} \kappa_{012} \Delta y_2 \end{cases} \quad (11)$$

Herein, the center of the cell is set to the origin of the coordinate system to simplify the equations.

The total strain energy is given by:

$$\mathcal{U} = \frac{1}{2} \int_{\Omega_c} \Gamma_0^T \mathbf{C} \Gamma_0 d\Omega_c \quad (12)$$

Here, $\Gamma_0 = \{\boldsymbol{\varepsilon}_0 \boldsymbol{\kappa}_0\}^T$ and symbol \mathbf{C} denotes the equivalent material stiffness matrix of the smeared panel.

The discrete version takes the form:

$$\mathcal{U} = \frac{1}{2} \mathbf{u}^T \mathbf{K} \mathbf{u} \quad (13)$$

By rewriting the displacement constraints of Eq. (11) in a matrix form $\mathbf{L} \mathbf{u} = \mathbf{D} \Gamma_0$, we can develop an augmented form of the potential energy for a system without any external force.

$$\Pi = \frac{1}{2} \mathbf{u}^T \mathbf{K} \mathbf{u} - \boldsymbol{\lambda}^T (\mathbf{L} \mathbf{u} - \mathbf{D} \Gamma_0) \quad (14)$$

Using the minimum potential energy principle, we have:

$$\begin{cases} \frac{\partial \Pi}{\partial \mathbf{u}} = \mathbf{K} \mathbf{u} - \mathbf{L}^T \boldsymbol{\lambda} = 0 \\ \frac{\partial \Pi}{\partial \boldsymbol{\lambda}} = \mathbf{L} \mathbf{u} - \mathbf{D} \Gamma_0 = 0 \end{cases} \quad (15)$$

which leads to

$$\begin{bmatrix} \mathbf{K} & \mathbf{L}^T \\ \mathbf{L} & \mathbf{0} \end{bmatrix} \begin{Bmatrix} \mathbf{u} \\ \boldsymbol{\lambda} \end{Bmatrix} = \begin{Bmatrix} \mathbf{0} \\ \mathbf{D} \end{Bmatrix} \Gamma_0 \quad (16)$$

Solving the above system with imposing strains and curvatures evaluated in the macroscopic level as “generalized loading” [11], displacements in the local region are obtained. Then, local stresses, which determines the material failure, can be acquired.

The solution of Eq.(16) takes the form of $\mathbf{u} = \mathbf{U}\Gamma_0$. With a combination of Eqs. (12) and (13) and a substitution of elementary strain and curvature states expressed by an unitary matrix into Eq. (12), the equivalent stiffness matrix of the smeared panel can be obtained via the following expression.

$$\mathbf{C}_{eff} = \frac{1}{A_c} \mathbf{U}^T \mathbf{K} \mathbf{U} \quad (17)$$

3 Local Buckling Prediction

For a characteristic cell of a grid-stiffened panel, the equilibrium of its finite element model could be expressed as follows:

$$\begin{bmatrix} \mathbf{K}_{1,1}^t & \mathbf{K}_{1,2:(n-1)}^t & \mathbf{K}_{1,n}^t \\ \mathbf{K}_{2:(n-1),1}^t & \mathbf{K}_{2:(n-1),2:(n-1)}^t & \mathbf{K}_{2:(n-1),n}^t \\ \mathbf{K}_{n,1}^t & \mathbf{K}_{2:(n-1),n}^t & \mathbf{K}_{n,n}^t \end{bmatrix} \begin{Bmatrix} \mathbf{u}_1 \\ \mathbf{u}_{2:(n-1)} \\ \mathbf{u}_n \end{Bmatrix} = \begin{Bmatrix} \mathbf{f}_1 \\ \mathbf{0} \\ \mathbf{f}_n \end{Bmatrix} \quad (18)$$

where \mathbf{K}^t is the tangent stiffness matrix. \mathbf{u} and \mathbf{f} are the displacement and force vectors, respectively. Subscripts 1 and n denote the starting part and the ending part of the periodic cell along the direction of the wave propagation, respectively.

According to the Bloch wave theory, displacement vectors of a point in a 2D periodic structure could be expressed in the following form [30]:

$$\mathbf{u}(y_1, y_2) = \tilde{\mathbf{u}}(y_1, y_2) \exp \left[i \left(\frac{m_1 y_1}{s_1} + \frac{m_2 y_2}{s_2} \right) \right] \quad (19)$$

where m_1 and m_2 are dimensionless wave numbers and s_1 and s_2 are the cell lengths along two different periodic axes. $\tilde{\mathbf{u}}(y_1, y_2)$ is a periodic function following the same cycle of a representative cell, which satisfies:

$$\tilde{\mathbf{u}}(y_1 + n_1 s_1, y_2 + n_2 s_2) = \tilde{\mathbf{u}}(y_1, y_2) \quad (20)$$

In the above equation, n_1 and n_2 are arbitrary integers.

The representation of \mathbf{u} in Eq. (19) implies the following relationship at the periodic boundaries:

$$\mathbf{u}_n = \boldsymbol{\mu}(e^{im_1}, e^{im_2}) \mathbf{u}_1 \quad (21)$$

Construct a matrix as follows:

$$\mathbf{L} = \{-\bar{\boldsymbol{\mu}} \mathbf{0} \mathbf{I}\}^T \quad (22)$$

where $\bar{\boldsymbol{\mu}}$ denotes the conjugate matrix of $\boldsymbol{\mu}$. Note that the matrix \mathbf{L} is identical to that used in the smearing process when the wave numbers are equal to zero. Then, the conjugate transpose matrix of \mathbf{L} could be expressed as:

$$\mathbf{L}^* = \{-\boldsymbol{\mu} \mathbf{0} \mathbf{I}\} \quad (23)$$

It is easy to conclude that:

$$\mathbf{L}^* \mathbf{u} = \mathbf{0} \quad (24)$$

The forces between boundary nodes on the opposite edges obey the same relationship as the displacements expressed by Eq. (21) but with opposite directions. Therefore, the following equation is satisfied.

$$\mathbf{f} = \mathbf{L} \mathbf{f}_n \quad (25)$$

With the substitution of Eqs. (24), (25), and (18) could be rewritten as [31]:

$$\begin{bmatrix} \mathbf{K}' & \mathbf{L} \\ \mathbf{L}^* & \mathbf{0} \end{bmatrix} \begin{Bmatrix} \mathbf{u} \\ -\mathbf{f}_n \end{Bmatrix} = \mathbf{0} \quad (26)$$

The generalized eigenvalues of the above equation are the buckling loads of the periodic panel. The minimum eigenvalue $\Lambda_m(m_1, m_2)$ for prescribed dimensionless wave numbers from $2n\pi$ to $(2n + 2)\pi$ defines the critical buckling load parameter surface, where n denotes a nonnegative integer. Due to the periodicity and symmetry, the range of m_1 and m_2 can be limited to $[0, \pi]$. Therefore, the critical buckling load defined as the minimum value of all the $\Lambda_m(m_1, m_2)$ satisfies the following equation [30].

$$\Lambda_c = \min_{0 \leq m_1, m_2 \leq \pi} \Lambda_m(m_1, m_2) \quad (27)$$

Actually, in contrast to periodic solid, a grid-stiffened thin-walled panel with infinite dimensions always buckles at zero, which belongs to global instability with a long wavelength. In this case, the local minimum value of Eq. (27) with the wave numbers far away from zero belongs to the range of a short wavelength, which is the local critical buckling load for a finite panel. The local buckling load of a finite grid-stiffened composite panel is obtained within this framework.

4 Numerical Examples

In this section, numerical examples are used to demonstrate the effectiveness of the proposed approach. First, the local buckling loads of an isotropic simply supported panel predicted by the proposed method are compared with those by a semi-analytic method [18]. Then, numerical predictions of the proposed method are presented for typical orthogrid- and isogrid-stiffened composite flat panels and circular cylinders. For the examples, detailed finite element models provide the basis for validating the accuracy of the proposed method.

4.1 A Flat Isotropic Panel

A comparison between local buckling loads of the proposed method and a semi-analytical skin buckling calculation method [18] is carried out in the example for orthogrid- and isogrid-stiffened isotropic panels under axial compression. In Weber and Middendorf's work, buckling load coefficients of both single panels with simply supported boundary conditions and skin fields with periodic boundary conditions imposed at opposite panel edges are provided. Except for the case of the rectangular panel under compression, there are evident differences between the results predicted by these two different assumptions. The results of both cases are considered in the comparison. The semi-analytical buckling results of the rectangular panel with clamped boundary conditions [36] are also included.

The different cell configurations involved for orthogrid and isogrid are illustrated in Fig. 3a and b, respectively. To eliminate the effect of dimensions and material properties, a dimensionless buckling load coefficient k is used with an expression as follows:

$$k = \frac{N_{cr}b^2}{\pi^2 D} \quad (28)$$

where

$$D = \frac{t^3 E}{12(1 - \nu^2)} \quad (29)$$

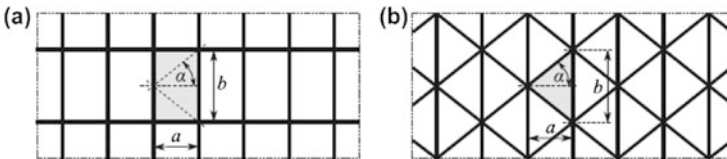


Fig. 3 Sketch of characteristic cell configurations of an isotropic panel [18]

In practice, there is no evident local buckling for a grid-stiffened panel with a small height of stiffeners. Numerically, there is no local minimum in the critical buckling load parameter surface detected for ratios of the stiffener height and the length of the panel less than a specific value. Investigations of the local buckling in this example are done for cell configurations with the height of the stiffeners changing from $0.12b$ to $0.52b$ and the width of the stiffener fixed to be $0.02b$. All the stiffeners are eccentrically located. Three typical aspect ratios a/b of 1.866, 1, and 0.289 are considered for the cell configuration in accordance with the reference [18]. As illustrated in Fig. 4, the semi-analytical methods with periodic boundary conditions and with clamped boundary conditions for orthogrid-stiffened panels under axial compression always provide the lower bound and the upper bound

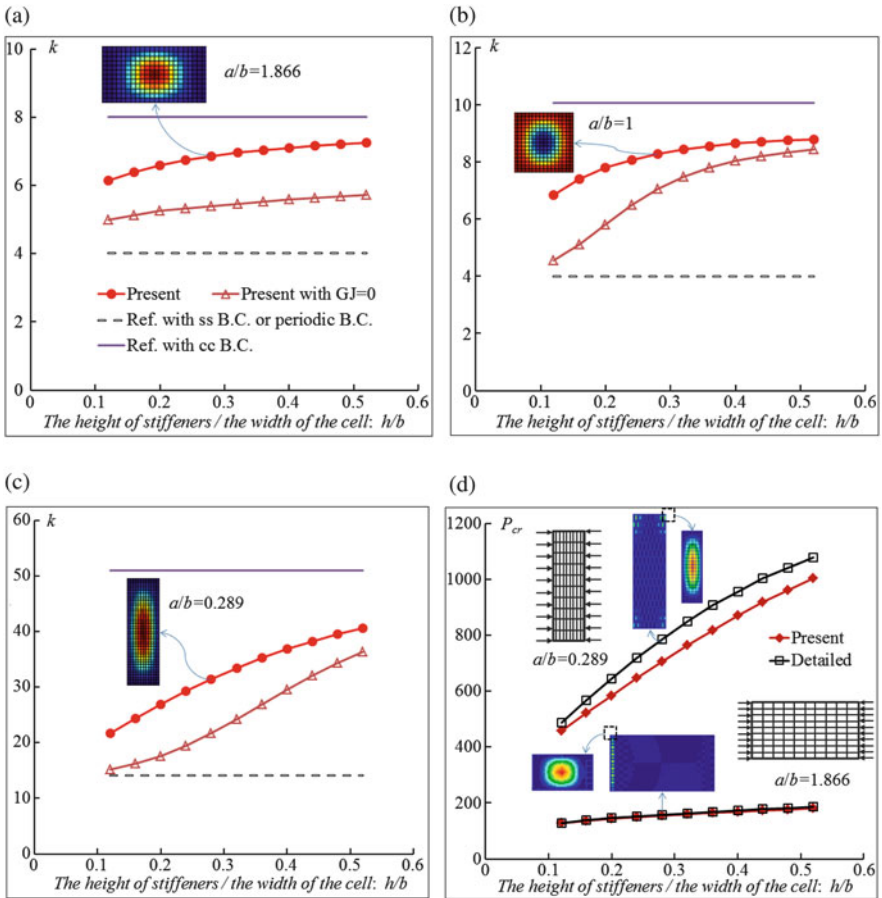


Fig. 4 A comparison between the skin local buckling predicted by the proposed method and the semi-analytical method of a flat orthogrid-stiffened isotropic panel under axial compression. (a) $a/b = 1.866$. (b) $a/b = 1$. (c) $a/b = 0.289$. (d) Validate the proposed method by the detailed finite element model

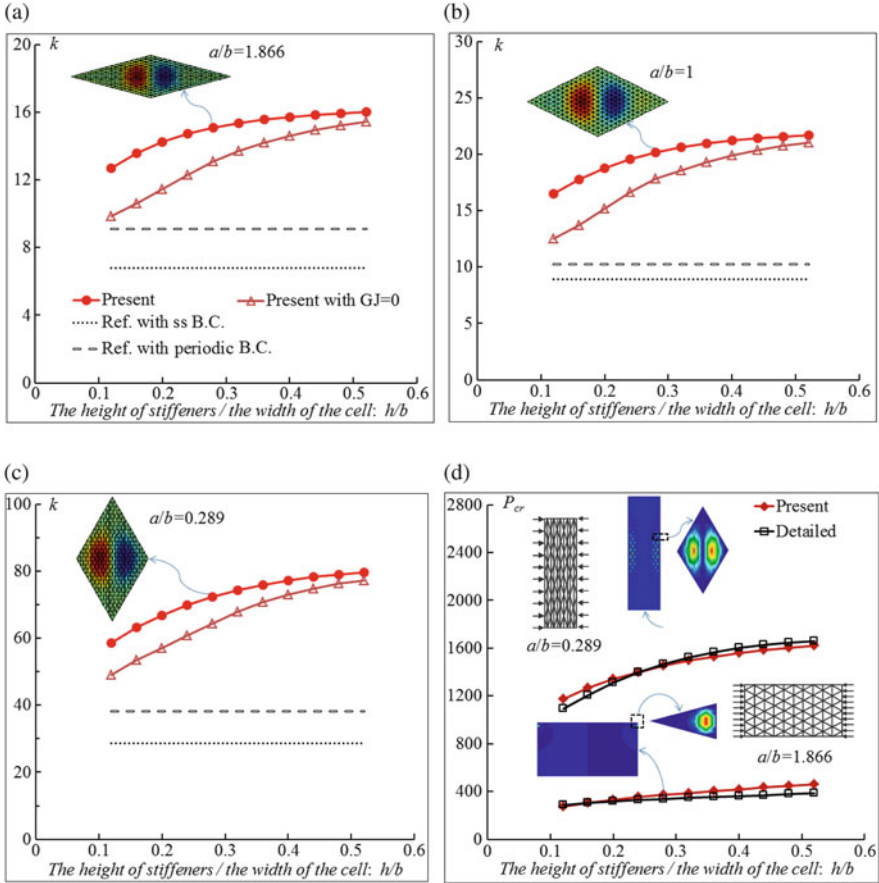


Fig. 5 A comparison between the skin local buckling predicted by the proposed method and the semi-analytical method of a flat isogrid-stiffened isotropic panel under axial compression. (a) $a/b = 1.866$. (b) $a/b = 1$. (c) $a/b = 0.289$. (d) Validate the proposed method by the detailed finite element model

bound of the skin buckling load coefficients predicted by the proposed method, respectively. In other words, the rectangular skin field under axial compression with the onset of local buckling predicted by the proposed method is always constrained with a boundary condition between simply supported and clamped, which can be concluded from both the values of the buckling load coefficients and the shape of the buckling modes.

A similar conclusion is drawn for the isogrid-stiffened panel, as illustrated in Fig. 5. It can be seen that results with the consideration of the interaction between adjacent skin fields provide a closer lower bound of the results predicted by the proposed method than those of simply supported boundary conditions. The torsional rigidity of the stiffeners ignored in the semi-analytical method takes a responsibility

of the difference between results of the proposed method and the semi-analytical method, which is proved by the results with $GJ = 0$.

As illustrated in Figs. 4d and 5d, local buckling loads of the orthogrid- and isogrid-stiffened panels under axial compression predicted by the proposed method are validated by the results of corresponding finite element models with detailed stiffeners for cell configurations with two extreme aspect ratios. The largest errors for the sampled orthogrid-stiffened panels with aspect ratios of 1.866 and 0.289 are -3% and -10% , respectively, while they are 20% and 8% for the sampled isogrid-stiffened panels. These errors are acceptable in practice. Moreover, the buckling modes obtained using the proposed method agree with those in a cell configuration of the detailed finite element models. All the detailed finite element models in this example employ a lattice with 16 cells in the width direction and 16 cells in the height direction, and the particular geometric and material parameters are as follows: the width of the cell configuration $b = 100$ mm, the skin thickness $t = 1$ mm, the width of the stiffeners $w = 2$ mm, the Young's modulus $E = 206.84$ GPa, and the Poisson's ratio $\nu = 1/3$.

From the comparisons, it can be concluded that the proposed method has the ability to predict the local buckling load of orthogrid- and isogrid-stiffened structures with stiffeners of different rigidities and the prediction results are more accurate than those calculated by the semi-analytical method with periodic boundary conditions, which have already been improved compared with those with simply supported boundary conditions.

4.2 A Flat Composite Panel

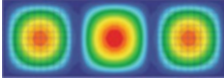
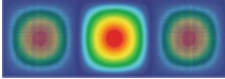
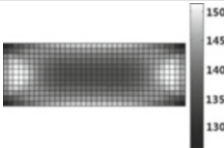

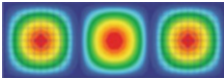
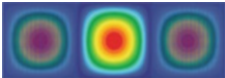


The example is a simply supported flat grid-stiffened composite panel, which represents a generic structural component of a transport helicopter fuselage, as studied in reference [20]. The flat panel with the length of 4376.4 mm and the width of 1587.7 mm is stiffened on one side by orthogrid or isogrid stiffeners. The skin laminate has an eight-ply symmetric layup of $(\pm 45/90/0)_s$ with each ply thickness being 0.1524 mm. The nominal ply mechanical properties are $E_{11} = 139.31$ GPa, $E_{22} = 13.103$ GPa, $G_{12} = G_{13} = G_{23} = 5.0345$ GPa, $\nu_{12} = 0.3$, and $\rho = 1590$ kg/mm³. All the stiffeners are made of 0-deg material with a height of $h = 12.9$ mm and a width of $w = 1.524$ mm.

The parameters of the grid-stiffened flat panel are given in Table 1. In the example, the angles between different stiffeners are set to be 60° for the isogrid

Table 1 Parameters of a grid-stiffened flat panel

Grid type	Dimensions of a cell: s_1/s_2 (mm)	No. of stiffeners		Weight of stiffeners (kg)
		Vertical	Horizontal	
Orthogrid	109.41/63.508	41	26	5.5917
Isogrid	136.58	38	–	5.5586

Table 2 Critical buckling loads of a grid-stiffened flat composite panel under compression

	Buckling	Proposed method	Detailed model	Error (%)
Orthogrid	Global			-0.2
		16.85	16.89	
	Local			-16.8
		126.61	152.15	
Isogrid	Global			4.5
		24.67	23.60	
	Local			12.3
		69.15	61.56	

cell configurations. The weights of the involved orthogrid- and isogrid-stiffened flat panels are very close.

To investigate the critical buckling loads, a unit uniaxial compression of 1 N/mm is considered. Both global and local buckling loads are given in Table 2. Local buckling behaviors predicted by the proposed method in Table 2 represent the distribution of local buckling loads. Compared with results of the detailed finite element model, global and local buckling loads predicted by the proposed method are within errors of 5 and 20 %, respectively, for the involved grid-stiffened panels.

4.3 A Composite Circular Cylinder

An orthogrid-stiffened composite circular cylinder with the diameter of 990 mm and the height of 1168 mm [6] is employed to investigate the critical buckling states of a cylinder under axial compression loading. The skin is made of AS4/3502 graphite/epoxy, while stiffeners are combinations of both AS4/3502 graphite/epoxy and filler. The mechanical properties of the skin and stiffeners are given in Table 3.

The cylinder with a skin thickness of 1.22 mm suffers from an axial compression of 175 N/mm. To ensure the uniform distribution of structural forces, clamped boundary conditions are used with radial displacements not fixed but coupled to

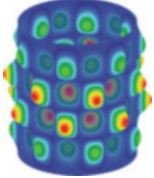
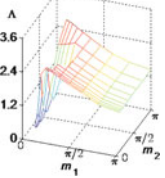
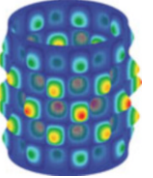
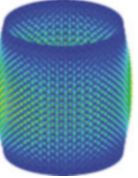
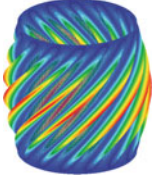
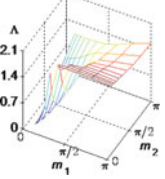
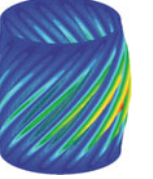
Table 3 Mechanical properties of grid-stiffened circular cylinders

	Skin	Stiffener
E_{11} : GPa	127.5	64.86
E_{22} : GPa	11.3	3.74
G_{12} : GPa	6	0.93
ν_{12}	0.3	0.3

Table 4 Dimensions of grid-stiffened circular cylinders

	Skin layup	No. of axial stiffeners/rings	Stiffeners: mm	
			Height	Width
Orthogrid	$(0, 90)_s$	90/20	6.35	1.7
	$(\pm 45)_s$	80/26	3.175	1.81

Table 5 Critical buckling loads of the orthogrid-stiffened circular cylinder

Skin layup	Buckling	Proposed method		Detailed model	
		Global	Local	Global	Local
$(0, 90)_s$	Mode				
	λ_c	1.1829	1.4356	1.1284	1.6426
	Error	4.8 %	-12.6 %		
$(\pm 45)_s$	Mode				—
	λ_c	0.9624	—	0.9283	—
	Error	3.7 %	—		

deform together for the top and bottom nodes, respectively. Two sets of dimensions of orthogrid-stiffened configurations are used corresponding to two different symmetric skin layups of $(0, 90)_s$ and $(\pm 45)_s$, as shown in Table 4.

Stability analysis of the involved composite circular cylinders is carried out using the proposed method. Both global and critical local buckling loads of these cylinders are calculated, and the results are provided in Table 5. The critical buckling load parameter surfaces with respect to dimensionless wave numbers are illustrated in items of the tables corresponding to local buckling behaviors obtained by the proposed method, where the local minimum represents the local buckling load.

As illustrated in Table 5, the errors of the global and local buckling loads using the proposed method are within 5 % and 15 %, respectively, compared with results of the detailed finite element model. Noticeably, in this case, the global buckling modes obtained by the proposed method are not exactly the same as those by the detailed finite element model. For cylinder buckling, the first few global buckling modes are different but their buckling loads are very close. These modes may happen at a different sequence for the proposed method and the detailed finite element method, which results in the difference between the critical global buckling modes. For the orthogrid-stiffened cylinder with a skin layup of $(\pm 45)_s$, local buckling does not exist since there is no local minimum in the critical buckling load parameter surface with respect to dimensionless wave numbers, as illustrated in Table 5. Actually, the local buckling is trivial in this case since the global buckling dominates the failure mode completely.

5 Conclusions

In this chapter, buckling analysis of periodically grid-stiffened composite plates and shells is studied. Both global and local buckling phenomena are taken into consideration. A smearing method based on homogenization theory is employed to calculate the equivalent material properties. Global buckling loads are obtained by buckling analysis of the smeared model. Local buckling loads are predicted by the Bloch wave theory. In contrast to applications of the Bloch wave theory in periodic solid to investigate in-plane material failure, the this chapter concentrates on local buckling of grid-stiffened structures where the critical load always goes to zero as the wave length is increased. Thus, the local minimum in dimensionless wave number space is considered to be the critical local buckling load. Because of the used detailed finite element model of the cell, with the skin and stiffeners assembled together, both the skin buckling and stiffener crippling are possible critical modes. There is no need for separate stability analysis of the stiffener and the skin. It is concluded from the comparisons between local buckling load coefficients of the proposed method and the semi-analytical method that the proposed method could predict the local buckling load more accurately than the semi-analytical method using periodic boundary conditions, while the latter always provide a lower bound of the former. Representative numerical examples of grid-stiffened flat composite panels and circular composite cylinders are employed to prove the effectiveness of the proposed method. Comparison with the results of the detailed finite element model indicates that local buckling loads predicted by the proposed method have an error within 20 % for compression loading.

References

1. Higgins, P. E. J., Wegner, P., Viisoreanu, A., & Sanford, G. E. (2004). Design and testing of the minotaur advanced grid-stiffened fairing. *Composite Structures*, 66, 339–349.
2. Huybrechts, S. M., Hahn, S. E., & Meink, T. E. E. (1999). Grid stiffened structures: A survey of fabrication, analysis and design methods. In *Proceedings of the 12th International Conference on Composite Materials (ICCM/12)*, Paris, France.
3. Jadhav, P., & Mantena, P. R. (2007). Parametric optimization of grid-stiffened composite panels for maximizing their performance under transverse loading. *Composite Structures*, 77, 353–363.
4. Schraad, M., & Triantafyllidis, N. (1997). Scale effects in media with periodic and nearly periodic microstructures - I. Macroscopic properties. *Journal of Applied Mechanics*, 64, 751–762.
5. Kassegne, S. K., & Reddy, J. N. (1998). Local behavior of discretely stiffened composite plates and cylindrical shells. *Composite Structures*, 41, 13–26.
6. Reddy, A. D., Valisetty, R. R., & Rehfield, L. W. (1985). Continuous filament wound composite concepts for aircraft fuselage structures. *Journal of Aircraft*, 22, 249–255.
7. Wang, J. T. S., & Hsu, T. M. (1985). Discrete analysis of stiffened composite cylindrical shells. *AIAA Journal*, 11, 1753–1761.
8. Wodesenbet, E., Kidane, S., & Pang, S. S. (2003). Optimization for buckling loads of grid stiffened composite panels. *Composite Structures*, 60, 159–169.
9. Zhang, Z. F., Chen, H. R. & Ye, L. (2011). A stiffened plate element model for advanced grid stiffened composite plates/shells. *Journal of Composite Materials*, 45, 187–202.
10. Hassani, B., & Hinton, E. (1998). A review of homogenization and topology optimization I-homogenization theory for media with periodic structure. *Computers & Structures*, 69, 707–717.
11. Michel, J. C., Moulinec, H., & Suquet, P. (1999). Effective properties of composite materials with periodic microstructure: A computational approach. *Computer Methods in Applied Mechanics and Engineering*, 172, 109–143.
12. Caillerie, D. (1984). Thin elastic and periodic plates. *Mathematical Methods in the Applied Sciences*, 6, 159–191.
13. Cecchi, A., & Sab, K. (2007). A homogenized Reissner-Mindlin model for orthotropic periodic plate: application to brickwork panels. *International Journal of Solids and Structures*, 44, 6055–6079.
14. Lebée, A., & Sab, K. (2011). A bending-gradient model for thick plates. Part I: Theory. *International Journal of Solids and Structures*, 48, 2878–2888.
15. Lebée, A., & Sab, K. (2011). A bending-gradient model for thick plates. Part II: Closed-form solutions for cylindrical bending of laminates. *International Journal of Solids and Structures*, 48, 2889–2901.
16. Lebée, A., & Sab, K. (2012). Homogenization of thick periodic plates: application of the Bending-Gradient plate theory to a folded core sandwich panel. *International Journal of Solids and Structures*, 49, 2778–2792.
17. Lebée, A., & Sab, K. (2013). Homogenization of a space frame as a thick plate: application of the Bending-Gradient plate theory to a beam lattice. *Computers & Structures*, 127, 88–101.
18. Weber, M. J., & Middendorf, P. (2014). Semi-analytical skin buckling of curved orthotropic grid-stiffened shells. *Composite Structures*, 108, 616–624.
19. Jaunky, N., Knight, Jr., N.F., & Ambur, D. R. (1998). Optimal design of general stiffened composite circular cylinders for global buckling with strength constraints. *Composite Structures*, 41, 243–252.
20. Jaunky, N., Knight, Jr., N. F. & Ambur, D. R. (1998). Optimal design of grid-stiffened composite panels using global and local buckling analyses. *Journal of Aircraft*, 35, 478–486.
21. Jaunky, N., Knight, Jr., N. F., & Ambur, D. R. (1996). Formulation of an improved smeared stiffener theory for buckling analysis of grid-stiffened composite panels. *Composites Part B: Engineering*, 27B, 519–526.

22. Ambur, D. R., & Jaunky, N. (2001). Optimal design of grid-stiffened panels and shells with variable curvature. *Composite Structures*, 52, 173–180.
23. Phillips, J. L., & Gürdal, Z. (1990). Analysis and optimum design of geodesically stiffened composite panels. In *Composite materials and design analysis* (pp. 509–528). Southampton: WIT Press.
24. Chen, H. J., & Tsai, S. W. (1995). Analysis and optimum design of composite grid structures. *Journal of Composite Materials*, 30, 503–533.
25. Mead, D. J. (1970). Free wave propagation in periodically supported infinite beams. *Journal of Sound and Vibration*, 11, 181–197.
26. Mead, D. J. (1986). A new method of analyzing wave propagation in periodic structures; applications to periodic Timoshenko beams and stiffened plates. *Journal of Sound and Vibration*, 104, 9–27.
27. Geymonat, G., Müller, S., & Triantafyllidis, N. (1993). Homogenization of nonlinearly elastic materials, microscopic bifurcation and macroscopic loss of rank-one convexity. *Archive for Rational Mechanics and Analysis*, 122, 231–291.
28. Triantafyllidis, N., & Schnaidt, W. C. (1993). Comparison of microscopic and macroscopic instabilities in a class of two-dimensional periodic composites. *Journal of the Mechanics and Physics of Solids*, 41, 1533–1565.
29. Triantafyllidis, N., & Bardenhagen, S. (1996). The influence of scale size on the stability of periodic solids and the role of associated higher order gradient continuum models. *Journal of the Mechanics and Physics of Solids*, 44, 1891–1928.
30. Schraad, M., & Triantafyllidis, N. (1997). Scale effects in media with periodic and nearly periodic microstructures - II. Failure mechanisms. *Journal of Applied Mechanics*, 64, 763–771.
31. Gong, L., Kyriakides, S., & Triantafyllidis, N. (2005). On the stability of Kelvin cell foams under compressive loads. *Journal of the Mechanics and Physics of Solids*, 53, 771–794.
32. Ohno, N., Okumura, D. & Niikawa, T. (2004). Long-wave buckling of elastic square honeycombs subject to in-plane biaxial compression. *International Journal of Mechanical Sciences*, 46, 1697–1713.
33. Okumura, D., Okada, A., & Ohno, N. (2008). Buckling behavior of Kelvin open-cell foams under [0 0 1], [0 1 1] and [1 1 1] compressive loads. *International Journal of Solids and Structures*, 45, 3807–3820.
34. Triantafyllidis, N., Nestorović, M. D., & Schraad, M. W. (2006). Failure surfaces for finitely strained two-phase periodic solids under general in-plane loading. *Journal of Applied Mechanics*, 73, 505–515.
35. Ohno, N., Okumura, D., & Noguchi, H. (2002). Microscopic symmetric bifurcation condition of cellular solids based on a homogenization theory of finite deformation. *Journal of the Mechanics and Physics of Solids*, 50, 1125–1153.
36. Galambos, T. V. (1998). *Guide to stability design criteria for metal structures* (5th ed.). New York: Wiley.

Three-Dimensional Image Processing Applied to the Characterization of Lightweight Mortar Reinforced with *Piassaba* Fibers

Susana M. Iglesias, Helder C. Almeida, Dany S. Dominguez,
and Jorge F.L. Santos

Abstract Among the solutions to solve the environmental problems caused by the industrial development and the urbanization growing is to reuse industrial waste in civil construction. In this work are characterized mixtures of lightweight mortar using ethylene-vinyl acetate (EVA) grains and *piassaba* fibers as aggregates. The EVA is a residue from footwear industry, and the *piassaba* fibers act as reinforcement material in the mixture. We propose a methodology that uses micro-tomographic and three-dimensional image processing to identify and quantify the aggregates, pores, and micro-cracks produced by mechanical stress in the samples. Results for four types of mixtures were analyzed. The present technique offers appropriated results for these mixtures.

1 Introduction

The environmental protection today is a goal and a concern for all areas of knowledge. Solutions for the reuse of industrial waste are now mandatory and recycling this waste in civil construction is one of the possibilities. Among the alternatives has the use of Ethylene-vinyl acetate (also known as EVA) from the footwear industry in lightweight mortar, in nonstructural parts [1]. EVA is a residue that has low density, large capacity to deform, good thermal, and acoustic characteristics. It can be used to develop a class of material that allows associating the functions of sealing and thermal comfort with lightness. However, studies have shown a reduction of mechanical strength when the EVA is added to the mortar mixture if compared to conventional mixtures. To solve this problem, an alternative

S.M. Iglesias (✉) • D.S. Dominguez • J.F.L. Santos
Programa de Pós-graduação em Modelagem Computacional, Universidade Estadual de Santa Cruz, Rod. Ilhéus-Itabuna km 16, Salobrinho, Ilhéus 45662-900, Bahia, Brazil
e-mail: smiglesias@uesc.br; dldominguez@gmail.com; jorgefabricio@ifba.edu.br

H.C. Almeida
Programa de Pós-graduação em Materiais, Universidade Estadual de Santa Cruz, Rod. Ilhéus-Itabuna km 16, Salobrinho, Ilhéus 45662-900, Bahia, Brazil
e-mail: helder.uesc@gmail.com

is using natural fibers in the mixture. In previous studies, it was shown that the addition of natural fibers improves the mechanical properties of the material. The fiber presence attenuates the stress propagation [2–4]. Among the natural fibers is the *piassaba* fiber from palm *Attalea funifera* Martius, broadly available in Southern Bahia, Brazil. In this work, lightweight concrete mixtures with EVA and *piassaba* fibers are analyzed.

To incorporate these new mixtures in civil construction, they should be featured in terms of their mechanical properties and internal structure. Generally the mechanical properties can be studied using mechanical tests as tensile and compressive tests. The internal structure can be characterized by nondestructive testing, such as ultrasound, microscopy, X-ray diffraction, and computed tomography. In this paper, we used micro-tomographic image processing techniques to study the internal structure of the material.

In previous works were made mechanical tests to characterize tensile stress and compression strength of this mixture (mortar + EVA + *piassaba*) [5]. Using two-dimensional image processing techniques, it was possible to identify the aggregates (there are EVA and *piassaba* fibers), pores, and micro-cracks in the study samples [6]. Still, the identification using two-dimensional images presents problems such as not considering the influence of fiber orientation. This work proposes the use of three-dimensional image processing to deepen the structural analysis of the lightweight mortar mixture reinforced with *piassaba* fibers improving the identification mechanism.

In the next section, the methodology used to study the lightweight mortar mixture is presented. In Sect. 3, are offered and discussed the results. The conclusions are shown in Sect. 4.

2 Methodology

In this work, four types of mixture were studied. The water/cement relation for all mixtures was 0.4, and the mass percentage of EVA and fibers for each type is shown in Table 1. These mixtures were used to prepare the samples. In these samples, the particle size distribution of EVA grains used varied from 850 to 1180 μm (16–20 mesh). The *piassaba* fibers were separated, cleaned, and cut with 10 mm length size. The sample preparation followed the Brazilian standard for fabrication and curing of cylindrical or prismatic concrete specimens (NBR 5738) [7].

Table 1 Characteristics of mixtures types

Mixture type	EVA (%)	Fiber (%)
(A) Pure mortar	0	0
(B) Mortar with EVA	1	0
(C) Mortar with EVA and fibers	1	1
(D) Mortar with fibers	0	1

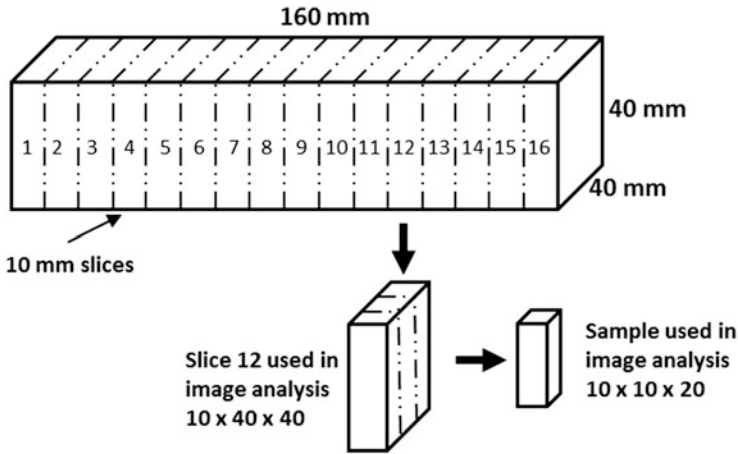


Fig. 1 Prismatic sample and scheme of cross-section slices of 10 mm for micro-tomographic image acquisition

Due to the limitations of the available micro-tomography equipment was necessary the extraction of smaller samples from the original specimen. The specimens were cut transversely into 16 slices with a length of 10 mm, as is shown in Fig. 1.

In previous works [6, 8], the mechanical properties of the mixtures were characterized using mechanical tests. After mechanical tests, the internal structure is composed of mortar, pores, EVA, *piassaba* fibers, and micro-cracks. These elements were characterized using two-dimensional image processing [5, 6].

In this work, the three-dimensional processing of the obtained micro-tomographic images was divided into two stages. The first, the preprocessing stage, includes the binarization of two-dimensional images, its rotation, the three-dimensional reconstruction, and the three-dimensional image cropping. The second is the three-dimensional image segmentation that includes the construction of a region's growth algorithm to make an accurate identification of the interest elements.

The binarization process transformed a grayscale image into a black and white image. As a result, the pixels in the image that represent mortar with cement paste and sand appear in black and those which represent the fibers, EVA grains, pores, and micro-cracks appear in white. These images are rotated to make easier the future crop. These two-dimensional images are stacked to frame the three-dimensional image.

As a result of the mechanical cut of the studied samples to fit in the tomography scanner, some edge problems in the image appeared. To solve these problems, edge techniques are applied in the three-dimensional object. This process was made using three criteria: external cropping, internal cropping, and external cropping with triangular edge. In the external cropping, the most external border point was detected, and this vertical/horizontal plane was selected for the cut. The same

procedure, but with the more internal point in the border, was used in the internal cropping. In the external cropping with triangular edge, first we made an external cropping and, to avoid spurious pixels, the edges were cut using a triangular base prism. Of these criteria, the external cropping with triangular edge shows the best results.

After the obtaining the three-dimensional images, the region's growth algorithm is applied to identify the different elements. This algorithm uses an auxiliary matrix with the same size of original image to store the identified regions. During the process, the three-dimensional image is swept, using the neighborhood concepts. The regions that represent EVA, fibers, pores, and micro-cracks are identified in the auxiliary matrix. In addition, in the algorithm, for each region volumes, the number of voxels is computed. This value represents the volumes of each region.

3 Results and Discussion

The methodology described in the previous section was applied in samples of each mixture type. In samples of pure mortar, only pores are detected. In samples of mortar with EVA, there are pores and EVA grains. In mortar with EVA and *piassaba* fibers, we also find pores and EVA, but the fibers are identified in the mixture too. In mortar with *piassaba* fibers, we detect the pores and the fibers. In those samples submitted to mechanical tests, micro-cracks are also detected. This detection is possible by using volumetric parameters of identifying regions. It is possible to accurately recognize the presence of EVA, fibers, pores, and micro-cracks.

The steps of the methodology for a sample that contains mortar, fibers, and EVA are shown in Fig. 2. This figure is for a sample without mechanical test. Figure 2a represents the original two-dimensional micro-tomographic image. Figure 2b shows the same image after the binarization process. In Fig. 2b, the mortar is in black, and pores and the aggregates are in white. Figure 2c illustrates the result of the rotation process. Figure 2d presents the three-dimensional image, resultant of the stacking process from the two-dimensional slices. Note, in the image, the spurious pixels at the edges. Figure 2e shows the three-dimensional image after the cropping. Finally, Fig. 2f presents the image resulting from the identification process using region's growth algorithm. The identified regions are in different gray tones.

The problems presented in the two-dimensional analysis are solved. The EVA and fibers identified as pores in the two-dimensional analysis are correctly identified by this volumetrical analysis.

Using this methodology and the volumetric analysis, it was possible to identify correctly the EVA, fibers, and pores. Nevertheless, it is not possible to totally separate the micro-cracks from the pores when they have the same volume range. In this case another geometrical region parameter must be used.

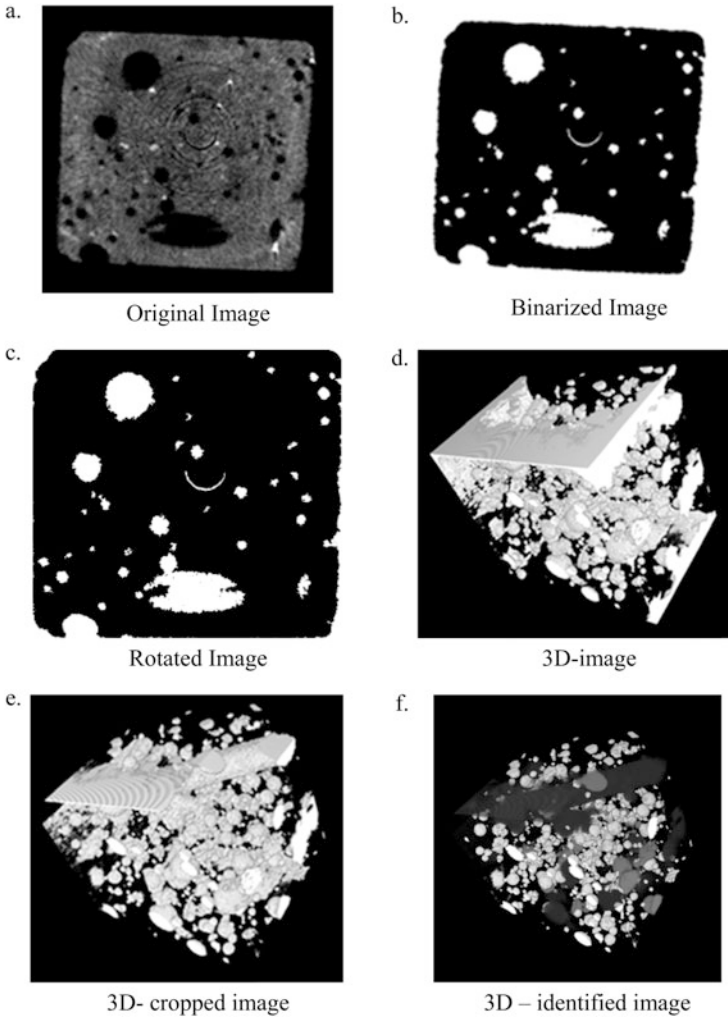


Fig. 2 Steps of the lightweight mortar mixture analysis methodology. In the figure, the sample contains mortar, fibers, and EVA

4 Conclusions

In this work, we obtained a methodology for microstructural analysis of samples of lightweight mortar with aggregates of EVA and *piassaba* fibers. This methodology is based on the three-dimensional image analysis. The images were obtained using micro-tomography and processed in two stages, the preprocessing stage that includes binarization, rotation, and the cropping process and the segmentation stage that uses a region growth algorithm.

As the methodology result, the aggregates, pores, and micro-cracks in the material were identified. Also it is possible to quantify the EVA, pores, and fibers. In samples submitted to mechanical tests, when the micro-cracks have volumes in the same range of the pores, the quantification failed. To solve this problem, other geometrical region parameters as the eccentricity must be considered.

The region's growth algorithm has a high computational cost hindering the processing of high volumes of three-dimensional objects. Computational alternatives, as parallel processing, must be developed in the future to solve this problem. In other research line, we propose the use of Fourier analysis to identify the different aggregates and micro-cracks and solve the edge problems.

Acknowledgments This work was partially supported by Fundação de Amparo à Pesquisa do Estado da Bahia (FAPESB), Brazil. The authors appreciate the computational support offered by Centro de Armazenamento de dados e Computação Avançada da Uesc (CACAU).

References

1. Lopes Lima, P. R., Leite, M. B., & Santiago, E. Q. R. (2010). Recycled lightweight concrete made from footwear industry waste and CDW. *Waste Management*, 30, 1107–1113.
2. Silva, F. A., Mobasher, B., & Filho, R. T. (2011). Mechanical behavior of strain hardening sisal fiber cementitious composites under quasi static and dynamic tensile loading. In *The 2nd international RILEM conference on strain hardening cementitious composites*.
3. Lopes, L. P. R. (2004). *Theoretical and experimental analysis of composites reinforced with sisal fibers*. Ph.D. Thesis, COPPE, Universidade Federal do Rio de Janeiro, Rio de Janeiro (in Portuguese).
4. Savastano, H., Jr., Santos, S. F., Radonjic, M., & Soboyejo, W. O. (2009). Fracture and fatigue of natural fiber-reinforced cementitious composites. *Cement and Concrete Composites*, 31(4), 232–243.
5. Silva, R. M., Dominguez, D. S., Alvim, J. T., & Iglesias, S. M. (2013). Characterization of lightweight cementitious composites reinforced with piassaba fibers using mechanical tests and micro-tomography. *International Review of Chemical Engineering*, 5, 8.
6. Silva, R. M., Dominguez, D. S., Alvim, R. C., & Iglesias, S. M. (2013). Análise da resistência mecânica e porosidade de um compósito cimentício leve com EVA e reforçado com fibras de piaçava. *Revista Eletrônica de Materiais e Processos*, 8, 44–50.
7. Associação Brasileira de Normas Técnicas (ABNT). (2003). *NBR 5738/concrete—Procedure for molding and curing the samples*. Rio de Janeiro: ABNT.
8. Silva, R. M., Alvim, R. C., & Domínguez, D. S. (2011). Study of mechanical strength of a cementitious composite reinforced with piassava fibers. *E.T.C. Educação, Tecnologia e Cultura*, 8, 29–39.

Computational Modeling of Fiber Composites with Thick Fibers as Homogeneous Structures with Use of Couple Stress Theory

Svitlana Fedorova, Tomáš Lasota, and Jiří Burša

Abstract Unidirectional fiber-reinforced elastomers are investigated. A respective finite strain model is formulated within the couple stress theory, and a specific new form of strain energy density is implemented for the three-dimensional finite element analysis. The homogeneous anisotropic model is based on kinematics and constitutive equations proposed by Spencer and Soldatos (International Journal of Non-Linear Mechanics 42:355–368, 2007) and includes additional material parameter regulating bending stiffness of the material regardless of its tensile stiffness. The procedure of determination of the additional material parameter is offered for the case of simple beam under small strains. Numerical simulations of four-point bending test are presented to demonstrate advantage of the new model.

1 Introduction

In the recent years, nonclassical continuum mechanics has become widely employed for dealing with various problems. There are two classes of generalized continuum theories: higher-grade and higher-order theories [1]. In brief, higher-grade theories employ higher-order gradients of the displacements, while higher-order continuum theories include additional kinematic variables attached to the material point. In particular, Cosserat theory [2, 3] (also known as micropolar) introduces independent rotational degrees of freedom to the classical continuum. Its review and bibliography can be found, e.g., in [4]. Couple stress theory [5] can be regarded as a special case of Cosserat theory (constrained Cosserat theory), where connection between the rotation field and the displacement gradients is present.

Conventional theory of fiber-reinforced solids employs an anisotropic homogeneous model with a unit vector field characterizing the direction of reinforcement [6]. Such homogenization is based on the assumption of infinitesimally thin densely

S. Fedorova (✉) • T. Lasota • J. Burša
Institute of Solid Mechanics, Mechatronics and Biomechanics, Brno University of Technology,
Brno, Czech Republic
e-mail: svtlnfdrv2@gmail.com

and uniformly distributed fibers. The closer the composite structure is to this assumption, the better agreement is provided by the model.

Size effects arise when the characteristic length scale of inhomogeneity is comparable with dimensions of the specimen [7]. It is often the case when microscale problems [8–14] or composite materials [7, 15, 16] are considered. The classical Cauchy continuum theory is not able to account for the influence of characteristic size of substructure on material behavior.

In the recent work by Spencer and Soldatos [17], a theoretical framework is introduced which employs the continuum capable of bearing couple stresses. They present a constitutive formulation in which deformed fiber curvature and deformation gradient are present.

In the present work, we regard fibers in the composite as slender beams embedded in the nonlinear elastic matrix. Employing the kinematics and general constitutive formulation presented in [17], we develop a homogeneous model the bending stiffness of which is governed by an additional material parameter independent of the tensile stiffness. The effective bending stiffness is “smeared out” so that the homogeneous model is capable to simulate bending behavior of the real heterogeneous structure.

The layout of the paper presents governing equations and general constitutive formulation of the adopted framework in Sects. 2 and 3. A simple computationally applicable form of strain energy is presented in Sect. 4. In Sect. 5 the principle of the virtual work is formulated for the given framework, and the scheme of the FE implementation is outlined. In Sect. 6 we determine material parameters for the new model. Comparison of numerical results is given in Sect. 7.

2 Adopted Kinematics and Balance Laws

We adopt Cartesian coordinate system $Ox_1x_2x_3$. In a conventional manner, a material point with position vector \mathbf{X} in the reference configuration moves to the position \mathbf{x} of the deformed configuration. In the notation applied below, boldface denotes a tensor or vector; uppercase letter and lowercase letter indices are associated with the reference and deformed configurations, respectively. Subscripts vary from one to three, and Einstein’s summation convention applies for repeated indices unless stated otherwise.

Within the framework of constrained Cosserat theory, the quasi-static problem is considered. The spin vector $\boldsymbol{\omega}$ is not independent but related to the displacement rate vector \mathbf{v} in the following way:

$$\omega_i = \frac{1}{2} \epsilon_{ijk} \frac{\partial v_k}{\partial x_j}, \quad (1)$$

where ϵ_{ijk} represents the Levi-Civita operator. Deformation gradient tensor \mathbf{F} and right Cauchy–Green deformation tensor \mathbf{C} are given by

$$F_{iR} = \frac{\partial x_i}{\partial X_R}, \quad (2)$$

$$C_{KL} = F_{iK}F_{iL}. \quad (3)$$

For a unidirectional fiber-reinforced composite, unit vector fields $\mathbf{A}(\mathbf{X})$ and $\mathbf{a}(\mathbf{X})$ define fiber directions in reference and deformed configurations, respectively. Conventional kinematics has to be enhanced in order to account for the bending stiffness of the continuum. Adopting theoretical framework proposed in [17], additional second-grade kinematical quantities are to be introduced. On the basis of vector $b_i = F_{iR}A_R$, deformed fiber gradient tensor \mathbf{G} and tensor $\mathbf{\Lambda}$ are defined as follows:

$$G_{iJ} = \frac{\partial b_i}{\partial X_J}, \quad (4)$$

$$\Lambda_{RS} = F_{iR}G_{iS}. \quad (5)$$

As we endow the material point with bending stiffness, additional stress measures are to be employed in the form of moments per unit area. These measures are generally referred to as “couple stresses.” Cauchy stress tensor is no longer symmetric due to the presence of couple stresses. This interconnection is obvious from the equations of equilibrium (body forces and body couples are absent):

$$\frac{\partial \sigma_{ji}}{\partial x_j} = 0, \quad (6a)$$

$$\frac{\partial m_{ji}}{\partial x_j} + \epsilon_{ijk}\sigma_{jk} = 0 \quad (6b)$$

where $\boldsymbol{\sigma}$ and \mathbf{m} are Cauchy stress tensor and couple stress tensor, respectively.

3 Constitutive Formulation Within Couple Stress Theory

3.1 Form of Strain Energy Density

Conventional form of the strain energy density for hyperelastic materials with one family of fibers is a function of the right Cauchy–Green deformation tensor \mathbf{C} and fiber direction vector \mathbf{A} .

In order to include the effect of gradients of the deformed fiber direction into the mathematical framework, Spencer and Soldatos [17] proposed the strain energy density, in addition, as a function of tensor $\mathbf{\Lambda}$ [introduced by Eq. (5)]. This function is introduced by means of 33 specific invariants of the above tensors \mathbf{C} , $\mathbf{\Lambda}$, and vector \mathbf{A} on the basis of canonical forms presented by Zheng [18]. However, these 33 independent invariants lead to excessively complicated constitutive equations. To simplify this theory, Spencer and Soldatos propose to assume that the strain energy depends on one-directional derivative of the fiber vector only, namely, that in the fiber direction representing the curvature of fibers. This assumption implies that dependence on the tensor $\mathbf{\Lambda}$ is replaced by dependence on the vector \mathbf{K} with components $K_R = \Lambda_{RS}A_S$. With this restriction the amount of invariants decreases from 33 to 11 having the following forms and physical dimensions:

$$\begin{aligned}
 I_1 &= \text{tr}C, \quad [-] \\
 I_2 &= \frac{1}{2} \left\{ (\text{tr}C)^2 - \text{tr}C^2 \right\}, \quad [-] \\
 I_3 &= \det C, \quad [-] \\
 I_4 &= ACA, \quad [-] \\
 I_5 &= AC^2A, \quad [-] \\
 I_6 &= \mathbf{A}\mathbf{\Lambda}^T\mathbf{\Lambda}\mathbf{A}, \quad [m^{-2}] \\
 I_7 &= \mathbf{A}\mathbf{\Lambda}^T\mathbf{C}\mathbf{\Lambda}\mathbf{A}, \quad [m^{-2}] \\
 I_8 &= \mathbf{A}\mathbf{\Lambda}^T\mathbf{C}^2\mathbf{\Lambda}\mathbf{A}, \quad [m^{-2}] \\
 I_9 &= \mathbf{A}\mathbf{\Lambda}\mathbf{A}, \quad [m^{-1}] \\
 I_{10} &= \mathbf{A}\mathbf{C}\mathbf{\Lambda}\mathbf{A}, \quad [m^{-1}] \\
 I_{11} &= \mathbf{A}\mathbf{C}^2\mathbf{\Lambda}\mathbf{A}. \quad [m^{-1}]
 \end{aligned} \tag{7}$$

However, the strain energy density, as function of all the 11 above invariants, still yields excessively complicated constitutive equations.

3.2 Constitutive Equations for Stresses and Couple Stresses

It should be noted that only the symmetric part of Cauchy stress tensor generates work upon deformation. Analogously, if we decompose couple stress tensor into spherical and deviatoric parts, only its deviatoric components contribute to the energy balance equation. Antisymmetric components of Cauchy stresses can be derived from (6b), while spherical components of couple stresses remain indeterminate within the framework of couple stress theory [19].

Constitutive equations are formulated by Spencer and Soldatos [17] for the symmetric part of Cauchy stress and for the deviatoric part of couple stress as

follows:

$$\sigma_{(ij)} = \frac{\rho}{\rho_0} \left[F_{iR} F_{jS} \left(\frac{\partial W}{\partial C_{RS}} + \frac{\partial W}{\partial C_{SR}} \right) + (G_{iR} F_{jS} + G_{jR} F_{iS}) \frac{\partial W}{\partial \Lambda_{SR}} \right], \quad (8a)$$

$$\bar{m}_{ji} = \frac{2}{3} e_{ikm} \frac{\rho}{\rho_0} \frac{\partial W}{\partial \Lambda_{PR}} F_{mP} (F_{jR} b_k + F_{kR} b_j). \quad (8b)$$

where $\rho_0/\rho = J$ is volume ratio.

The detailed derivation of the equations based on the energy balance equation can be found in [17].

In accordance with equilibrium equations, the antisymmetric part of the stress is defined by the following equation [20]:

$$\sigma_{[ij]} = \frac{1}{2} \epsilon_{kji} \frac{\partial m_{lk}}{\partial x_l}. \quad (9)$$

4 A Simple Specific form of the Model with Modified Invariants

To construct computationally applicable strain energy form suited for the rubberlike composites reinforced with stiff fibers, we employ simplifying assumptions. We restrict W to be quadratic at most in the components of \mathbf{A} . Such assumption, as pointed out in [17], implies that the fiber radius of curvature is large compared to the substructure dimensions (fiber diameters or fiber spacing). To reduce the amount of invariants, the coupling between \mathbf{A} and \mathbf{C} is ignored. For simplicity, we chose strain energy density function that contains only one additional invariant accounting for the bending stiffness of fibers.

To reduce numerical difficulties in finite element simulation, it is advantageous to perform multiplicative decomposition of deformation gradient:

$$\mathbf{F} = \mathbf{J}^{1/3} \bar{\mathbf{F}}, \quad \Rightarrow \quad \mathbf{C} = \mathbf{J}^{2/3} \bar{\mathbf{C}}. \quad (10)$$

where $\bar{\mathbf{F}}$ and $\bar{\mathbf{C}} = \bar{\mathbf{F}}^T \bar{\mathbf{F}}$ are associated with volume-preserving (distortional) deformation of the material. Tensors $\bar{\mathbf{F}}$ and $\bar{\mathbf{C}}$ will be referred to as the modified deformation gradient tensor and modified right Cauchy–Green tensor, respectively [21].

We extend the multiplicative decomposition to second-gradient kinematics by introducing the modified tensor \bar{G} :

$$\bar{G}_{ij} = \frac{\partial \bar{b}_i}{\partial X_j} = \frac{\partial (\bar{F}_{iR} A_R)}{\partial X_j}. \quad (11)$$

After expressing the deformation gradient in terms of displacement vector \mathbf{u} , we obtain

$$\bar{G}_{ij} = G_{ij} J^{-1/3} - \frac{1}{3} A_{iR} J^{-1/3} F_{iR} \frac{\partial^2 u_k}{\partial X_j \partial X_L} \frac{\partial X_L}{\partial x_k}. \quad (12)$$

It should be noted that it holds in case of incompressibility ($J = 1$) [6]:

$$\frac{\partial^2 u_k}{\partial X_j \partial X_L} \frac{\partial X_L}{\partial x_k} = 0, \quad (13)$$

which reduces Eq. (12) into equality $\bar{G}_{ij} = G_{ij}$.

Modified tensor \bar{A} is introduced by the formula

$$\bar{A}_{RS} = \bar{F}_{iR} \bar{G}_{iS}. \quad (14)$$

Similarly it can be shown for tensor \bar{A} that in case of incompressibility, the modified tensor equals the original one, i.e., $\bar{A}_{RS} = A_{RS}$.

Based on the modified tensors above, modified invariants can be introduced [22]:

$$\bar{I}_1 = \bar{C}_{AA} = J^{-2/3} C_{AA}, \quad (15)$$

$$\bar{I}_4 = A_B \bar{C}_{CB} A_C = J^{-2/3} A_B C_{CB} A_C, \quad (16)$$

$$\begin{aligned} \bar{I}_6 = & A_B \bar{\Lambda}_{OB} \bar{\Lambda}_{OC} A_C = J^{-4/3} (A_B \Lambda_{OB} \Lambda_{OC} A_C - \\ & - \frac{1}{3} F_{OK}^{-1} G_{KO} A_L C_{LR} (A_S \Lambda_{RS} + A_N \Lambda_{RN} - \frac{1}{3} G_{BC} F_{CB}^{-1} A_O C_{OR})). \end{aligned} \quad (17)$$

The strain energy density consists then of isochoric (deviatoric) and volumetric parts; the deviatoric part is composed of isotropic and anisotropic contributions:

$$W = \bar{W} + W_{\text{vol}}, \quad (18)$$

$$W_{\text{vol}} = \frac{1}{d} (J - 1)^2, \quad (19)$$

$$\bar{W} = \bar{W}_{\text{iso}} + \bar{W}_{\text{aniso}}, \quad (20)$$

$$\bar{W}_{\text{iso}} = k_1 (\bar{I}_1 - 3), \quad (21)$$

$$\bar{W}_{\text{aniso}} = k_2 (\bar{I}_4 - 1)^2 + k_3 \bar{I}_6. \quad (22)$$

Then the strain energy density has the final form

$$W = k_1 (\bar{I}_1 - 3) + k_2 (\bar{I}_4 - 1)^2 + k_3 \bar{I}_6 + \frac{1}{d} (J - 1)^2. \quad (23)$$

To allow for a stress-free reference configuration, the anisotropic term ($I_4 - 1$) can occur in W only through its squares [23]. The strain energy density must be at least quadratic in the components of either \mathbf{F} or \mathbf{G} [24]. The coefficients present material parameters: k_1 is related to properties of the matrix (neo-Hooke model); k_2 and k_3 relate to the tensile and bending stiffness of the medium in the direction of reinforcement, respectively; and d relates to the material compressibility.

According to (8a, 8b) and (23), constitutive equations acquire the form

$$\begin{aligned} \sigma_{(ij)} = & 2F_{iR}F_{jS}J^{-2/3} \left[k_1 \left(\delta_{SR} - \frac{1}{3}C_{RS}^{-1}C_{AA} \right) + 2k_2 (\bar{I}_4 - 1) (A_R A_S - \right. \\ & \left. \frac{1}{3}C_{RS}^{-1}A_B C_{CB} A_C) + \frac{1}{d} (J - 1) C_{RS}^{-1} J^{-3/2} \right] + k_3 \left[F_{iR}F_{jS} \left(\frac{\partial \bar{I}_6}{\partial C_{RS}} + \frac{\partial \bar{I}_6}{\partial C_{SR}} \right) \right. \\ & \left. + (G_{iS}F_{jR} + G_{jS}F_{iR}) \frac{\partial \bar{I}_6}{\partial \Lambda_{RS}} \right]. \end{aligned} \quad (24a)$$

$$\bar{m}_{ji} = \frac{2}{3} e_{ikm} k_3 \frac{\partial \bar{I}_6}{\partial \Lambda_{PR}} F_{mP} (F_{jR} b_k + F_{kR} b_j). \quad (24b)$$

5 Finite Element Implementation

In this section, displacement-based finite element approach is presented. It should be noted that an alternative approach employing Lagrange C^0 -shape functions is possible, in which first derivatives of displacements are introduced as additional independent unknowns. In that case, the relation (1) must be taken into account via Lagrange multipliers [25].

5.1 Weak Form of the Stationary Boundary Value Problem

In order to develop finite element formulation we start with constructing the weak form of the balance Eq. (6a, 6b). Let us introduce virtual displacement rate field

δv and virtual spin field $\delta \omega$ as the weighting functions. Multiplication of (6a) with δv and (6b) with $\delta \omega$ and subsequent integration of their sum over the current configuration (volume v) yield

$$\int_v \frac{\partial \sigma_{ji}}{\partial x_j} \delta v_i dv + \int_v \left(\frac{\partial m_{ji}}{\partial x_j} \delta \omega_i + \epsilon_{ijk} \sigma_{jk} \delta \omega_i \right) dv = 0. \quad (25)$$

With the use of divergence theorem, it can be rewritten as

$$\int_v \left(\sigma_{ij} \frac{\partial \delta v_i}{\partial x_j} + m_{ji} \frac{\partial \delta \omega_i}{\partial x_j} - \epsilon_{ijk} \sigma_{jk} \delta \omega_i \right) dv - \int_s (t_i \delta v_i + l_i \delta \omega_i) ds = 0 \quad (26)$$

where \mathbf{t} is traction vector and \mathbf{l} couple traction vector (moment per unit area) acting on surface s of the deformed body.

Partial derivatives $\frac{\partial v_i}{\partial x_j}$ can be divided into symmetric d_{ij} and antisymmetric ω_{ij} parts

$$\frac{\partial v_i}{\partial x_j} = d_{ij} + \omega_{ij} \quad (27)$$

where d_{ij} are components of the rate of deformation tensor and ω_{ij} are components of the spin tensor.

Similarly the force stress can be divided into its symmetric $\sigma_{(ij)}$ and antisymmetric $\sigma_{[ij]}$ parts and the couple stress into its volumetric and deviatoric parts.

Note that the following relations [17] are valid:

$$\sigma_{[ij]} d_{ij} = 0; \quad (28)$$

$$\sigma_{(ij)} \omega_{ij} = 0; \quad (29)$$

$$\frac{\partial \omega_i}{\partial x_i} = 0, \quad (30)$$

and spin tensor and spin vector are related as

$$\epsilon_{ijk} \omega_i = -\omega_{jk}. \quad (31)$$

With the use of the above equations, the principle of virtual work is then formulated as follows:

$$\int_v \left(\sigma_{(ij)} \frac{\partial \delta v_i}{\partial x_j} + \bar{m}_{ji} \frac{\partial \delta \omega_i}{\partial x_j} \right) dv - \int_s (t_i \delta v_i + l_i \delta \omega_i) ds = 0. \quad (32)$$

With the kinematic constraint (1), it becomes

$$\int_v \left(\sigma_{(ij)} \frac{\partial \delta v_i}{\partial x_j} + \frac{1}{2} \epsilon_{ilk} \bar{m}_{ji} \frac{\partial^2 \delta v_k}{\partial x_j \partial x_l} \right) dv - \int_s \left(t_i \delta v_i + \frac{1}{2} \epsilon_{ijk} l_i \frac{\partial \delta v_k}{\partial x_j} \right) ds = 0. \quad (33)$$

In accordance with the constrained Cosserat theory, displacement vector field is taken to be the only fundamental unknown.

Let us now introduce (Kirchhoff) symmetric force stress $\tau_{(ij)}$ and deviatoric couple stress: $\bar{\mu}_{ij}$

$$\tau_{(ij)} = J \sigma_{(ij)}; \quad (34a)$$

$$\bar{\mu}_{ij} = J \bar{m}_{ij}. \quad (34b)$$

Then we can rewrite (31) as

$$\int_v \left(\tau_{(ij)} \frac{\partial \delta v_i}{\partial x_j} + \frac{1}{2} \epsilon_{ilk} \bar{\mu}_{ji} \frac{\partial^2 \delta v_k}{\partial x_j \partial x_l} \right) dV - \int_s \left(t_i \delta v_i + \frac{1}{2} \epsilon_{ijk} l_i \frac{\partial \delta v_k}{\partial x_j} \right) ds = 0. \quad (35)$$

The volume integral has now taken over the undeformed solid, which is convenient for further computations. The area integral is evaluated over the deformed surface. However, as long as traction and traction couples are not prescribed on the boundary, the second term in (34a) is ignored. Here and further we consider the case when only displacements and their first derivatives are prescribed as boundary conditions. Consequently, the principle of virtual work (34a) can be rewritten into the final form

$$\int_v \left(\tau_{(ij)} \frac{\partial \delta v_i}{\partial x_j} + \frac{1}{2} \epsilon_{ilk} \bar{\mu}_{ji} \frac{\partial^2 \delta v_k}{\partial x_j \partial x_l} \right) dV = 0. \quad (36)$$

5.2 Approximation and Discretization

Due to presence of the gradients of strain in the variational formulation, a need arises for higher orders of continuity in the interpolation functions. Namely, so-called complete C_1 element shape functions are to be employed. Displacement field and virtual displacement rate field within the element are approximated in the following manner:

$$u_i(\xi) = N^a(\xi) u_i^a + O^a(\xi) \alpha_i^a + P^a(\xi) \beta_i^a + Q^a(\xi) \gamma_i^a, \quad (37)$$

$$\delta v_i(\xi) = N^a(\xi) \delta v_i^a + O^a(\xi) \delta \alpha_i^a + P^a(\xi) \delta b_i^a + Q^a(\xi) \delta g_i^a \quad (38)$$

where ξ_i are normalized local coordinates, $-1 < \xi_i < 1$ (natural coordinates), u_i^a can be regarded as nodal displacements, and $\alpha_i^a, \beta_i^a, \gamma_i^a$ as nodal slopes in directions ξ_1, ξ_2 , and ξ_3 respectively; superscript indices identify the node number. Virtual rates of nodal displacements and slopes are denoted as $\delta v_i^a, \delta \alpha_i^a, \delta \beta_i^a, \delta \gamma_i^a$ in (36). N, O, P , and Q are Hermite polynomials [26] satisfying the following conditions: $N^a(\xi)$ takes the value of 1 at node a and zero at all the other nodes within the element; its derivatives $\frac{\partial N^a(\xi)}{\partial \xi_i}$ are zero at all nodes; $O^a(\xi), P^a(\xi)$, and $Q^a(\xi)$ take zero value at all nodes, while their derivatives $\frac{\partial O^a(\xi)}{\partial \xi_1}, \frac{\partial P^a(\xi)}{\partial \xi_2}$, and $\frac{\partial Q^a(\xi)}{\partial \xi_3}$ take value of 1 at node a and zero at all the others; the derivatives with respect to the other ξ_i are zero at all nodes.

In order to proceed with discretization, let us convert derivatives in the weak form (34b) to the reference coordinates X_i , thus obtaining

$$\int_V \left(\tau_{(ij)} \frac{\partial \delta v_i}{\partial X_M} F_{Mj}^{-1} + \frac{1}{2} \epsilon_{ikl} \bar{w}_{ji} F_{Mj}^{-1} \left(F_{Nk}^{-1} \frac{\partial^2 \delta v_i}{\partial X_M \partial X_N} - F_{No}^{-1} F_{Pk}^{-1} \frac{\partial \delta v_i}{\partial X_N} \frac{\partial F_{oP}}{\partial X_M} \right) \right) dV = 0. \quad (39)$$

Using Eq. (39) and element connectivity and utilizing the fact that $\delta v_i^a, \delta \alpha_i^a, \delta \beta_i^a, \delta \gamma_i^a$ are arbitrary everywhere, except for the boundary surface, we obtain four systems of nonlinear equations. Integration is performed using a standard Gauss quadrature scheme.

These nonlinear systems are to be solved using Newton–Raphson iterative procedure. After the linearization, the following four linear systems with respect to unknown increments of displacements Δu_i^a and increments of slopes $\Delta \alpha_i^a, \Delta \beta_i^a, \Delta \gamma_i^a$ are considered:

$$\begin{aligned} K_{aibk}^{uu} \Delta u_k^b + K_{aibk}^{u\alpha} \Delta \alpha_k^b + K_{aibk}^{u\beta} \Delta \beta_k^b + K_{aibk}^{u\gamma} \Delta \gamma_k^b &= R_i^a \\ K_{aibk}^{\alpha u} \Delta u_k^b + K_{aibk}^{\alpha\alpha} \Delta \alpha_k^b + K_{aibk}^{\alpha\beta} \Delta \beta_k^b + K_{aibk}^{\alpha\gamma} \Delta \gamma_k^b &= S_i^a \\ K_{aibk}^{\beta u} \Delta u_k^b + K_{aibk}^{\beta\alpha} \Delta \alpha_k^b + K_{aibk}^{\beta\beta} \Delta \beta_k^b + K_{aibk}^{\beta\gamma} \Delta \gamma_k^b &= T_i^a \\ K_{aibk}^{\gamma u} \Delta u_k^b + K_{aibk}^{\gamma\alpha} \Delta \alpha_k^b + K_{aibk}^{\gamma\beta} \Delta \beta_k^b + K_{aibk}^{\gamma\gamma} \Delta \gamma_k^b &= U_i^a. \end{aligned} \quad (40)$$

5.3 Implementation

A new finite element solver was written in Matlab software. Hexahedral finite elements with 8 nodes and 27 integration points were used for iterative solution of Eq. (40). Iterative process is terminated when residual (disequilibrium) is less than a tolerance times a reference value $\|\bar{R}\| < 0.00001 \bar{R}_{\text{ref}}$ and when the increment of displacements and slopes is less than the tolerance times a reference value $\|\Delta \bar{u}\| < 0.0001 \bar{u}_{\text{ref}}$.

Here \bar{R} is vector of residuals

$$\bar{R} = \begin{pmatrix} R \\ S \\ T \\ V \end{pmatrix}, \quad (41)$$

$\Delta\bar{u}$ is vector of increments of displacements and slopes

$$\Delta\bar{u} = \begin{pmatrix} \Delta u \\ \Delta\alpha \\ \Delta\beta \\ \Delta\gamma \end{pmatrix}, \quad (42)$$

and $\|\cdot\|$ is a vector norm ($\|\bar{R}\| = \sqrt{\sum R_i^2}$). \bar{R}_{ref} and \bar{u}_{ref} are reference values, \bar{R}_{ref} is vector of restoring loads corresponding to element internal loads at nodes with imposed displacement constraints and $\bar{u}_{\text{ref}} = \|\bar{u}\|$ where

$$\bar{u} = \begin{pmatrix} u \\ \alpha \\ \beta \\ \gamma \end{pmatrix}. \quad (43)$$

6 Identification of Material Parameters for Small Strains

6.1 Couple Stress Theory for the Planar Problem

For the illustration, let us consider an elementary volume in equilibrium for a planar problem (Fig. 1). In accordance with balance Eq. (6a, 6b), the following is true for the given coordinates:

$$-\sigma_{13} + \sigma_{31} + \frac{\partial m_{12}}{\partial X_1} + \frac{\partial m_{22}}{\partial X_2} + \frac{\partial m_{32}}{\partial X_3} = 0. \quad (44)$$

Let us consider a beam undergoing pure bending around X_2 axis. Figure 2 presents schematically inner resultants acting on the section of the beam. Normal stress distribution contributing to a positive value of the classic moment M_2 for the given coordinates and positive direction of the couple stresses for the given coordinates are depicted below.

For the case of small linear strains, we operate with displacements u_i and rotations $\theta_i = \frac{1}{2}\epsilon_{ijk}\frac{\partial u_k}{\partial x_j}$ instead of displacement rates and spins.

Fig. 1 Positive directions of the shear stresses and couple stresses in a planar problem

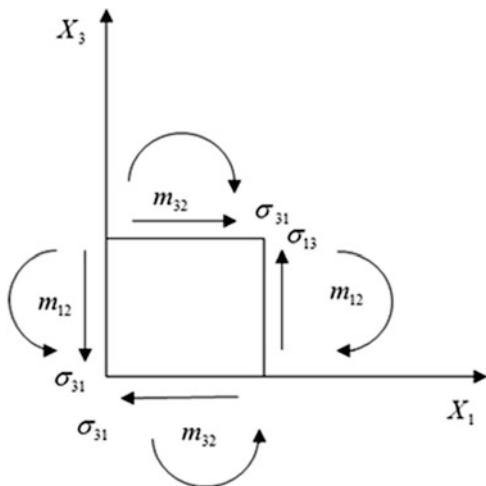
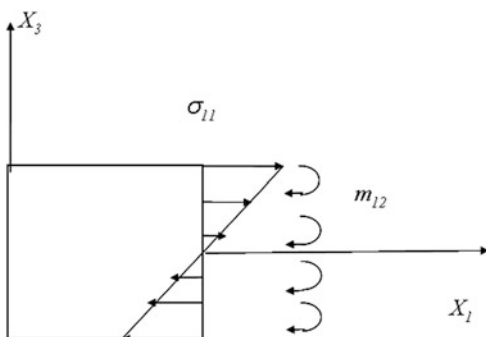


Fig. 2 Stress and couple stress distribution in pure bending



The overall bending moment in the beam cross section can be calculated as

$$M_2^{\text{full}} = \iint_S (\sigma_1 x_3 + m_{12}) dx_2 dx_3, \tag{45}$$

$$M_2^{\text{full}} = M_2 + \iint_S m_{12} dx_2 dx_3. \tag{46}$$

6.2 *Discrepancy Between Heterogeneous and Homogeneous Models Within the Conventional Elasticity*

Let us consider linear elastic behavior of a composite beam with one family of fibers aligned along the beam axis. Such a specimen can be modeled as a heterogeneous structure characterized by elastic constants of constituents and a specific

arrangement and size of fibers. Also, it can be modeled using a homogenized anisotropic (transversely isotropic) hyperelastic model. In this case the tensile stiffness of the specimen in the preferred direction is uniformly “smeared out” throughout the section of the model. The corresponding elastic modulus in the direction of fibers can be obtained by the rule of mixtures:

$$E_{\text{hom}} = (1 - \psi_f) E_m + \psi_f E_f, \quad (47)$$

where ψ_f is the volume fraction of fibers. As it can be seen from (45), the homogeneous model is characterized by elastic constants of constituents and their volume fractions only, with no regard to disposition and distribution of fibers in the given composite.

Let us compare the pure bending behavior of these two beam models. If the heterogeneous model is subjected to bending along the fibers, we can express the overall bending moment in the section as $M_2 = D_{\text{het}} k$, where $k = -\frac{\partial^2 u_3}{\partial x_1^2}$ is the curvature of the beam and D_{het} is the bending stiffness of the model along the preferred direction:

$$D_{\text{het}} = E_m J_m + E_f J_f, \quad (48)$$

where J_m and J_f are overall moments of inertia of the sections of matrix and fibers, respectively.

If the homogeneous model is subjected to bending along the direction of the reinforcement, we can express the overall bending moment in the section as $M_2 = D_{\text{hom}} k$, where k is the curvature and D_{hom} is the bending stiffness of the homogeneous model:

$$D_{\text{hom}} = E_{\text{hom}} J, \quad (49)$$

where J is the moment of inertia of the whole cross section of the beam.

If we substitute E_{hom} from (47), we obtain

$$D_{\text{hom}} = ((1 - \psi_f) E_m + \psi_f E_f) J. \quad (50)$$

If we compare (50) and (48), it is obvious that the homogenized model cannot successfully simulate bending behavior of the heterogeneous model. The bending stiffness D_{hom} takes into account volume fraction of fibers and properties of the constituents only but does not include moments of inertia of constituents. By replacing the heterogeneous model with a transversely isotropic one, we preserve the same tensile stiffness but not the same bending response, as illustrated below (Fig. 3).

Bending stiffness D_{hom} can be larger or smaller than the actual stiffness D_{het} of the corresponding heterogeneous model, depending on the distribution of the fibers with respect to the neutral plane (middle plane in case of symmetrical cross section).

Fig. 3 Sections of the models with the same value of D_{hom} but different D_{het}



The homogeneous model which describes bending behavior in accordance with the heterogeneous one more accurately can be formulated using couple stress theory.

6.3 Parameter k_3 for the Equivalent Model of the Fiber-Reinforced Beam

We continue to consider a beam reinforced by parallel fibers subjected to pure bending with respect to X_2 axis (Fig. 4). For simplicity, material incompressibility is assumed. The goal is to construct an equivalent homogeneous anisotropic model within the constrained Cosserat continuum. Such equivalent model must correctly simulate the response of the original structure under both bending and tension. We begin with simplifying the governing equations for the couple stress continuum under small-strain assumptions.

In the case when fibers are initially aligned along the X_1 direction, it holds in general:

$$A = \begin{pmatrix} 1 \\ 0 \\ 0 \end{pmatrix}, \quad (51)$$

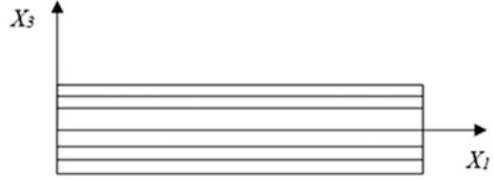
$$F = \begin{pmatrix} 1 + \frac{\partial u_1}{\partial X_1} & \frac{\partial u_1}{\partial X_2} & \frac{\partial u_1}{\partial X_3} \\ \frac{\partial u_2}{\partial X_1} & 1 + \frac{\partial u_2}{\partial X_2} & \frac{\partial u_2}{\partial X_3} \\ \frac{\partial u_3}{\partial X_1} & \frac{\partial u_3}{\partial X_2} & 1 + \frac{\partial u_3}{\partial X_3} \end{pmatrix}, \quad (52)$$

$$b = \begin{pmatrix} 1 + \frac{\partial u_1}{\partial X_1} \\ \frac{\partial u_2}{\partial X_1} \\ \frac{\partial u_3}{\partial X_1} \end{pmatrix}. \quad (53)$$

Overall bending moment M^{full} acting in the cross section of the model is given by (45). The constitutive relations for an incompressible material given in the general form are

$$\sigma_{(ij)} = \left[F_{iR} F_{jS} \left(\frac{\partial W}{\partial C_{RS}} + \frac{\partial W}{\partial C_{SR}} \right) + (G_{iR} F_{jS} + G_{jR} F_{iS}) \frac{\partial W}{\partial \Lambda_{SR}} \right] + p \delta_{ij}, \quad (54a)$$

Fig. 4 The beam in the reference configuration



$$\bar{m}_{ji} = \frac{2}{3} e_{ikm} \frac{\partial W}{\partial \Lambda_{PR}} F_{mP} (F_{jR} b_k + F_{kR} b_j) \quad (54b)$$

where p is hydrostatic pressure. In this case,

$$W = \frac{\mu}{2} (I_1 - 3) + k_2 (I_4 - 1)^2 + k_3 I_6, \quad (55)$$

where unmodified invariants I_1, I_4, I_6 can be used.

Let us linearize constitutive relations (54a, 54b) for the case of small strains. The basic assumption is that all partial derivatives of displacements are much smaller than one. If we follow the notation of [17], we can state that all $\frac{\partial u_i}{\partial x_j}$ are of the order of magnitude $O(e)$. Consequently the strain energy density W has to be of the order $O(e^2)$, and terms of higher order can be discarded.

Symmetric stresses have to be of order $O(e)$. If we leave out higher-order terms in (54a), the following expression is left:

$$\sigma_{(ij)} = \frac{\partial W}{\partial C_{ij}} + \frac{\partial W}{\partial C_{ji}} + \delta_{ij} p. \quad (56)$$

It should be noted that if no volumetric deformation occurs and we use strain energy density function such as (55), in which no coupling between \mathbf{C} and \mathbf{A} is present, the symmetric stresses (56) do not depend on the fiber curvature. Therefore the expressions for normal stresses are identical with those in the classical (Cauchy) theory of transversely isotropic materials. If we compute $\sigma_{(11)}$ for the case of bending of the beam along the fiber direction using (55) and (56) and then neglect all the quantities of the order of magnitude higher than $O(e)$, we obtain

$$\sigma_{(11)} = (3\mu + 8k_2) \varepsilon_{11} + p, \quad (57)$$

where ε_{11} is tensile strain and $(3\mu + 8k_2)$ is equivalent of Young's modulus of the material in the preferred direction. We can rewrite it as

$$\sigma_{(11)} = E_{\text{hom}} \varepsilon_{11} + p. \quad (58)$$

If shear is absent and plane $X_1 X_2$ coincides with the neutral plane of the beam, the longitudinal strain ε_{11} is expressed via curvature k as $\varepsilon_{11} = k \cdot X_3$, where $k = -\frac{\partial^2 u_3}{\partial x_1^2}$.

Then we can rewrite (54b) as

$$\sigma_{(II)} = E_{\text{hom}} k X_3 + p. \quad (59)$$

Now let us consider deviatoric couple stresses. For the given problem, we have

$$I_6 = \Lambda_{11}^2 + \Lambda_{21}^2 + \Lambda_{31}^2 \quad (60)$$

$$\frac{\partial I_6}{\partial \Lambda_{i1}} = 2\Lambda_{i1}. \quad (61)$$

Relation (5) gives

$$\Lambda_{31} = F_{13} \frac{\partial^2 u_1}{\partial X_1^2} + F_{23} \frac{\partial^2 u_2}{\partial X_1^2} + F_{33} \frac{\partial^2 u_3}{\partial X_1^2}. \quad (62)$$

If we assume small strains and consider only bending with respect to axis X_2 , it holds

$$\Lambda_{31} = F_{33} \frac{\partial^2 u_3}{\partial X_1^2} \approx \frac{\partial^2 u_3}{\partial X_1^2}. \quad (63)$$

Employing relation (8b) and (63) and leaving out the higher-order terms, we obtain

$$\bar{m}^{\text{lin}}_{12} = -\frac{8}{3} k_3 \Lambda_{31} = -\frac{8}{3} k_3 \frac{\partial^2 u_3}{\partial X_1^2} \quad (64)$$

Using the notion of curvature introduced above, we can reformulate (64) as

$$\bar{m}^{\text{lin}}_{12} = \frac{8}{3} k_3 k. \quad (65)$$

Employing (45), (59), and (65), we obtain

$$M_2^{\text{full}} = \iint_S \left(E_{\text{hom}} k \cdot X_3^2 + \frac{8}{3} k_3 k \right) dX_2 dX_3. \quad (66)$$

As the beam curvature and the material parameters are constant throughout the section, the following is valid:

$$M_2^{\text{full}} = E_{\text{hom}} k \cdot \iint_S X_3^2 dX_2 dX_3 + \frac{8}{3} k_3 k \cdot \iint_S dX_2 dX_3. \quad (67)$$

The bending moment then equals

$$M_2^{\text{full}} = D_{\text{hom}}^{\text{full}} \cdot k, \quad (68)$$

where the $D_{\text{hom}}^{\text{full}}$ can be identified as the bending stiffness of the model:

$$D_{\text{hom}}^{\text{full}} = E_{\text{hom}}J + \frac{8}{3} \cdot k_3 \cdot S, \quad (69)$$

where S is the beam cross section area.

The constant k_3 is then determined from the condition $D_{\text{hom}}^{\text{full}} = D_{\text{het}}$ as

$$k_3 = \frac{3}{8} \frac{E_m J_m + E_f J_f - E_{\text{hom}} J}{S} = \frac{3}{8} \frac{D_{\text{het}} - D_{\text{hom}}}{S}. \quad (70)$$

This formula is analogous to the rule of mixture in application to the bending stiffness. The effective bending stiffness of the initial heterogeneous model is “smeared out” uniformly throughout the section of the homogeneous model by means of the couple stress theory.

The condition $D_{\text{hom}}^{\text{full}} = D_{\text{het}}$ is equivalent to the condition of equality of the bending moments acting on the cross sections of the composite beam and correspondent homogeneous beam. The similar logics is used in [27] where the authors employ the condition of equal strain energies stored in the heterogeneous and correspondent homogeneous representative volumes (for the case of homogenization of cellular materials). From formula (67), it can be seen that the additional material parameter k_3 serves to augment the bending stiffness of the couple stress continuum beam without interfering with its tensile stiffness. In this sense, the term with k_3 can be understood as the difference between the bending stiffness supplied by the averaged Young’s modulus and the actual bending stiffness of the heterogeneous structure. If the fibers are thin and densely and uniformly distributed, the constant k_3 tends to zero.

7 Numerical Example of Bended Beam

On the basis of the formulation given in Sect. 5, the finite element code has been written in Matlab software. As an illustrative example, let us consider a fiber-reinforced composite beam with two rows of unidirectional fibers (cross section is schematically presented in Fig. 3 to the left) undergoing four-point bending (Fig. 5). As the fiber diameter is comparable to the dimensions of the specimen, size effect is to be expected. The given specimen is modeled in three different ways:

- Via heterogeneous FE model with explicitly modeled fibers embedded in matrix
- Via equivalent homogeneous transversally isotropic FE model in accordance with the classic elasticity (later referred to as classic model)

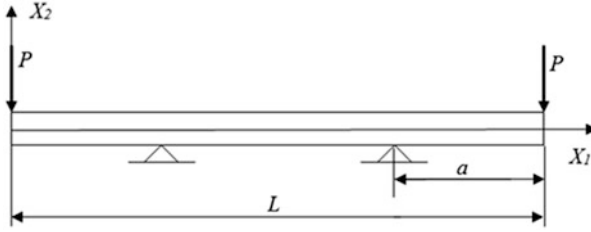


Fig. 5 Four-point bending

- Via equivalent homogeneous transversally isotropic FE model in accordance with the couple stress theory and formulations given in Sects. 4 and 5 (later referred to as CST model)

7.1 A Thin Composite Beam with the 0° Fiber Declination: Four-Point Bending

Let us consider a fiber-reinforced composite with two rows of unidirectional fibers with the dimensions $40 \times 2 \times 1$ mm. Fiber diameter is $d = 0.1$ mm, distance from the middle plane to fiber center is $c = 0.35$ mm, and the fiber spacing in each row is $s = 0.1$ mm. Material constants of the constituents include elastic modulus $E_f = 2100$ MPa and Poisson ratio $\nu_f = 0.3$ of fibers and matrix parameters for neo-Hooke material law $\mu = 2$ MPa, $d = 0.0001$ MPa $^{-1}$. The strain energy potential for the rubber matrix is given as follows:

$$W = \frac{\mu}{2} (I_1 - 3) + \frac{1}{d} (J - 1)^2. \quad (71)$$

The conventional model with fiber direction defined by vector \mathbf{A} is based on the strain energy density

$$W = \frac{\mu}{2} (I_1 - 3) + k_2 (I_4 - 1) + \frac{1}{d} (J - 1)^2. \quad (72)$$

Then it holds for stress

$$\sigma_{ij} = 2F_{ik}F_{jl} \frac{\partial W}{\partial C_{ikl}}. \quad (73)$$

The shear modulus μ is the same as used for matrix in the heterogeneous model. For the given problem with linear elastic fibers under small strains, the constant k_2 can be calculated from the condition of the same average tensile stiffness of the

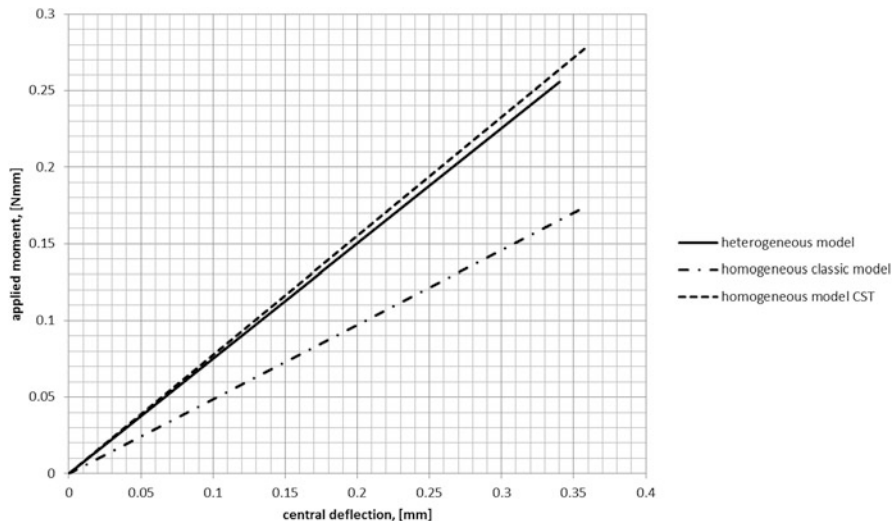


Fig. 6 Comparison of FE simulations of four-point bending using different constitutive models (0° fiber declination)

heterogeneous and homogeneous models in the preferred direction (see Appendix) as $k_2 = \frac{1}{8} ((1 - \psi_f) \cdot E_m + \psi_f \cdot E_f - 3\mu) = 18.244$ MPa.

In the CST model, a new term I_6 is added related to the curvature of the deformed fibers. The corresponding hyperelastic anisotropic potential is as follows according to (23):

$$W = \frac{\mu}{2} (\bar{I}_1 - 3) + k_2 (\bar{I}_4 - 1)^2 + k_3 \bar{I}_6 + \frac{1}{d} (J - 1)^2.$$

The objective is to set all the constants so that this model correctly simulates both tensile and bending behavior of the given heterogeneous model.

According to (70) and the given data, we set the constant $k_3 = 2.1718$ Pa \times m². Constants μ and k_2 are the same as in the classical model used above. Results of all the three simulations are compared in Fig. 6.

7.2 A Thin Composite Beam with 30° Fiber Declination: Four-Point Bending

The example above is a standard linear problem which can be solved analytically with respect to the deflection which can be assumed constant throughout the beam thickness. This simplicity occurs due to the fibers being aligned along the X_1 axis. In the present example, we consider the case when the fibers have 30° declination

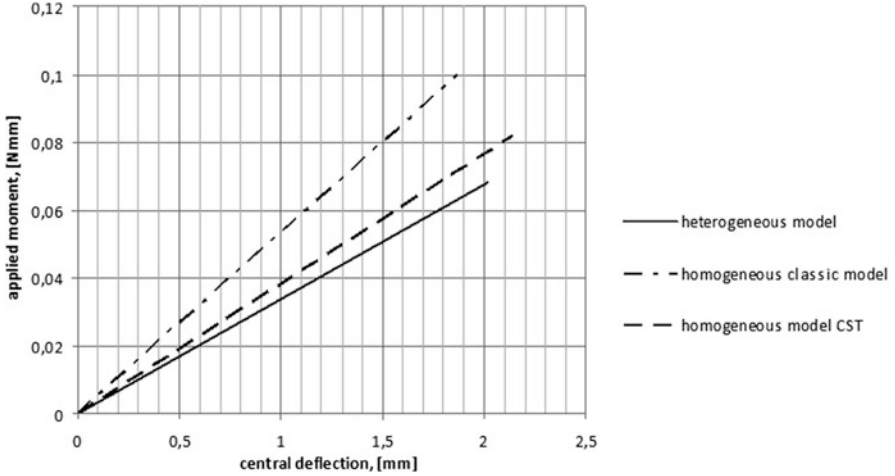


Fig. 7 Comparison of FE simulations of four-point bending using different constitutive models (30° fiber declination)

angle which renders the problem unsolvable analytically. Dimensions of the composite structure are given as follows: $240 \times 25.4 \times 5$ and 8 mm. Fiber diameter is $d = 0.45$ mm, distance from the middle plane to fiber center is $c = 1.45$ mm, and the fiber spacing in each row is $s = 0.65$ mm.

Material constants of the constituents include elastic modulus $E_f = 2100$ MPa and Poisson ratio $\nu_f = 0.3$ of fibers and matrix parameters for Neo-Hooke material law $\mu = 2$ MPa, $d = 0.0001$ MPa⁻¹. The plate is loaded as shown in Fig. 5.

The material constants for the “classic” and “CST” models are analytically derived in the similar way as outlined in 7.1 and Appendix. The constant k_3 is determined using (70).

The values of the material parameters obtained for the expression (72) are as follows: $k_2 = 12.75$ MPa and $k_3 = -25.27$ Pa \times m². Negative value of the constant k_3 indicates that the bending stiffness of the classical homogeneous model, generated by the averaged tensile stiffness of the heterogeneous beam, is higher than the real bending stiffness of the beam. So the CST model is constructed by augmenting the classic model with the additional term that, roughly speaking, subtracts the excessive bending stiffness without in any way affecting tensile properties of the model (which are in complete agreement with the heterogeneous structure already). Importantly, the fiber direction unit vector is now defined as $(0.866, 0, 0.5)^T$. The results of the simulations are presented (Fig. 7).

8 Conclusion

The constitutive equations published in Spencer and Soldatos [17] are used to formulate a specific form of strain energy density function on the basis of constraint Cosserat theory (in which couple stresses are introduced and displacements or displacement rates are the only independent unknowns). This approach leads to second derivatives of displacement rates occurring in the finite element formulations. A specific form of strain energy density was proposed with an additional term correcting the effective bending stiffness of the continuum. The higher-order continuity required on element boundaries is solved by means of C_1 elements, and parameters of the model are determined on the basis of fictitious experiments. With the example of the beam under bending, it is shown that the discrepancy between the classical homogeneous model and a heterogeneous model including dimensions and topology of the fibers can be largely overcome by the presented approach. The mentioned example is considered for the case of the small strains. The further verifications of the model and the finite element code are matters of ongoing research.

Acknowledgments This work was supported by the Czech Science Foundation project number 13-16304S, by faculty project number FSI-S-14-2344, and through NETME CENTRE PLUS (LO1202) by financial means from the Ministry of Education, Youth and Sports under the “National Sustainability Programme I.”

Appendix

The material parameter k_2 can be determined under condition that the tensile force in the direction of fiber remains the same in both the homogenous and heterogeneous models under uniaxial tension $p^{\text{het}} = p^{\text{hom}}$.

Consider $\mathbf{A} = \begin{pmatrix} \mathbf{1} \\ \mathbf{0} \\ \mathbf{0} \end{pmatrix}$ and uniaxial tension in the direction X_1 . We consider

small tensile strains in the fiber direction; therefore linearized constitutive equations might be used. $\sigma_{ij} = 2F_{ik}F_{jl}\frac{\partial W}{\partial C_{ijkl}}$ is general constitutive relation for incompressible hyperelastic material (hydrostatic pressure is absent). The strain energy density is given by $W = \frac{\mu}{2}(I_1 - 3) + k_2(I_4 - 1)^2$. The right Cauchy–Green deformation tensor

is $C = \begin{pmatrix} \lambda_1^2 & 0 & 0 \\ 0 & \lambda_2^2 & 0 \\ 0 & 0 & \lambda_3^2 \end{pmatrix}$, and incompressibility condition holds $\lambda_1\lambda_2\lambda_3 = 1$, where

$\lambda_1, \lambda_2, \lambda_3$ are principal stretch ratios.

Consequently, we can write that

$$\sigma_{11}^{\text{hom}} = \mu \left(2\lambda^2 + \frac{1}{\lambda} \right) + 4k_2 (\lambda^4 - \lambda^2) \quad (74)$$

where $\lambda = \lambda_1$ is the stretch ratio in the direction of fiber.

For the small strains, it takes form

$$\sigma_{11}^{\text{hom}} = (3\mu + 8k_2) \cdot \varepsilon_{11} = E_1^{\text{hom}} \cdot \varepsilon_{11}. \quad (75)$$

The tensile force acting on the section will be

$$P^{\text{hom}} = \int_S \sigma_{11}^{\text{hom}} dS = S \cdot \sigma_{11}^{\text{hom}} = S \cdot (3\mu + 8k_2) \cdot \varepsilon_{11}. \quad (76)$$

As to the heterogeneous model, the tensile force in linearized case is as follows:

$$P^{\text{het}} = \int_S \sigma_{11}^{\text{het}} dS = S \cdot ((1 - \psi_f) \cdot E_m + \psi_f \cdot E_f) \cdot \varepsilon_{11}, \quad (77)$$

where ψ_f is the fiber volume fraction and E_m and E_f are matrix and fiber moduli.

Consequently, we have condition

$$(3\mu + 8k_2) \cdot \varepsilon_{11} = ((1 - \psi_f) \cdot E_m + \psi_f \cdot E_f) \cdot \varepsilon_{11}, \quad (78)$$

and so it follows that

$$k_2 = \frac{1}{8} ((1 - \psi_f) \cdot E_m + \psi_f \cdot E_f - 3\mu). \quad (79)$$

References

1. Forest, S., & Sievert, R. (2006). Nonlinear microstrain theories. *International Journal of Solids and Structures*, 43, 7224–7245.
2. Cosserat, E., & Cosserat, F. (1909). *Théorie des corps déformables*. Paris: A. Hermann et Fils.
3. Eringen, A. C. (1962). *Nonlinear theory of continuous media*. New York: McGraw-Hill.
4. Altenbach, J., Altenbach, H., & Eremeyev, V. A. (2010). On generalized Cosserat-type theories of plates and shells: A short review and bibliography. *Archive of Applied Mechanics*, 80, 73–92.
5. Koiter, W. T. (1964). Couple stresses in the theory of elasticity I and II. *Proceedings of the Koninklijke Nederlandse Akademie van Wetenschappen*, 67, 17–44.
6. Spencer, A. J. M. (1972). *Deformations of fibre-reinforced materials*. London: Oxford University Press.
7. Forest, S., & Sab, K. (1998). Cosserat overall modelling of heterogeneous materials. *Mechanics Research Communications*, 25(4), 449–454.

8. de Borst, R. (1993). A generalisation of J_2 —Flow theory for polar continua. *Computer Methods in Applied Mechanics and Engineering*, 103, 347–362.
9. Sansour, C., Skatulla, S., & Zbib, H. (2010). A formulation for the micromorphic continuum at finite inelastic strains. *International Journal of Solids and Structures*, 47, 1546–1554.
10. Isbuga, V., & Regueiro, R. A. (2011). Three-dimensional finite element analysis of finite deformation micromorphic linear isotropic elasticity. *International Journal of Engineering Science*, 49, 1326–1336.
11. Tsiatas, G. C. (2009). A new Kirchhoff plate model based on a modified couple stress theory. *International Journal of Solids and Structures*, 46, 2757–2764.
12. Park, S. K., & Gao, X.-L. (2006). Bernoulli–Euler beam model based on a modified couple stress theory. *Journal of Micromechanics and Microengineering*, 16, 2355–2359.
13. Lam, D. C. C., Yang, F., Chong, A. C. M., Wang, J., & Tong, P. (2003). Experiments and theory in strain gradient elasticity. *Journal of the Mechanics and Physics of Solids*, 51, 1477–1508.
14. Bauer, S., Schäfer, M., Grammenoudis, P., & Tsakmakis, C. (2010). Three-dimensional finite elements for large deformation micropolar elasticity. *Computer Methods in Applied Mechanics and Engineering*, 199, 2643–2654.
15. Chen, W., & Si, J. (2013). A model of composite laminated beam based on the global–local theory and new modified couple-stress theory. *Composite Structures*, 103, 99–107.
16. Fleck, N. A., & Shu, J. Y. (1995). Microbuckle initiation in fibre composites: A finite element study. *Journal of the Mechanics and Physics of Solids*, 43(12), 1887–1918.
17. Spencer, A. J. M., & Soldatos, K. P. (2007). Finite deformations of fibre-reinforced elastic solid with fibre bending stiffness. *International Journal of Non-Linear Mechanics*, 42, 355–368.
18. Zheng, Q.-S. (1994). Theory of representations for tensor functions. *Applied Mechanics Reviews*, 47, 554.
19. Toupin, R. A. (1962). Elastic materials with couple-stresses. *Archive for Rational Mechanics and Analysis*, 11, 385.
20. Soldatos, K. P. (2013). Foundation of polar linear elasticity for fibre-reinforced materials. *Journal of Elasticity*, 114(2), 155–178.
21. Holzapfel, G. A. (2000). *Nonlinear solid mechanics. A continuum approach for engineering*. Chichester: Wiley.
22. Lasota, T. (2013). *Computational modelling of mechanical behaviour of “elastomer-steel fibre” composite*. Dissertation, Brno University of Technology, Brno.
23. Timmel, M., Kolling, S., & Kaliske, M. (2007). *Phenomenological and micromechanical modeling of anisotropic effects in hyperelastic materials*. LS-DYNA FORUM 6, Frankenthal
24. Soldatos, K. P. (2010). Second-gradient plane deformations of ideal fibre-reinforced materials: Implications of hyper-elasticity theory. *Journal of Engineering Mathematics*, 68(1), 99–127.
25. Lasota, T., Burša, J., & Fedorova, S. (2012). *Constitutive equations and finite element formulation for anisotropic hyperelastic composites based on constrained Cosserat continuum*. Paper presented at the European Congress on Computational Methods in Applied Sciences and Engineering, Vienna, Austria, September 10–14, 2012.
26. Huebner, K. H., Dewhirst, D. L., Smith, D. E., & Byrom, T. G. (2001). *The finite element method for engineers* (4th ed.). New York: Wiley-InterScience.
27. Su, W., & Liu, S. (2010). Size-dependent optimal microstructure design based on couple-stress theory. *Structural and Multidisciplinary Optimization*, 42, 243–254.

Towards Fiber Bundle Models for Composite Pressure Vessels

Jörg B. Multhoff

Abstract Finite element models for composite pressure vessels (CPV) are usually based on the assumptions of the classical laminate theory (CLT). In the CLT, the composite laminate is represented by a stack of homogeneous plies. Each ply is described by thickness, material orientation angle, and anisotropic mechanical properties. For filament wound CPV, each layer is frequently modeled by two unidirectional plies with opposite fiber angles. Ply thickness and fiber angle in each layer vary throughout the laminate depending on vessel geometry and fiber path. The thickness buildup due to the band overlap is usually described by analytical or semi-empirical formulas. Close observation of the actual fiber architecture of filament wound CPV reveals that this model is only a convenient simplification. The reality can be modeled more closely by an enhanced filament winding simulation which tracks the deposition of a finite-width band on the winding surface. However, it is not clear how to transform this detailed laminate information into a suitable finite element model based on CLT. The classical modeling approach uses layered shell or layered solid elements to model the laminate. This requires the use of a certain number of plies, each with unique angle and thickness within every layered finite element. However, a mesh layout representing the detailed description of the real laminate within the framework of CLT is hard to envision. In the present contribution, it is proposed to model the filament wound band as a group of fiber bundles following the real fiber path on the winding surface. The fiber bundles are embedded in a structured mesh representing the matrix material. This fiber bundle approach may be the appropriate bridge between micro- and macro-descriptions of the composite materials resulting from filament winding. In this contribution, the main idea of the fiber bundle approach is motivated, explored, and compared with modeling strategies based on layered solid elements. The fiber bundle approach may be extended to filament wound, fiber-placed, or braided structures with partial surface coverage which are even more difficult to describe by CLT.

J.B. Multhoff (✉)
ISATEC GmbH, Rathausstr. 10, 52072 Aachen, Germany
e-mail: j.multhoff@isatec-aachen.de

1 Introduction

The importance of gas storage for mobile applications is steadily growing. This leads to a rising demand for light-weight composite pressure vessels (CPVs). However, the behavior of composite structures is unintuitive and not easy to predict. The safe and efficient design of CPVs therefore requires thorough analysis. This is in particular true for high performance applications like hydrogen tanks for mass market automotive applications [1].

Important features of composite materials and filament winding are described briefly to give the necessary background for the discussion of finite element analysis methods for CPV and to motivate the present work.

1.1 Fibrous Composite Materials

Structural composites are generally defined as materials consisting of two or more phases on a macroscopic scale, whose mechanical performance are designed to be superior to those of the constituent materials acting independently [2]. In particular, fiber-reinforced plastic materials consist of stiff and strong fibers embedded in a soft matrix material. Material in fiber form exhibits the highest tensile strength of all known material forms. However, the strength of the fiber is reduced with increased length due to the higher probability of a local weakness. Embedding a multitude of parallel fibers at high volume fraction in a soft matrix material with sufficient adhesion enables them to share loads and to mitigate the consequences of local failure, among other benefits.

It is important to note that this unidirectional fiber-reinforced composite material has excellent stiffness and strength properties only in fiber direction, Tables 1 and 2. In general, it is necessary to combine multiple stacked layers of unidirectional material with different fiber directions in a laminate to accommodate all loads acting on a structure. The resulting laminate properties usually still show a high directional dependency. Recognizing that the matrix dominated strength properties are much less certain and reproducible than the strength in fiber direction, it is clear that the design should generally not depend on them strongly. Realizing the benefits of fiber-reinforced composite materials for demanding structural application requires a considerably higher analysis effort than the use of traditional structural materials.

Table 1 Illustrative unidirectional CFRP elastic properties (in-plane) [3]

Description	Symbol	Value
Parallel modulus	E_1	171.4 GPa
Transverse modulus	E_2	9.08 GPa
Shear modulus	G_{12}	5.29 GPa
Major Poisson's ratio	ν_{12}	0.32

Excellent stiffness properties exist only in fiber direction

Table 2 Illustrative unidirectional CFRP strength properties (in-plane) [3]

Description	Symbol	Value
Parallel tensile strength	R_1^+	2326.2 MPa
Parallel compressive strength	R_1^-	1200.1 MPa
Transverse tensile strength	R_2^+	62.3 MPa
Transverse compressive strength	R_2^-	199.8 MPa
Shear strength	R_6	92.3 MPa

Excellent strength properties exist only in fiber direction

1.2 Filament Winding

Filament winding is one of the oldest manufacturing methods for structural composites [4]. Wet winding has the advantage of using the raw materials, fiber and resin, in its direct form without intermediate processing steps. The manufacturing speed measured in mass per time is among the highest in comparison to other methods. In sum, this contributes to relatively low manufacturing costs for filament wound composite parts compared to other methods [5] and explains its continued importance.

In the filament winding process, multiple rovings or tows, each composed of thousands of individual filaments, are formed to a flat band and are impregnated with a matrix material, usually a resin. A typical fiber volume fraction V_f is 60%. The band is continuously deposited on a rotating mandrel, eventually covering the entire surface, Fig. 1. The resulting winding pattern consists of multiple cycles; in each cycle, the band follows a specific path along the winding surface, Fig. 2. This path is characterized by a certain angle α of the band and thus the fibers relative to the *meridian* of the winding surface. Usually the cylindrical part of the vessel is covered in such a way that the resulting layer is composed of two bands with opposite fiber angles ($+\alpha/ -\alpha$) at each location. However, considerable band overlap occurs in the domes leading to a characteristic thickness build-up at the polar openings.

Notable characteristics of the filament wound structure are the distribution of the winding angle and the layer thickness along the winding surface as well as the crossing points that lead to a certain interweaving of the layers, Fig. 1. The details depend on the winding pattern. Usually, winding angle and thickness are constant in the cylindrical part of the vessel and assume minimum values (α_0, t_0).

1.3 Analysis of Composite Pressure Vessels

Different analysis methods are available and in use for CPVs [6]. All have to take into account the special features arising in the filament wound composite structure as described before. Netting analysis deserves special mention as the first analysis method for composite pressure vessels, introducing the important concept and design principle that the fiber network takes all the loads [5]. However, only finite element analysis has the potential to model all relevant effects with

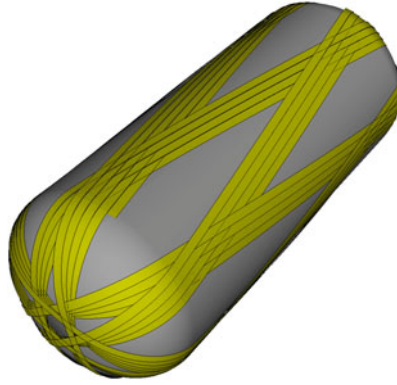


Fig. 1 Filament winding: Multiple parallel rovings of unidirectional material are placed on a rotating mandrel in a prescribed pattern (partial winding shown for clarity). The resulting laminate possesses characteristic fiber angle and layer thickness distributions as well as a certain interweave of plies and associated fiber crossing points

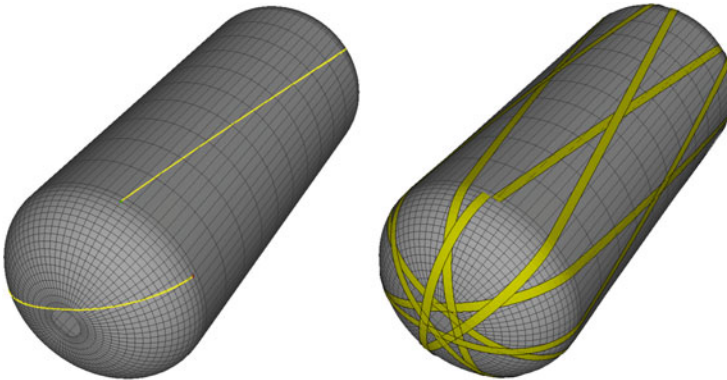


Fig. 2 Fiber path (*left*) and unidirectional band (*right*) on the winding surface. Only three cycles are shown for clarity. Full surface coverage results in a characteristic winding pattern

sufficient accuracy. Finite element methods for composite materials and structures are discussed in [7]. A review of finite element analysis methods specifically for filament wound CPVs was given in [8].

2 Filament Winding Simulation

The effects of the filament winding process on the resulting fiber architecture is not self-evident and requires analysis by filament winding simulation. The filament winding simulation was originally developed to generate suitable winding patterns and to program the automatic filament winding machine [5].

2.1 Fiber Path

The wet fiber can be deposited on the surface only on—or close to—a *geodesic* path without slipping. On a surface of revolution with local radius r , the geodesic path is given by Clairaut's theorem [4, 5]:

$$r \sin(\alpha) = \text{const.} \quad (1)$$

The fiber is tangent at the polar opening with radius r_p , i.e., $\alpha(r_p) = 90^\circ$. These layers are called helical layers. For geodesic winding, the fiber angle at each radius can be evaluated by Eq. (2).

$$\alpha(r) = \arcsin\left(\frac{r_p}{r}\right) \quad (2)$$

Figure 3 shows an example for this fiber angle distribution. Some deviation from this path is possible if the surface friction or material adhesion is exploited.

Layers with a constant winding angle close to 90° are called hoop layers and can only be applied in the cylindrical part of the vessel. The polar opening radius of these layers is equal to or close to the radius in the cylindrical part of the vessel. Practical designs require multiple helical and hoop layers each with different winding angle α_0 and corresponding polar opening diameters.

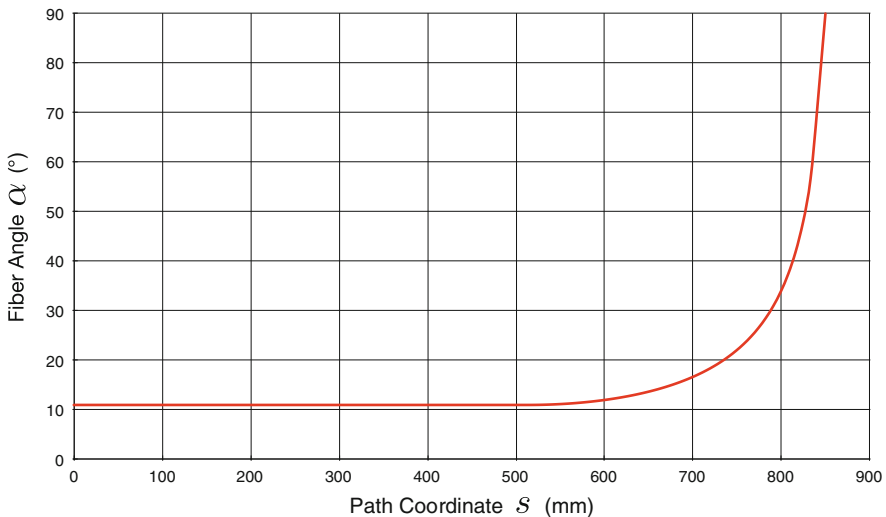


Fig. 3 Example of the fiber angle distribution along the meridian path according to Eq. (2). The fiber angle relative to the meridian is minimal in the cylindrical part (α_0) and assumes a value of 90° at the polar opening

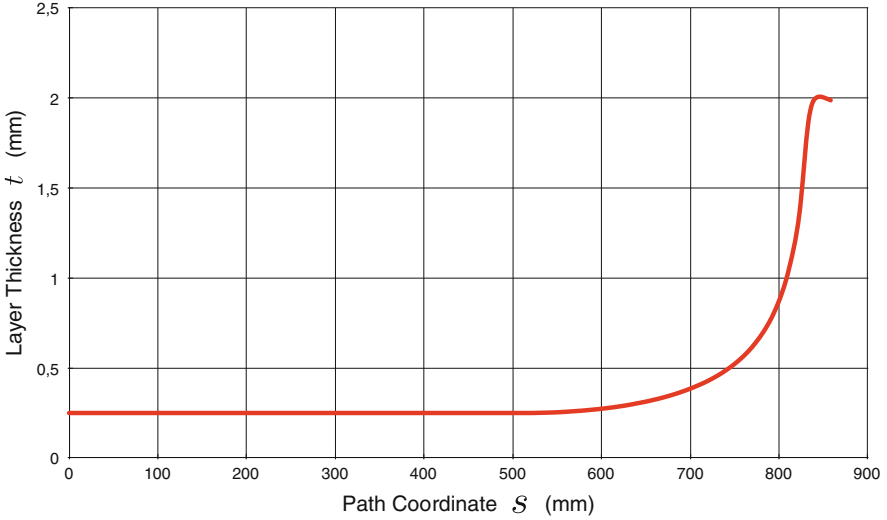


Fig. 4 Example of the layer thickness distribution along the meridian path. The layer thickness is minimal in the cylindrical part (t_0) and increases in the dome towards the polar opening due to band overlap. This effect depends on the fiber bandwidth w and the winding pattern

2.2 Layer Thickness

One feature of the continuous filament winding process is that each *parallel* of the winding surface is crossed by the same number of fibers. This results in a constant layer thickness in the cylindrical part of the vessel. However, the layer thickness increases with decreasing vessel radius. This is a consequence of the progressive band overlap that can be easily recognized in Figs. 1 and 6. This behavior can be approximately described by Eq. (3) up to a certain distance from the polar opening. The resulting layer thickness distribution is shown in Fig. 4.

$$t(r) = t_0 \frac{r_0 \cos(\alpha_0)}{r \cos(\alpha)} \quad (3)$$

Improved prediction of the layer thickness is possible by empirical or analytical methods [6] and application of the enhanced filament winding simulation.

2.3 Enhanced Filament Winding Simulation

The main differences between the real fiber architecture of filament wound vessels and the idealized theory as described above can be recognized by explicit consideration of the finite fiber bandwidth w in an enhanced version of the filament winding simulation.

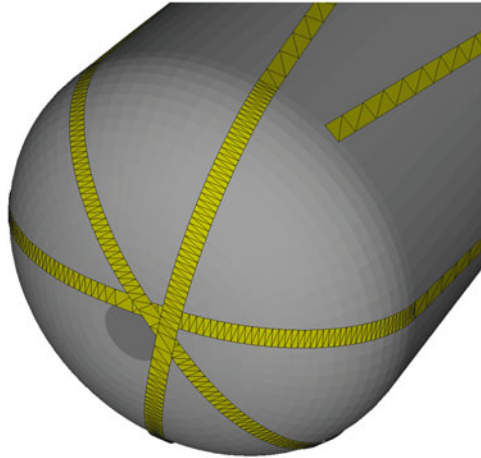


Fig. 5 Representation of the filament wound band by triangular patches. (Only three cycles are shown for clarity). The local thickness is computed by accumulation of these triangular patches at sampling points on the winding surface [9]

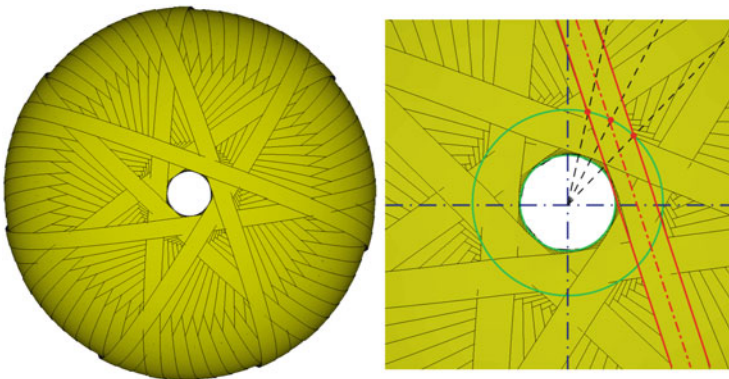


Fig. 6 Overlap of the unidirectional band in the dome (*left*) and near the polar opening (*right*). The fiber angle relative to the meridian is not unique at a given parallel due to the finite fiber bandwidth w

After computing the fiber path, the geometry of the fiber band, usually consisting of multiple parallel fiber strands, is modeled, Fig 2. The fiber band is represented by patches of triangles connecting consecutive bounding points, Fig. 5. The local thickness is computed by accumulation of band patches at sampling points on the winding surface. Likewise the local laminate stacking sequence at any sampling point can be computed. Details are presented in [9].

2.4 Local Laminate Properties

The main results of the simulated band deposition on the winding surface are consistent with observations that can also be made with actual vessels manufactured by filament winding. The differences between the real laminate structure and the idealized theory are mainly due to the finite width w of the filament band. They are reduced with decreasing width of the band. Additional differences may exist due to fiber bridging effects, band taper, band splitting, etc. (Fig. 6).

The main observations are:

1. The effective thickness distribution along the meridian direction is not continuous as shown in Fig. 4 but stepped due to the band overlap, Fig. 7.
2. The thickness at a given meridian position in circumferential direction is not constant but variable and depends on the winding pattern.
3. The local fiber angle within a layer at a given meridian and circumferential position is not constant in the circumferential direction (Fig. 6) and is in general not given by Clairaut's theorem as shown in Fig. 3

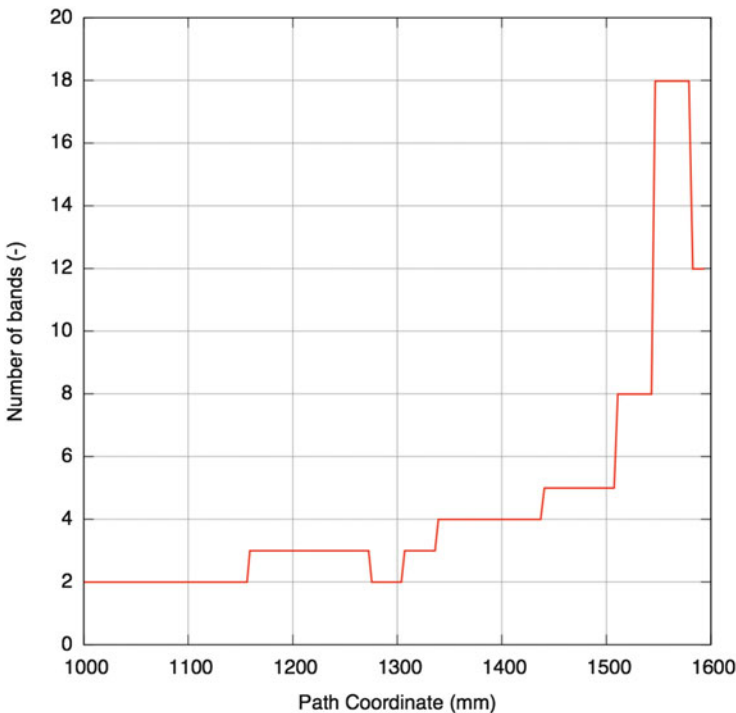


Fig. 7 Example of the stepped thickness distribution along a meridian path. The thickness build-up in the dome towards the polar opening is due to the increasing band overlap. The thickness distribution is not axisymmetric but depends on the winding pattern

In sum, the important local properties fiber angle and layer thickness possess a discontinuous distribution in the laminate. For optimized composite pressure vessel designs, it is of high interest to examine the effects of these observations on the structural behavior.

2.5 Representation of Local Properties in the Analysis Model

The transfer of the laminate data generated by the enhanced filament winding simulation into the finite element model may proceed as follows: In the simplest case, the grid points representing the winding surface are used as nodal points of the finite element discretization. The finite elements may be shell or solid elements. However, only solid elements allow for the required detailed analysis. In the case of solid elements, the grid points represent the nodes on the inner surface, and the nodes on the outside surface are generated using the normal vectors of the winding surface and the thickness data. The required thickness information for each node is taken from the accumulated band thickness at the nodal points. Depending on the element type, the internal laminate description may allow for multiple layers with constant thickness and constant angle of principle material direction or for variable thickness layers with variable angle of principle material direction. In the latter case, the thickness and angle data usually have to be input at the nodal points. However, most finite element formulations require that the layers are continuous within the element and thus that the number of layers is the same at all nodes.

It turns out that this may not be the case for general filament wound structures. The easiest solution to this problem is to use a sampling point in the center of the element to record the local laminate stacking sequence and to use this data to define the laminate corresponding to the entire element. This may represent the real stiffness and strength distribution poorly. A more accurate approach may be to use the location of the in-plane integration points of the element as the sampling points, e.g., for 4×4 in-plane Gauss integration. Different laminate stacking sequences with individual number of layers would result at the in-plane integration points, making special element formulations necessary.

In general, the finite element discretization is not predetermined by this scheme but can be adjusted to fit the accuracy to practical needs. It is only necessary to define the location of the desired sampling points on the winding surface and to map these sampling points to the appropriate finite elements. However, a mesh layout which respects the detailed description of the real laminate as shown, e.g., in Fig. 6 within the framework of a laminate theory is hard to envision.

To avoid the mentioned problems, in the present contribution it is proposed to model the filament wound band as a group of fiber bundles following the real fiber path on the winding surface. The fiber bundles are embedded in a structured mesh representing the matrix material as described below.

3 Finite Elements for Filament Wound Structures

The finite element analysis of composite laminates based on the assumptions of the classical laminate theory (CLT) is described, e.g., in [7]. The most appropriate representation, especially for thick-walled vessels, can be achieved using layered solid elements, Fig. 8. In general, multiple elements in thickness direction are necessary [8]. Shell elements are beyond the scope of this discussion.

3.1 Layered Solid Element

The concept of the layered solid element is reviewed in two versions for constant and for variable layer thickness. Aspects of geometric nonlinearity and element technology are neglected for simplicity. Only the formulation of the element stiffness matrix is considered. The notation of the original sources is preserved.

3.1.1 Constant Layer Thickness

One example for the formulation of the layered solid element for constant thickness layers is proposed in [10]. Using the isoparametric concept, the stiffness matrix $[KF]$ can be evaluated by Eq. (4) in terms of the strain interpolation matrix $[BF]$, the constitutive matrix $[EI']$, and the Jacobian matrix $[J]$ in the standard way [11].

$$[KF] = \int_{-1}^{+1} \int_{-1}^{+1} \int_{-1}^{+1} [BF]^T [EI'] [BF] \det[J] d\xi d\eta d\zeta \quad (4)$$

The integral can be evaluated by numerical integration. However, the constitutive matrix $[EI']$ is not continuous in the element but is different from layer to layer due to the necessary transformation from the principle directions of the orthotropic material to the global coordinate directions. This is handled by splitting the integration limits through each layer. For the application of the Gauss quadrature formula, the integration limits within each layer should be from -1 to $+1$. This is achieved by a

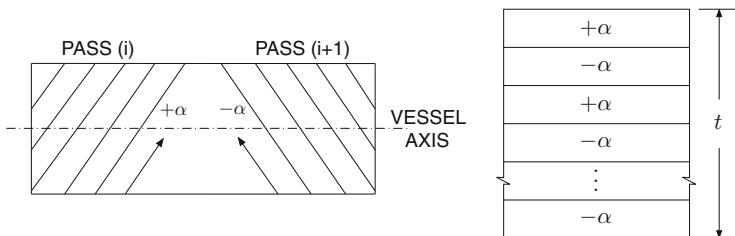


Fig. 8 Representation of the filament wound composite pressure vessel wall using CLT [10]. Each layer is represented by two plies with opposite fiber angle α

change of variable for the thickness coordinate ζ as formulated in Eq. (5).

$$\zeta = -1 + \frac{1}{t} \left[-h_k(1 - \zeta_k) + 2 \sum_{j=1}^k h_j \right] \quad (5)$$

Using this equation, the thickness coordinate ζ_k in layer k varies from -1 to $+1$ and the change of variable involves effectively a scaling factor for the layer thickness h_k relative to the total element thickness t :

$$d\zeta = \left(\frac{h_k}{t} \right) d\zeta_k \quad (6)$$

With this substitution for $d\zeta$ the stiffness matrix in Eq. (4) can be evaluated as the sum over all n layers contained in the element.

$$[KF] = \sum_{k=1}^n \int_{-1}^{+1} \int_{-1}^{+1} \int_{-1}^{+1} [BF]^T [E'] [BF] \det[J] \frac{h_k}{t} d\xi d\eta d\zeta_k \quad (7)$$

This formulation illustrates the idea of the layered solid element very well but is of limited applicability for filament wound structures with variable layer thickness.

3.1.2 Variable Layer Thickness

An element formulation allowing for variable element thickness—among other features—is proposed in [12]. Here only the integration scheme for the linear stiffness matrix is considered. The element geometry is interpolated with trilinear shape functions \bar{N}_i . After the usual first isoparametric map, a second isoparametric map for each layer is introduced, Fig. 9. The coordinates $\xi = [\xi^1, \xi^2, \xi^3]^T$ of the first map are interpolated in terms of the coordinates $r = [r^1, r^2, r^3]^T$ of the second map using Eqs. (8) and (9). ξ_i contains the coordinates of the layer under consideration.

$$\xi = \sum_{i=1}^{nnode} \bar{N}_i \xi_i \quad (8)$$

$$\bar{N}_i = \frac{1}{8} (1 + r^1 r_i^1) (1 + r^2 r_i^2) (1 + r^3 r_i^3) \quad (9)$$

The components of the element stiffness matrix \mathbf{K}_{eIJ} are evaluated by summation over all layers $nlay$ and over all integration points $ngaus$:

$$\mathbf{K}_{eIJ} = \sum_{L=1}^{nlay} \sum_{gp=1}^{ngaus} \mathbf{B}_I^T(\xi_{gp}^L) \mathbb{C}_L \mathbf{B}_J(\xi_{gp}^L) \det \mathbf{J}(\xi_{gp}^L) \det \mathbf{J}^L(\mathbf{r}_{gp}^L) w_{gp}^L \quad (10)$$

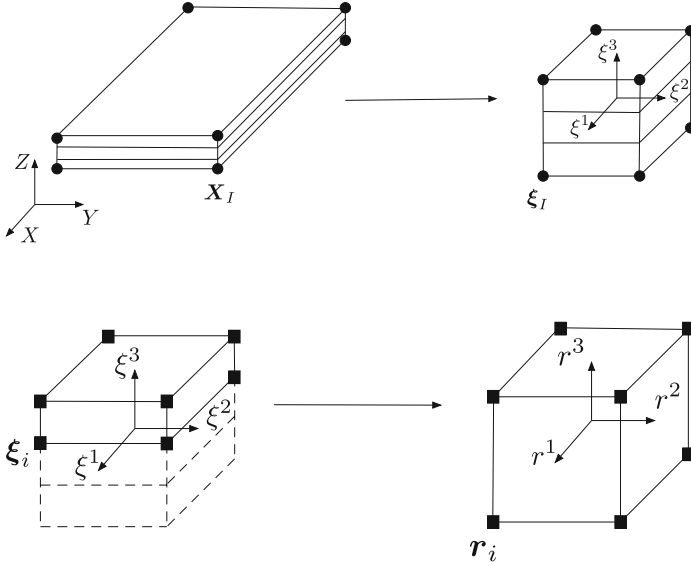


Fig. 9 First and second isoparametric map for integration of layered elements [12]

Here, \mathbf{J} and \mathbf{J}^L are the Jacobian matrix of the first and second map, and w_{gp}^L are the weighting factors of the integration point. \mathbf{B} is the strain interpolation matrix and \mathbf{C}_L is the constitutive matrix in layer L .

For the modeling of a filament wound structure with a stack of layered solid elements with variable layer thickness, the total laminate must be mapped on the laminate pertaining to the individual elements, Fig. 12. For practical applications, this step requires special software [1].

3.2 Reinforcing Element

The application of truss elements embedded in solid elements for the modeling of dry filament wound pressure vessels was proposed in [13]. This can be realized by constraining the nodal degrees of freedom of the truss element to the degrees of freedom of the embedding solid element. Thus, the displacement field of the solid element imposes the displacements of all embedded truss elements.

The same effect can be achieved by classical reinforcing elements as described e.g., in [14]. Here, the degrees of freedom of the reinforcing element $\{u_{II}, v_{II}, w_{II}\}^T$ are expressed in terms of the degrees of freedom of the embedding element

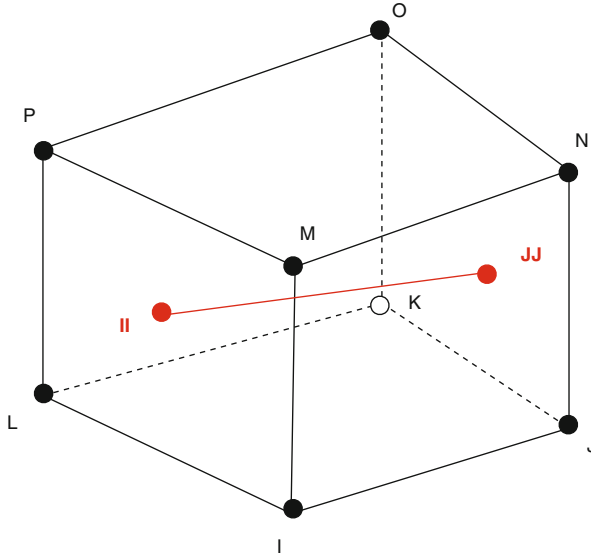


Fig. 10 Reinforcing element: Reinforcement embedded in a solid element. The deformation of the reinforcement $\{u_{II}, v_{II}, w_{II}\}^T$ is defined by the deformation of the embedding element $\{u_i, v_i, w_i\}^T$

by way of the eight trilinear shape functions of the embedding element N_i by Eq. (11), Fig. 10.

$$\begin{Bmatrix} u_{II} \\ v_{II} \\ w_{II} \end{Bmatrix} = \sum_{i=1}^8 N_i(\xi_{II}, \eta_{II}, \zeta_{II}) \begin{Bmatrix} u_i \\ v_i \\ w_i \end{Bmatrix} \quad (11)$$

Using this transformation, the stiffness matrix of the reinforcing element can be expressed in terms of the degrees of freedom of the embedding element and superimposed to form the total stiffness. Typically, the reinforcing element allows the definition of multiple reinforcing members. This formulation is restricted to unidirectional reinforcement in the direction of the reinforcing members. This may be appropriate for the modeling of dry filament wound structures without use of matrix materials or for analysis on the basis of the assumption of netting analysis.

For the modeling of a filament wound structure, the global fiber architecture must be mapped on the reinforcing members in the individual elements. This can be accomplished by post-processing the results of the enhanced filament winding simulation.

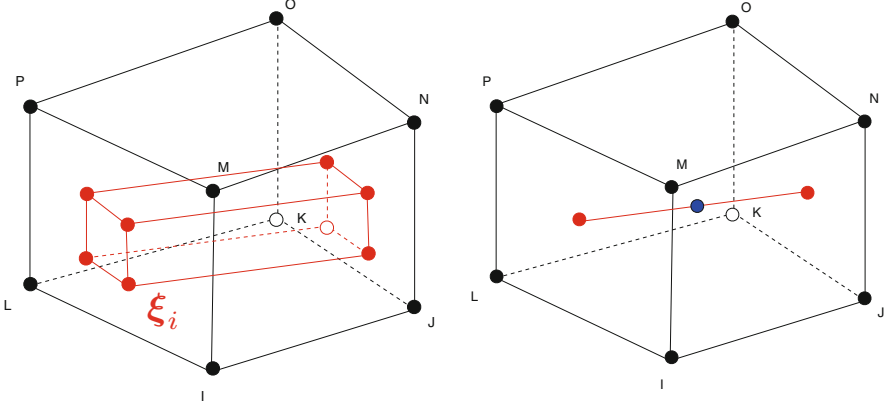


Fig. 11 Fiber bundle element, first variant with prismatic fiber bundle volume (*left*) and second variant with one-dimensional representation of the fiber bundle volume (*right*)

3.3 Fiber Bundle Element

The idea of the fiber bundle element is to form a *synthesis* of the layered element and the reinforcing element as a practical meso-level model for the fiber architectures arising from filament winding or similar manufacturing methods.

In a first variant, the geometry of each fiber bundle is modeled by a prismatic shape that can be mapped on a cube. This variant is similar to the layered element with variable layer thickness as described before but has a generalized geometry of the second isoparametric map, Fig. 11. ξ_i in Eq. (8) now contains the coordinates of the fiber bundle under consideration. This variant of the fiber bundle element may use the same Gauss integration formula as the layered element (Fig. 12).

In a second variant, each fiber bundle is modeled by a volume simply computed from length and cross-section area. This variant is similar to the reinforcing element described before but allows the alternative use of a one-dimensional or a three-dimensional constitutive model. In the latter case, the reinforcement is not purely unidirectional. This variant could use a one-point integration rule.

The components of the element stiffness matrix for both variants are evaluated as follows:

$$\mathbf{K}_{eIJ} = \sum_{B=1}^{nbundle} \sum_{ip=1}^{nip} \mathbf{B}_I^T(\xi_{ip}^B) \mathbf{C}_B \mathbf{B}_J(\xi_{ip}^B) \det \mathbf{J}(\xi_{ip}^B) \det \mathbf{J}^B(\mathbf{r}_{ip}^B) w_{ip}^B \quad (12)$$

The differences between the two variants are the number of integration points, the effective formulas for the Jacobian matrix of the second isoparametric map \mathbf{J}^B and the weighting factor w_{ip}^B of the integration points. \mathbf{C}_B is the constitutive matrix for the fiber bundle B . For both variants, an additional contribution may be added to represent the effect of the embedding matrix material.

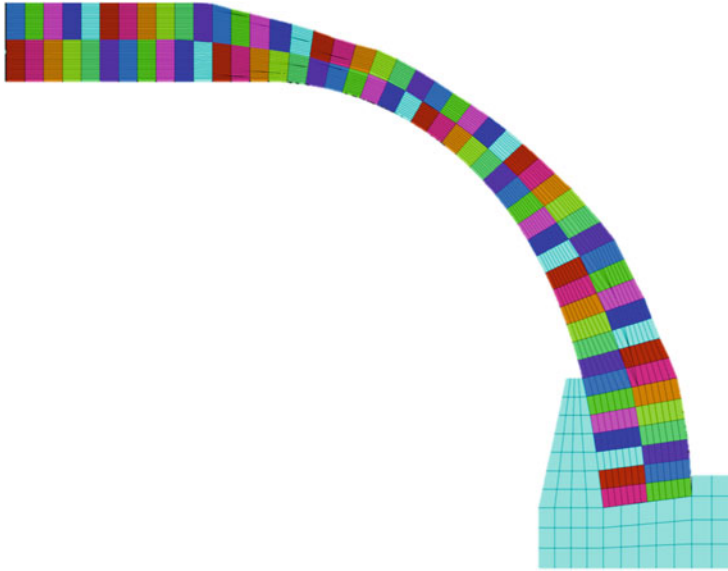


Fig. 12 Cross section of finite element model based on layered solid elements [1] (Two elements in *thickness direction* shown for clarity). Each element has individual properties to describe the laminate stack. Two computational layers with opposite fiber angle are used to represent one filament wound layer. The ply drop-off can be modeled using variable layer thickness

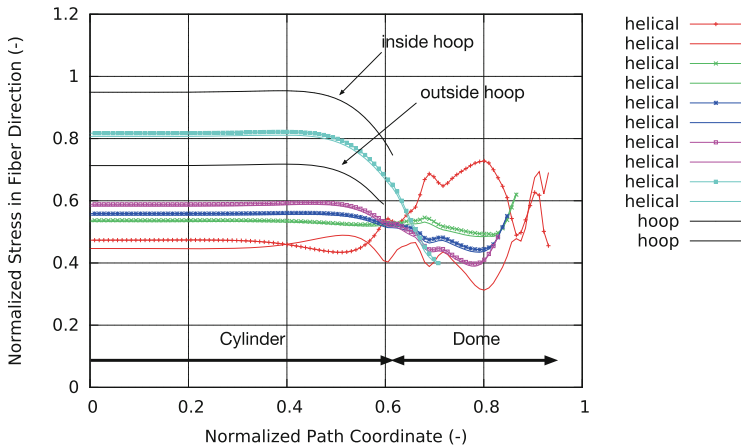


Fig. 13 Typical layer-wise evaluation of finite element results [1]. An axisymmetric stress distribution is usually assumed. The fiber bundle model promises more detailed results, especially in the vicinity of the polar openings of the composite shell

The first variant may be more costly than the second variant due to the higher number of integration points. However, evaluation of the relative efficiency is subject to verification of the element behavior and requires more research (Fig.13).

4 Conclusions

The enhanced filament winding simulation confirms the observation that filament wound composite pressure vessel structures possess discontinuous fiber angle and layer thickness distributions. This poses difficulties for the accurate modeling using layered elements based on the assumptions of the CLT. Consideration of the implementation of layered solid elements and reinforcing elements motivates the formulation of a fiber bundle element that may be more effective for the analysis of filament wound structures. Implementation of this concept is proceeding and requires further work in the infrastructure of the enhanced filament winding simulation and in testing of the fiber bundle element. The fiber bundle approach may be the appropriate bridge between micro- and macro-descriptions of the composite materials resulting from filament winding and may be extended to structures arising from fiber placement and braiding processes. The results are relevant for the safe and economic design of optimized high pressure hydrogen tanks for automotive applications.

References

1. Multhoff, J. B., & Krieger, J. (2010). Effective structural design procedure for composite hydrogen tanks. In *18th World Hydrogen Energy Conference 2010*, Essen.
2. Daniel, I. M., & Ishai, O. I. (1994). *Engineering mechanics of composite materials*. Oxford: Oxford University Press.
3. Barbero, E. J. (2011). *Introduction to composite materials design* (2nd ed.). Boca Raton: CRC Press.
4. Rosato, D. C., & Grove, C. S. (1964) *Filament winding: Its development, manufacturing, application, and design*. New York: Wiley.
5. Peters, S. T., Humphrey, W. D., & Foral, R. F. (1999). *Filament winding composite structure fabrication* 2nd (ed.). Covina, CA: SAMPE Publishers.
6. Vasiliev, V. V. (2009). *Composite pressure vessels: design, analysis and manufacturing*. Blacksburg: Bull Ridge.
7. Ochoa, O. O., & Reddy, J. N. (1992). *Finite element analysis of composite laminates*. Dordrecht: Kluwer Academic Publishers.
8. Multhoff, J. B., Krieger, J., Loures da Costa, L. E. V., & Betten, J. (2001). Problems in high-resolution finite element models of composite rocket motor cases. In *Proceedings of COBEM 2001* (Vol. 6, pp. 207–216), Uberlândia.
9. Multhoff, J. B. (2013). Enhanced filament winding simulation for improved structural analysis of composite pressure vessels. In *The 19th International Conference on Composite Materials* (pp. 9150–9158), Montreal.
10. Hoa, S. V., Yu, C. W., & Sankar, T. S. (1985). Analysis of filament wound vessel using finite elements. *Composite Structures*, 3, 1–18.
11. Zienkiewicz, O. C., & Taylor, R. L. (2005). *The finite element method* 6th (ed.). Oxford: Elsevier.
12. Klinkel, S., Gruttmann, F., & Wagner, W. (1999). A continuum based three-dimensional shell element for laminated structures. *Computers and Structures*, 71, 43–62.

13. Koppert, J. J., de Boer, H., Weustink, A. P. D., Beukers, A., & Bersee, H. E. N. (2007). Virtual testing of dry filament wound thick walled pressure vessels. In *The 16th International Conference on Composite Materials*, Kyoto.
14. Hofstetter, G., & Mang, H. A. (1995). *Computational mechanics of reinforced concrete structures*. Braunschweig: Vieweg.

A Macro Model for 3D Fiber-Reinforced Polymer Composites

Pedro V. Marcal, Jeffrey T. Fong, and Nobuki Yamagata

Abstract A finite element Macro Model is proposed for the analysis of continuous and discontinuous 3D fiber-reinforced polymer composites (FRPCs). The Macro Model is made by modeling the matrix and each fiber layer as a parallel and geometrically similar elements, respectively. The yield strength of the material is modeled by an elastic-plastic Mises material with linear work-hardening. The fiber yielding is modeled by an additional negative work-hardening curve with values approaching that of its Young's modulus to simulate failure after the maximum plastic strain is reached. A series of case studies is used to illustrate the facets of the model and compare the results with experiment. In most cases, and using carbon fiber, it was found that premature failure occurred by fracture. A fracture analysis model was proposed as an extension to the model by introducing a numerical approximation of the classical fracture mechanics theory.

1 Introduction

A fiber-reinforced polymer composite (FRPC) has a very complex behavior that spans several scales of physical dimensions due to the interaction between the resin matrix and the fiber reinforcement. In this paper, we confine our model to the simplest finite element model possible for the FRPC. We generalize the Macro

Contribution of the National Institute of Standards and Technology. Not subject to copyright.

P.V. Marcal (✉)

MPACT Corp., 6643, Buttonwood Ave., Oak Park, CA, 91377 USA

e-mail: pedrovmarcal@gmail.com

J.T. Fong

Applied and Computational Mathematics Division, National Institute of Standards & Technology (NIST), 100 Bureau Drive, Mail Code 8910 Gaithersburg, MD, 20899-8910 USA

e-mail: fong@nist.gov

N. Yamagata

Advanced Creative Technology Co., Ltd., 1-8-3 Shibuya, Shibuya-ku, Tokyo, 150-0002 Japan

e-mail: yamagata@actact.co.jp

Model first used by Buyukozturk and Marcal [1] for reinforced concrete. This model allows us to simplify the problem to just one physical scale, and because of the simplification in computing, we were also able to explore many complex material failure modes in which the FRPC could fail.

There are two paths to failure caused by nonlinear material behavior of the fiber that requires modification of the straightforward nonlinear elastic-plastic behavior and that is due to the reduced maximum tensile strain compared to metals. In our model, we account for this by introducing a negative work-hardening of the order of the elastic modulus once the maximum tensile strain is reached.

In nonlinear analysis with the Macro Model, it was soon discovered that fracture mechanics formed a lower bound to our models, particularly when carbon fiber is used. In this study, we present our Macro Model and apply it to problems with continuous fibers as well as discrete fibers. We compare our results with experiments. The study is confined to layered planar fiber reinforcement, although we provide a preliminary result that includes stitching in the third direction to show that such problems in 3D can be handled by our model. It is noted here that even though the FRPC layers may be in plane stress, a fracture mechanics analysis involves fracture through the thickness so that it requires a full 3D analysis.

In the current work, we show the importance of 3D fracture mechanics in predicting the failure of even simple specimens. We point out the difference between fracture of continuous fiber composites (CFC) and fracture of homogeneous materials. Fracture initiation occurs along lines of fiber directions where the structural weakness was discernible. This is a necessary part of the analysis since it often differs from the intuitive paths that the loading would have suggested. In fact, the necessity of assuming a failure path is so critical that we choose to call it the “Principle of Feasible Failure Paths in FRC” (Feasibility Principle).

Finally, we conclude by studying how our model may be used to account for discontinuous fibers. The increasing use of Hexcel’s HexMC [2] discontinuous fiber composites (DFC) in the molding of complex structural parts is prompting interest among research engineers. Experimental work by Boursier [2] has pointed out the differences in failure between DFC and CFC. In particular, the theories used for analysis of CFC do not seem to hold for DFC. If this were true, it would be an important exclusion since many variants of DFC are being considered for use in autos and commercial airliners. In this paper, we will show that our model can be adapted to work for DFC.

2 Finite Element Macro Model

In this model, we represent the resin matrix and each fiber layer aligned in a particular direction as a series of parallel elements occupying the same element topology. These components are shown as a schematic in Fig. 1.

Each component is described simply as an isotropic elastic-plastic material. Their individual nonlinear incremental stiffnesses are easily computed by any nonlinear

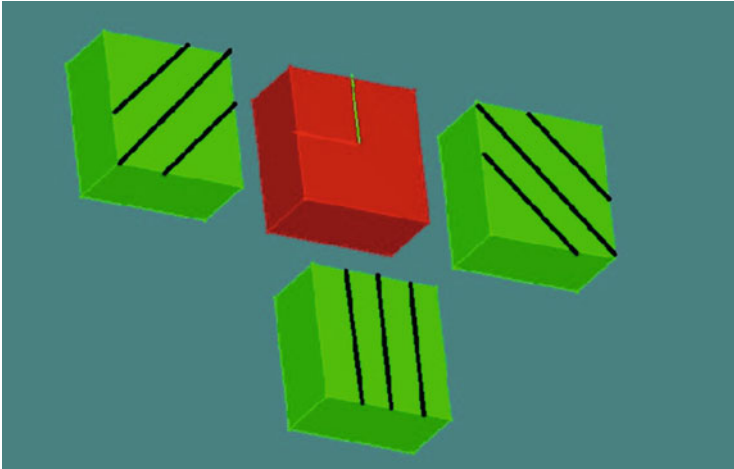


Fig. 1 Schematic showing matrix (*red*) and three fiber components ($+45$, -45 , and 90°)

finite element program. The element stiffnesses contribute to the element topology as a ratio of their volume. In this paper, we use the MPACT program [3] to model the element topology with a 27-node hexa element. Then the element stiffness for the resin matrix assumes an isotropic elastic-plastic behavior, while the fibers are modeled directly as space bars that follow the displacement constraints of the element assumed displacement function. It is conveniently simulated with an anisotropic material behavior where the only significant stiffness lies along the fiber direction. The elastic-plastic material was assumed to behave in an elastic-perfectly plastic manner for an equivalent plastic strain corresponding to five times the strain to first yield. Then it is assumed to fail by micro-cracking. The micro-cracking was assumed to be represented by a negative work-hardening slope equal to 0.2 times the Young's modulus of the respective matrices or fibers. This 0.2 value was chosen because it gave a smooth stable failure mechanism that was thought to represent the strength support being still offered by the surrounding matrix material. Once the element stiffnesses are calculated, the direct stiffness of the displacement method takes over and the FEM follows the usual solution path.

The model has been applied to study fracture of continuous as well as discontinuous fibers. The basic fracture model consists of three layers of planar elements through the thickness. The first layer models the current depth of the initial crack which is usually determined by the transverse butt joints of the layers which may also be staggered (Fig. 2).

In the second layer, the thickness is assumed to be that thickness that the crack propagates through. It is assumed to be equal to the thickness that includes all the fiber directions plus the matrix resin thickness (this is also the layer thickness assumed for the original cracked mesh depth, for convenience). The final layer is the remaining depth for all the rest of the thickness, respectively. The three layers are

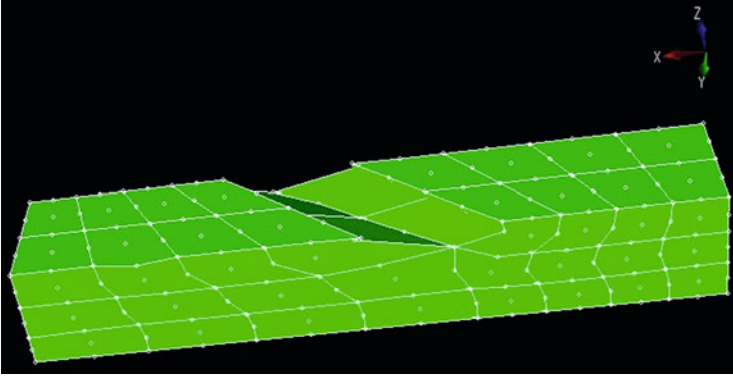


Fig. 2 Deformed first cracked layer (not to scale)

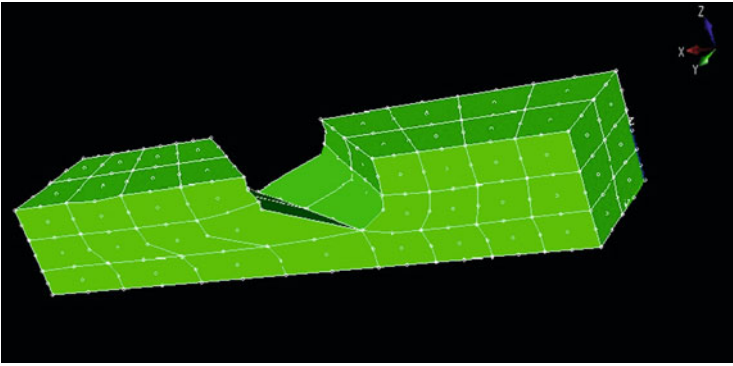


Fig. 3 Deformed second cracked layer (not to scale)

sufficient to determine the fracture load by FEM and classic fracture mechanics. The novelty in our approach is that we use our model to carry out the implied differentiation in the classical theory by a numerical differentiation instead. In the case of discrete fibers, we treated the fibers as being quasi-isotropic with an assumed initial crack depth equal to four thicknesses of fibers and matrix. In our analysis, we assumed a J-integral value of 80 J/mm. This is slightly lower than the value measured in [4]. For our analysis of the fracture of a simple tension specimen, we developed a mesh generator that aligned the mesh in the 45° direction. The experimental specimen did fracture in that direction (Fig. 3).

3 Case Studies with Macro Model

In the following, we demonstrate the versatility of our model by applying it to three classes of problems with their own modes of material failure.

Table 1 Material properties

Material T300/N5028	Tensile stiffness (GPa)	Tensile strength (mPa)
Carbon fiber	220	3000
Poisson's ratio	0.2	
Epoxy	3.25	70
Poisson's ratio	0	
Volume ratios	Each fiber 0.175	Matrix 0.3

In our first case study, we carry out a full nonlinear plane stress analysis with the Macro Model. The results are compared with the numerical results of Tsai [5], where he used a degradation model, which at the time was regarded as a useful model.

We will illustrate this macro-mechanical approach by considering a plane stress composite with carbon fibers in the 0° , $+45^\circ$, -45° , and 90° angle to the x-direction.

To be specific, we will consider a carbon fiber epoxy composite, viz., T300/N5028.

The matrix material is assumed to behave in an isotropic manner. We represent each layer of fiber in a given direction as an anisotropic material with its Young's modulus in the main fiber direction and much reduced values in the other orthogonal directions. Note that the fiber assumption is made because it is the closest representation of a fiber in the MPACT finite element program, even though other programs may have a more convenient model for a given layer of fibers. Similarly the elastic-plastic behavior of the fiber is assumed to follow an isotropic Mises material. At first, the elastic-plastic material is assumed to behave in an elastic-perfectly plastic manner for an equivalent plastic strain corresponding to five times the strain to first yield. Then it is assumed to fail by micro-cracking. The micro-cracking is assumed to be represented by a negative work-hardening slope equal to 0.2 times the Young's modulus of the respective matrices or fibers. This 0.2 value is chosen because it gives a smooth stable failure mechanism that represents the strength support being still offered by the surrounding matrix material. We recall that the Mises plasticity assumption with associated flow rule implies incompressible plastic straining.

Two load cases were studied. The cases were displacement controlled.

The first case is that of uniaxial loading, while the second applies an equally tensile compressive displacement in orthogonal directions, respectively.

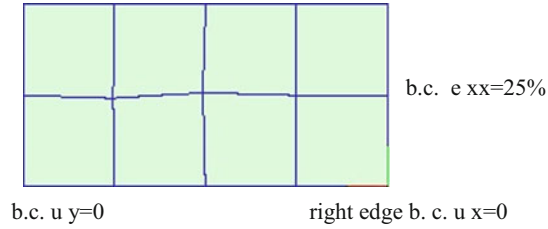
The material properties used are described in Table 1.

4 Details of FEA

Total applied strain in one direction = 25 %.

Incremental analysis with 20 equally spaced time steps.

Automatic controls were set to restrict changes to less than 0.2 % per increment.

Fig. 4 Finite element mesh

Direct sparse matrix solver.

Quadratic 9-node (2D analogue of the 3D quadratic 27-node) plane stress elements were used.

This resulted in a mesh (Fig. 4) with a total of 45 nodes.

Eight elements were used for the matrix.

Eight elements were used for each fiber direction with the same element connectivity as each matrix element, respectively.

Thus, giving 40 total elements.

A python program was developed to easily generate the superimposed element model from a basic one material specimen.

The finite element model is shown below with boundary conditions (b.c.) applied to the respective edge nodes.

b.c. Case 1 undefined e_{yy} , Case 2 $e_{yy} = -e_{xx}$

5 Results, Case 1: Uniaxial Loading

The equivalent stress (sig_equiv) vs. uniaxial strain (e_{xx}) diagram is shown in Fig. 5. The sig_equiv is equal to sig_{xx} in the uniaxial loading case. The results from progressive degradation (Tsai [5]) are also shown.

The sig_{yy} is a small stress induced by the Poisson ratio effect on the 90° fiber. This is given by Fig. 6.

The average equivalent plastic strain is shown in Fig. 7. One of the drawbacks of the superposing model is that it gives average values for all the quantities at the nodes. The actual values for each fiber must be calculated from the applied strain in a separate calculation or output for each element at its integration point. However, the average values do give an indication of the total plastic strains. The inset scaled plastic strain gives a better estimate of the early plastic straining.

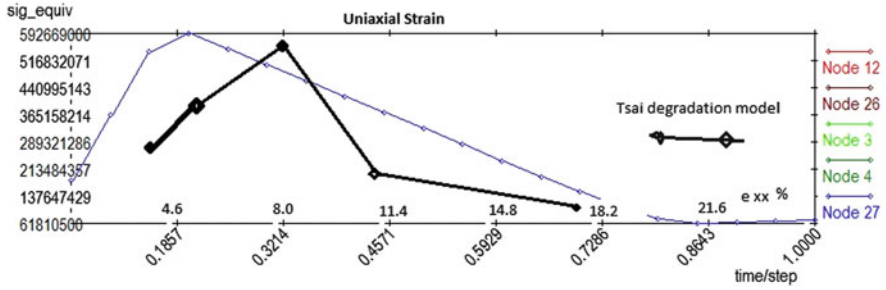


Fig. 5 Equivalent stress (sig_equiv) vs. uniaxial strain (e_{xx})

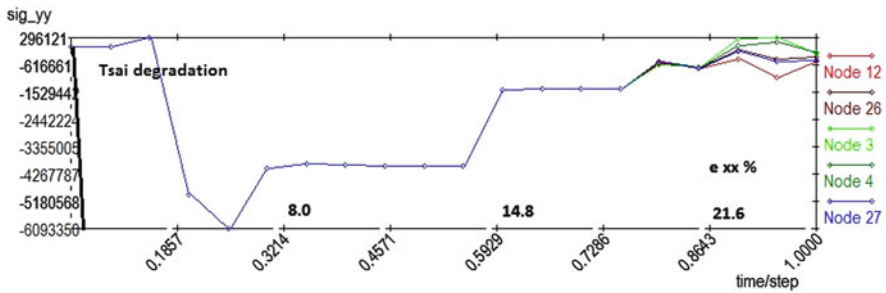


Fig. 6 Transverse stress (sig_yy) vs. uniaxial strain (e_{xx})

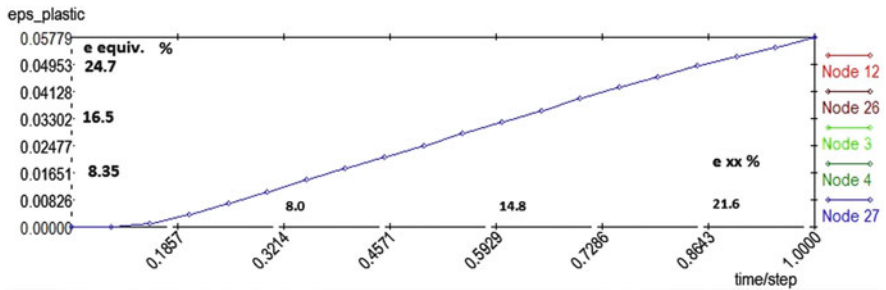


Fig. 7 Equivalent plastic strain vs. uniaxial strain

6 Discussion, Case 1: Uniaxial Loading

The maximum applied stress is shown in Fig. 5. This maximum load agrees with that calculated by Tsai in the Progressive Degradation Model [5].

The diagram for the transverse stress sig_yy gives a good idea of the effect of plastic yielding in the matrix. We note that there is a ratio of about 40 in the yield in stress of the fiber to the matrix. The early plastic straining is all due to the matrix and from the decreased value of the sig_yy shows that the negative work-hardening has already kicked in for the matrix. However, as more strain is applied, the stiffness and

the strength behavior are completely dominated by the fiber composite layers. Note that the maximum average stress of 600 MPa is reached at an early applied strain of about 5.5 % when the negative work-hardening stress for the +45° and -45° fiber layers kicks in and the maximum load starts to decrease. Note that the maximum load is a combination of the strength of the uniaxial fiber with the 45° fibers, and both are in the perfectly plastic regime when the maximum load is reached. However, the choice of the point at which the fiber negative work-hardening kicks in can have an effect on how the composite degrades.

In the light of the above discussion, and because of the dominance of the fiber layers, we conclude that our Macro Model is capable of capturing the most important behavior of the laminate. We also see the value in our selection of the matrix material and its volume ratio since the matrix clearly plays the part of constraining the fiber layers to stay in its original orientation. Recall the incompressibility of the matrix in plastic straining and that the matrix behaves largely in the plastic regime during the entire loading. Because low-cycle fatigue of the matrix is a function of the plastic range, this observation has important ramifications when we consider design for low-cycle fatigue.

7 Results, Case 2: Biaxial Tension and Compression

The uniaxial stress, sig_xx, vs. applied strain is shown in Fig. 8.

The applied load diagram does not differ much from the diagram for the uniaxial loading case. The maximum load is also close to that of the uniaxial case. This flows from our conclusion that the directional behavior of the fiber layers dominates and the fiber layers are disposed symmetrically in terms of the pair 0°, 90° and the pair +45°, -45°, respectively. Each of the fiber pairs bears the e_xx and the e_yy strains, and in the tension compression case, the result is algebraically additive. It can be seen that our model is twice as strong as the Tsai Progressive Degradation Model [5].

The transverse stress, sig_yy, vs. applied strain is shown in Fig. 9.

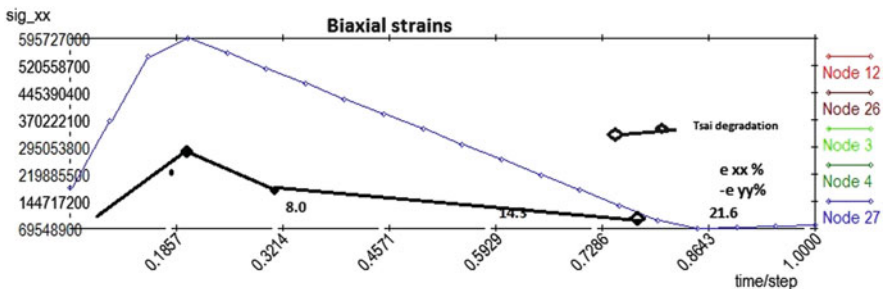


Fig. 8 Sig_xx vs. applied strain (e_xx = -e_yy)

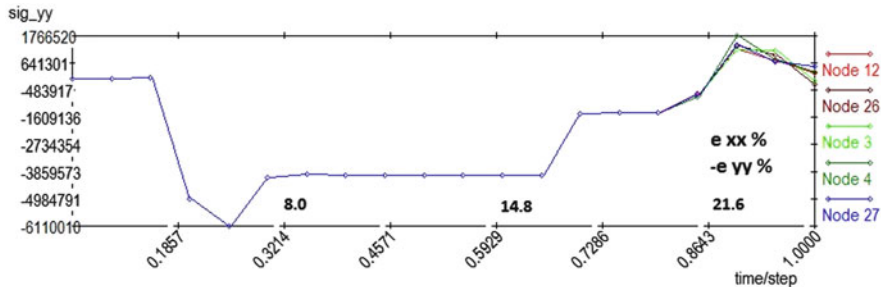


Fig. 9 Sig_yy vs. applied strain ($e_{xx} = -e_{yy}$)

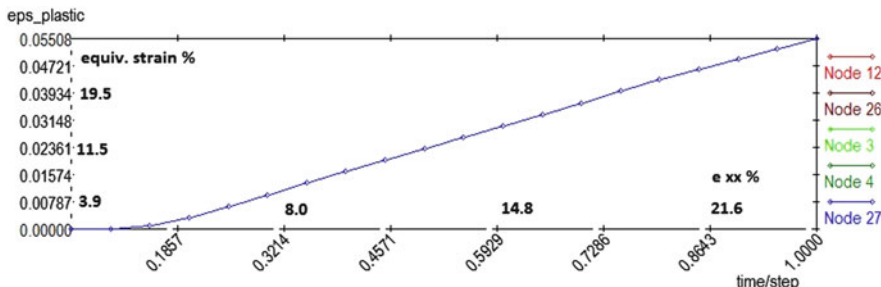


Fig. 10 Equivalent plastic strain vs. applied strain. ($e_{xx} = -e_{yy}$)

In this biaxial stress case, the effect of the tension compression strains is canceling, and we obtain the reduced load in the transverse direction. The maximum transverse stress in the Tsai Progressive Degradation Model was the negative of the maximum in the xx direction (applied load). This showed the difference between the stress and the strain models. However, the differences in the maximum loads are quite significant. The Tsai Progressive Degradation Model does not reflect the dominance of the fiber layers.

In order to complete the picture of the results, we show the average equivalent plastic strains vs. the applied biaxial strains in Fig. 10.

The results for the equivalent plastic strain are the same as those for the uniaxial loading case. The purpose of introducing the above test cases is to establish some experience with the use of our Macro Model. A minimal conclusion here is that the model works and the results are comparable to other results in the literature. In later studies, we will advance arguments as to why the full nonlinear analysis may be preempted by fracture in the case of carbon fibers.

8 Case 3: Biaxial Tests on a C-Ply Laminate

A number of C-Ply (0, +45, -45, 0) tensile specimens were tested by Alan Nettles [6]. The result showed that the transverse strength of the laminate was 1/7th that of the axial strength. The analysis of the axial and transverse aligned tension tests with a 2D macro-mechanical model produced essentially the same maximum loads except that the stiffness of the transverse loading was halved. This result was not consistent with our numerical studies of Cases 1 and 2. So the only possible conclusion to the behavior of the transverse material loading is that there was a fracture. Unfortunately this fracture mode is in the thickness direction, thus necessitating the use of 3D elements. Since the 3D 27-node hexa elements had not been used for fiber composites analysis, it was deemed prudent to carry out a series of unit tests, i.e., tests on a single element.

9 Unit Tests (FEM Analyses on a Single Element)

In order to observe the behavior of our Macro Model, tests were run on a single element with a single fiber layer direction. These tests showed up the weakness in the elements because there was no constraint against rotation of the fiber without strains. In order to impose constraints in our elements, we found that applying plane strain conditions in the two orthogonal directions to the loading was sufficient. This of course imposed a certain degree of inconsistency and is thought to produce a stiffer result. The ideal solution is in fact to develop 3D fiber layers which can then be constrained to move with the 3D hexa element walls. This is a future goal for the MPACT program.

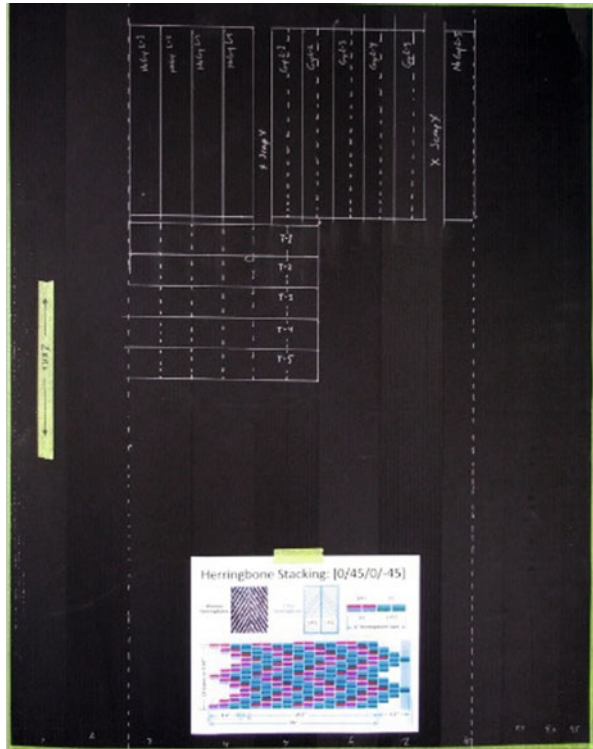
10 Fracture Mechanics Model

The following model was used to represent the progression of the crack. The first layer of the C-Ply (0, +45, -45, 0) is assumed to have cracked at the interface between the +45 and -45 ends and also through the 0, 0 joins (Fig. 2). The second layer of equal thickness (Fig. 3) is then the barrier to the progression of the crack tip. Hence, we develop the load vs. disp at the specimen end for the crack in the first and second layer, respectively. Then the difference in the same load applied to both cases constitutes the work of fracture at the crack tip.

Therefore,

$$J\text{-Int} = -G = -\Delta W / \Delta A \quad (1)$$

Fig. 11 Transverse specimen with staggered seams



where $W = \sum Pu$,
and the crack area = A.

Finally, the third layer of elements represents the rest of the thickness of the C-Ply.

The same material was assumed for layer 2 and layer 3 of the structure.

An analysis was performed for this fracture model. The three layers are shown in Figs. 2 and 3 (not to scale) in the model used to simulate the test.

The transverse specimen used by Nettles [6] is shown in Fig. 11. Because of the fiber in the 0° direction and no fiber in the 90°, the seams in the specimen in the transverse direction were aligned in a staggered manner.

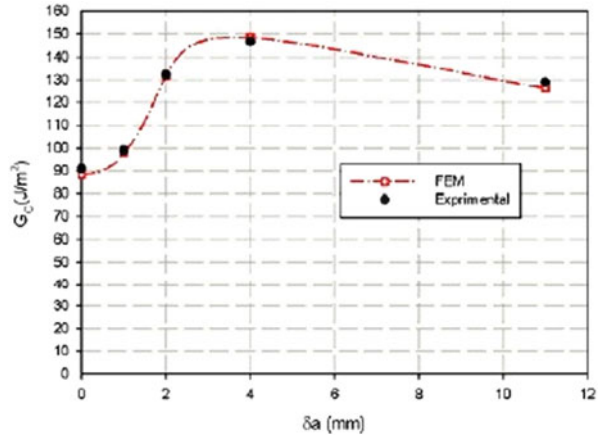
The tests were performed on an IM7 8552 material. The test results are summarized in the following.

11 Tensile Test Results

Longitudinal load, no gap (continuous strips in the axial direction).

Strength 182.3 ± 7.8 KSI (1258 ± 54 MPa), $E = 10.2$ MSI (70.4 GPa).

Fig. 12 J-int for a progressive increase in the size of the initial crack tip



Longitudinal load, gap.

Strength 180.2 ± 11.1 KSI (1243 ± 77 MPa).

Transverse load (always failed at a seam).

Strength 27.3 ± 0.6 KSI (188 ± 4 MPa), $E = 2.54$ MSI (17.4 GPa).

A substitution of numbers into the approximation of the J-int in (1) yielded a value of 80 J/mm.

This may be compared with the results of Mohammed et al. [4] for the (0, 90) ply layers. The result of testing on a compact specimen with a crack is shown in Fig. 12 taken from [4] for an IM7 8552 material.

The starting value of J-int = 90 J/mm was found for $a = 1$. Because of the lower stiffness in the axial direction resulting from the two fiber layers (-45, +45), we expect a lower value of J-int for our model. However, this result shows the value of the Macro Model. The simplicity of the concept and its implementation in the finite element program is a positive for the model.

The simplicity of the C-Ply configuration and the ease in which it is modeled may commend the model as an alternate way of calculating and measuring the fracture toughness of a material. It is worth noting that the results were obtained with a model of 315 nodes and 96 27-node hexa elements. Each evaluation of the model was completed in 30 s on a 4-year-old PC desktop with an I7 Intel chip.

12 Fracture in Sheet-Molded Compound (SMC) Form of DFC

The increasing use of Hexcel’s HexMC DFC in the molding of complex structural parts [2] is prompting interest among research engineers. Experimental work by Boursier [2] has pointed out the differences in failure between DFC and CFC. In particular, the theories used for analysis of CFC do not seem to hold for DFC. If this

What is HexMC[®] material?

HexMC
Material,
(450mm wide
Roll),
~2000 gsm,
~2 mm thick



50mm x
8mm 8552/
AS4 UD
150 gsm,
38% RC,
Controlled
Random
Distribution

Fig. 13 HexMC

were true, it would be an important exclusion since many variants of DFC are being considered for use in autos and commercial airliners.

In the current study, we showed the importance of 3D fracture mechanics in predicting the failure of even simple specimens. We pointed out the difference in our model between fracture of CFC and fracture of homogeneous materials. Fracture initiation occurs along lines of fiber directions where the structural weakness is discernible. This is a necessary part of the analysis since it often differs from the intuitive paths that the loading would suggest. In fact, the necessity of assuming a failure path is so critical that we choose to call it the “Principle of Feasible Failure Paths in FRC” (Feasibility Principle). This Principle is obvious and implied in our previous study of continuous fibers. In the following, we show its applicability in predicting failure in DFC (HexMC).

In Fig. 13, we show the production and composition of HexMC.

Its behavior and uses were described by a presentation by Boursier [2].

The HexMC DFC is made up of plies of fiber chips as shown on the right of Fig. 13. This is idealized in our discussion as randomly placed rectangular chips whose average lengths exceed 25 mm. These chips are arranged in random locations and directions.

13 Theoretical Considerations for Modeling the Failure of DFC

When the fiber reinforcement is discontinuous, we have gaps randomly placed along a specimen. The exact way to account for this is through a Monte Carlo simulation of the additional crack initiators. Such a procedure makes extraordinary demands

on the amount of computing. In our Macro Model, we assume an averaging of this crack initiators, and we assume that its effect is averaged out when we sum it across the cracked and failed section; we refer to this as the Feasibility Principle. Clearly, because of the existence of these cracks due to the discontinuous fibers, we can expect much earlier formation of visible cracks. However, the final failure is determined by cracking through the second layer of material. Here for simplicity, we assume that fracture takes place through continuous fibers. Finally, with all this simplification, we cannot expect a predetermined model as for a continuous fiber model. However, our aim is to assume reasonable initial crack depths and then heuristically determine the optimum parameters by comparison with experiments over a broad selection of specimens.

Boursier [2] showed that the average stiffness properties could be represented by the equivalent quasi-isotropic (QI) laminate with (0, +45, -45, 90) fibers. Here, we also assume that its other mechanical properties are equivalent to those of QI. We assume that cracks form at the edges of a chip.

14 Results of Modeling DFC Failure

Returning to the modeling of the DFC and in line with the Feasibility Principle and consistent with random orientation of the chips, we recognize that we need to combine three chip directions as we move along the cross section of a tension specimen, namely, at 0, 22.5, and 45°, respectively, in any order (this is roughly in line with the observed jagged fracture lines of the experiments in [2]). Here, we assume that we can model individual directions of failure and combine their results without considering the interaction between crack initiations at the join of different angles of chip edges. The building of models to represent DFC is straightforward because we do not need to vary the QI material throughout the specimen.

Again, we use the same three layers to model fracture; Fig. 2 shows the initial layer of a 3D model (not to scale) of an unnotched specimen tested in [2]. The model shows the deformed specimen due to an applied axial average strain. The specimen has dimension of 22.4, 3.8, 0.3 cm. Each chip layer is assumed to occupy 1/6 of the laminate thickness or 0.05 cm. The initial crack propagation is modeled through another 1/6 of the laminate thickness. A second series of analysis were made wherein the starting crack was at the edge of a double chip with the same dimensions. This gave it starting crack depths of 2/6 or 0.1 cm. The analysis assumed that the QI material had a fracture property of $J_{-int} = 80$ kJ/mm. The Macro Model was applied for the analysis of these models. The purpose of our analysis is to show the best combination of initial crack depths in any combination of the crack directions that will reproduce the experimental results. Clearly this is a heuristic value, but because of its repeatability, it is useful in design and analysis. The results are summarized in Table 2.

Table 2 FEA and experimental [2] average axial stress (MPa)

Crack\Av App stressAlign\MPa Degrees	Crack depth unit chip 0.63 cm	Crack depth 2× unit chip 1.26 cm	Combination of two units and one 2× unit 1, 1, 2×	Combination of one unit and two 2× units 1, 2×, 2×
0	451	84	331	208
22.5	442	94.6	331	208
45	470	80	331	208
HexMC experiment [2]	340			
QI FEA	680			
QI experiment [6]	730			

QI quasi isotropic, FEA finite element analysis

15 Discussion of Results of Modeling DFC Failure

The results of the analysis show the importance of selecting a failure path in line with the Feasibility Principle. As it turns out, the results are pretty insensitive to the direction of the assumed crack direction once the crack depth has been finalized. We note that the average stress for crack depth of one unit chip is too high and that of the two chips is too low when compared against the HexMC experimental results. Fortunately, we were able to mix and match the crack depths used because of the insensitivity of the results to the assumed direction of the crack. We note that this was not the case with the CFC analysis because of the alignment of the crack directions with the fiber directions. We note that the results for the 1, 1, 2× crack combinations provided a good match with experiment. The comparison of the QI results was also reasonable, but it is noted that this is a function of the combination of fracture criterion values and the yield strength of the fibers.

The results here uphold the conclusions of [2] that the stiffness modulus is equivalent to the HexMC QI specimens. The results also show the way forward in assuming equivalent representation of the yield strength of HexMC with the QI materials. This saves a large amount of inclusion of statistics in modeling of HexMC and also for any future work with non-chip DFC that is so popular with the auto industry. We were fortunate in being able to select the depth of the crack to achieve a reasonable result. Otherwise, the selection of the appropriate combination of chips would have involved a Monte Carlo simulation of the geometric placement of chips that is beyond the ability of the writer. The insensitivity of the HexMC material to material defects was a major conclusion of [2]. This will be the result of a further study below which would consider the effects of inclusion of defects in DFC and CFC parts.

16 Sheet-Molded Compound-Formed DFC

In the previous section, we addressed the fracture of HexMC DFCs that is now seeing increasing use in the building of secondary structural components in the new commercial airliners [2]. There is an older form of DFC that is made from injection molding. Its fibers are still randomly oriented and often come in SMC form. We shall refer to these as SMC DFC. The SMC DFC is widely favored in the auto industry because of its ease of production and ease of use, usually resulting in greater economy. Qian et al. [7] have carried out tests on SMC DFC tension specimens. Prior to this, the analysis of fracture by FEA for DFC materials involved considerable computing in order to deal with the statistical nature of the randomly oriented short fibers. It appears that the fracture predictions developed here and using the Feasibility Principle can be used directly to predict the results in [7]. The prediction of fracture is dependent on both the strength and the J-integral. This allows us to reexpress our results in dimensionless form with fracture values of the equivalent quasi-isotropic (QI) set equal to 100 %.

17 Theoretical Considerations for Modeling the Failure of SMC DFC

In order to obtain a working model for SMC DFC, we need to assume a depth for the initial crack. In [2] we assumed unit chip thickness and twice that value was used for portions of the HexMC material and obtained reasonable results. It would be reasonable to assume that the same crack depth could be used here. However, because of the uniform random distribution in SMC that does not have the structure of a chip imposed on it by its basic components, it would be reasonable to assume a uniform crack depth throughout the specimen.

As can be seen in Table 3, the experimental results [7] (column 5) are much closer to the FEA results with a starting crack equal to unit depth (column 6) compared to that for the HexMC (column 4).

From this, we conclude that a uniform crack depth assumption is justified for SMC DFC.

18 Case Study of Specimens with Holes as a Notched Specimen

In order to make a start in understanding the impact of notches and other defects that find their way into the final manufactured product, tests were conducted in [2, 7] on holes. Holes can be found everywhere in an assembled complex product. Yet their failure in the presence of flaws is not well understood. They are also an easy

Table 3 Average stress (QI [2] = 100 %) for experiments [2, 7] and FEA

Crack\Av App StressAlign Degrees	Crack depth unit chip 0.63 cm [2] (%)	Crack depth 2× unit chip 1.26 cm [2] (%)	Combination of two 1 unit and 1 of 2× [2] (%)	SMC [7] (%)	SMC crack depth unit thick 0.63 cm [7] (%)
QI experiment [2, 7]	100.00	100	100	100	100
QI FEA	93.10				93.1
HexMC experiment [2]	46.30		45.2		
0	61.70	11.5	45.2	58.3	61.7
22.5	60.50	12.9	45.2	58.3	60.5
45	64.30	10.9	45.2	58.3	64.3

Table 4 Comparison of experiment [7] with FEA for QI and SMC specimens with holes

Hole diameter (cm)	QI experiment [7] (%)	QI FEA (%)	SMC experiment [7]%	SMC FEA (%)
0	100	92.6	63.1	62
3	89.4	85.3	52.6	57.1
5.2	73.6	79.9	44.7	53.5
7	63.1	75.5	44.7	50.2
9.2	58.4	70	44.7	46.9
14	50	58	39.9	39.1

Note The fracture value of the equivalent quasi-isotropic (QI) set equals 100 %

geometry to deal with in a test specimen. The analysis of the presence of a hole in a QI specimen is more complex because it has to deal with the shift from a peak stress at the net cross section to a feasible crack path at 45° to the axial load direction. It is therefore unreasonable to expect a simple net averaging of the results for an unnotched specimen. On the other hand, for the SMC material, we need not expect a shift in peak stress location in order to form a feasible crack path. Therefore, we can expect much better correlation of the fracture predictions for SMC DFC specimens. The results are assembled in Table 4 for such an evaluation. Specimen width = 3.8 cm.

The results in Table 4 have also been plotted in Fig. 14 where the comparisons between theory and experiments can be visualized. A comparison of the results for the QI specimens showed a poor comparison between theory and experiment for the reasons already suggested above (although passable as a first estimate). Therefore, in such cases, it is advised that an analysis be carried out for a QI specimen.

The results for the SMC specimens do provide a reasonable comparison between FEA and experiment.

The use of the results obtained for the HexMC DFC study may be applied here in a simple net-section averaging. It is noted that [7] has indicated that there

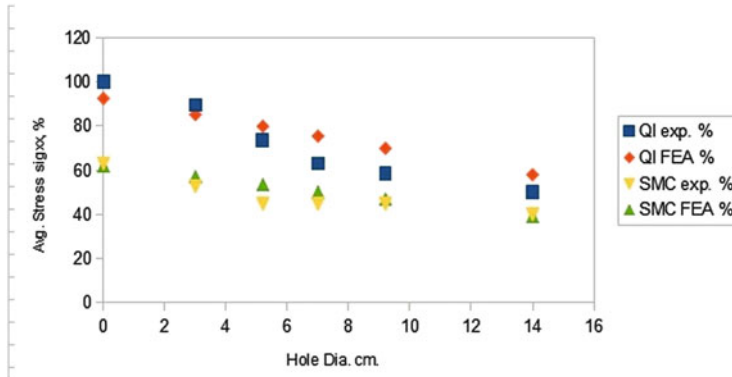


Fig. 14 Average stress at fracture of notched specimens

is considerable scatter in the results for first appearance of surface cracks (non-propagating) because of difficulties in generating a uniform random fiber placement.

Finally, it is a widely held view [2, 7] that the DFC specimens are less sensitive to notch and other flaws when compared to the QI specimens. As we can see from the results in Fig. 14 (and the way it is presented), this is not so. It is just that the initial presence of the cracks in DFC is basically built in and these have a large role in lowering the fracture load. Moreover, nowhere do we see a crossing below of the QI results for CFC with the SMC DFC results.

19 Discussion of All Results and Conclusions

The results of fracture analysis of HexMC already provided insight into the mode of failure of DFC specimens. The main reason for undertaking this study was to obtain an understanding of how to modify the assumptions of the initial crack depth at fracture for the SMC material.

We conclude that the comparisons of Table 4 suggest that it is reasonable to assume a uniform crack depth across the section. This is in line with the target of achieving completely random placement of the fibers.

The second conclusion is that a simple net averaging of the stresses in the cross section provides a good estimate of the fracture of SMC DFC specimens with holes. This encourages us in the expectation that some simple mixing method may be found for the analysis of defects of other types.

The third conclusion is a negative one that the net-averaging methods may not be used for prediction of fracture in QI specimens. However, without the major distraction of DFC materials, such analysis with the Macro Model is easily carried out in minutes on a PC. This may be compared with the multiscale models used, for

example, in Mohamed et al. [4] that required at least two orders of magnitude more in computed times.

Disclaimer Certain commercial equipment, instruments, materials, or computer software is identified in this paper in order to specify the experimental or computational procedure adequately. Such identification is not intended to imply recommendation or endorsement by the National Institute of Standards and Technology, nor is it intended to imply that the materials, equipment, and software identified are necessarily the best available for the purpose.

References

1. Buyukozturk, O., & Marcal, P. V. (1975). *Strength of reinforced concrete chambers under external pressure*. 2nd National Congress on Pressure Vessel and Piping, ASME paper no. 75-PVP-7, June 1975.
2. Boursier, B. (2010). *Failure initiation and effect of defects in structural discontinuous fiber composites*. SAMPE Technical conference 2010, also <http://www.hexcel.com/Innovation/Documents/Failure%20Initiation%20and%20Effect%20of%20Defects%20in%20Structural%20Discontinuous%20Fiber%20Composites.pdf>. [Also see Boursier, B., *Interim presentation to AMTAS*].
3. Nonlinear General purpose Finite Element Program. (1995). *User's guide*. MPACT Corp.
4. Mohammed, Y., Mohamed, K. H., & Hashem, A. M. (2010). Finite element computational approach of fracture toughness in composite compact-tension specimens. *International Journal of Mechanical and Mechatronics Engineering*, 12(4), 57–61.
5. Tsai, S. W. (2008). Strengths of laminates. In S. W. Tsai (Ed.), *Strength & life of composites*. Stanford, CA: Composites Design Group, Stanford University. www.compositesdesign.stanford.edu
6. Nettles, A. (2013). *Results for tests on a C-Ply specimen (0, 45, -45, 90, 0) deg*. Private Communication, January 2013.
7. Qian, C., Harper, L. T., Turner, T. A., & Warrior, N. A. (2010). Notched behavior of discontinuous carbon fibre composites: Comparison with quasi-isotropic non-crimp fabric. *Composites Part A: Applied Science and Manufacturing*, 42(3), 293–302. doi:10.1016/j.compositesa.2010.12.001.

Modeling and SPH Analysis of Composite Materials

Nobuki Yamagata, Yuzuru Sakai, and Pedro V. Marcal

Abstract A number of SPH modeling and analysis examples using medical imaging devices such as computed tomography (CT) scan and MRI have seen an increase in the industrial field. In this study, we propose an image processing technique which can quantize the material properties by brightness value and generate three-dimensional (3D) SPH particle models from the sliced CT/MRI image data of composite materials. In the past, to reconstruct a 3D model by CT/MRI medical images, an unstructured grid approach (polygon) was often used to reproduce the complex geometry. However, this could not represent a solid model. We use CT/MRI medical image brightness to arrange for the initial particle coordinates by voxel method instead of polygon approach in this study. The 3D particle data are generated by using threshold selection by the brightness value. Using the proposed method here, we introduce the two-dimensional (2D) elastic analysis and the 3D elastic-plastic analysis for the carbon fiber-reinforced plastic material using the SPH method. It is concluded that SPH composite material analysis using image processing such as CT/MRI and microscope photographs is convenient for evaluating the composite materials.

1 Introduction

Smoothed particle hydrodynamics (SPH) is a meshless Lagrangian method which is promising as a possible alternative to numerical techniques, which are Finite Element Method (FEM), Boundary Element Method (BEM), and Finite Difference Method (FDM), currently used to analyze high-deformation impulsive loading

N. Yamagata (✉)
SPH Laboratories, Inc., 79-5 Tokiwadai Hodogaya-ku, Yokohama, Japan
e-mail: nyamagata@sphlab.co.jp

Y. Sakai
Yokohama National University, 79-5 Tokiwadai Hodogaya-ku, Yokohama, Japan
e-mail: ysakai@ynu.ac.jp

P.V. Marcal
MPACT Corporation, 6643 Buttonwood Ave., Oak Park, CA, 91377 USA
e-mail: pedrovmarcal@gmail.com

events, such as hypervelocity impact or explosive loading of materials, elastic-plastic analysis, heat transfer analysis, and other various phenomena, Eulerian techniques are considered appropriate for handling the large motions associated with the large deformations; however, detailed analysis is difficult because of the lack of history at the arbitrary positions of the body by using the Eulerian grid. However, Lagrangian techniques are convenient to keep accurate histories of the physical values associated with each Lagrangian particle throughout the whole event.

SPH is the typical Lagrangian technique which is the most popular among several particle methods. SPH is basically an interpolating technique as FDM; however, it is based on kernel integral and the concept of smoothing length which yields the meshless feature to the method. The meshless technique is very convenient to deal with the complicated structures, which is free from the troubles concerning with mesh or grid generation, remeshing, and remodeling.

The basic SPH technique was first introduced by Lucy [1] and Gingold and Monaghan [2] in 1977, and two comprehensive reviews are presented by Benz [3] and Monaghan [4]. More recently, the effect of strength was added by Libersky and Petschek [5] and axisymmetric algorithms were developed by Johnson et al. [6] and Petschek and Libersky [7].

In recent years, researchers have also shown the values of particle methods for elastic analysis [8] and large deformation flow analysis [9]. In the case of drop impact analysis of a structure with complex geometries, it is very difficult to analyze by using mesh-type models. Also in fracture analysis, it is rather difficult to analyze a crack path in the mesh domain because the connectivity of FEM mesh is unable to decide the crack growth direction freely. The authors have confirmed the utility of a particle method for many structural problems [10–13].

A number of SPH modeling and analysis examples using medical imaging devices such as computed tomography (CT) scan and MRI have also seen an increase in the industrial field [14]. And the particle modeling technique for microstructure mechanics of a metal using microscopic photographs and its application examples to 2D elastic wave propagation analysis and 2D Equal-Channel Angular Processing (ECAP) elastic-plastic analysis have been reported in Ref. [15].

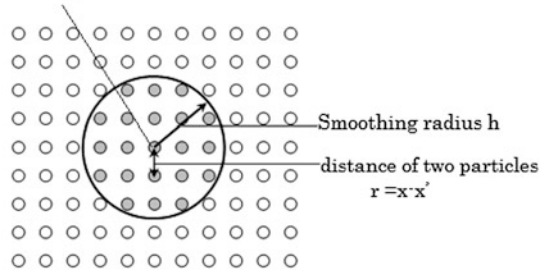
In this study, we introduce the elastic-plastic analysis and fracture analysis of carbon fiber-reinforced plastic material using the SPH method. And it is concluded that SPH composite material analysis using image processing such as CT/MRI and microscope photographs is convenient for evaluating composite materials.

2 Theory of Analysis

2.1 Theory of SPH

The foundation of SPH is one of the interpolation techniques. The equation of motion and the conservation laws of continuum mechanics, in the form of partial differential equations, are introduced into integral equations through the use of an interpolation function (weight function) that gives the estimate of the field variables

Fig. 1 The concept of SPH Evaluation point x



at a point. In numerical process, information is given at discrete points so that the integrals are evaluated as summing over neighboring particles. Figure 1 shows the concept of the SPH method. Consider a function $f(x)$ and a kernel $w(x-x',h)$ which has a radius (support domain) h ; the kernel estimate is

$$f(x) \approx \int f(x') w(x-x',h) dx' \tag{1}$$

As a typical weight function, we employed the spline function of 3° which is usually used in SPH analysis [16]. The approximation for spatial derivatives is obtained by substituting $\nabla \cdot f(x)$ for $f(x)$ in Eq. (1):

$$\nabla \cdot f(x) \approx \int \nabla \cdot f(x') W(x-x',h) dx' \tag{2}$$

In general, physical parameters $f(x)$ in a continuum are interpolated using a weight function, and the discrete kernel estimate and its spatial derivative become

$$f(x) \approx \sum_{j=1}^N \frac{m^j}{\rho^j} f(x^j) W(x-x^j,h) \tag{3}$$

and

$$\nabla \cdot f(x) \approx -\sum_{j=1}^N \frac{m^j}{\rho^j} f(x^j) \cdot \nabla W(x-x^j,h) \tag{4}$$

where m is the mass, ρ is the density of the material, and J is the interpolation points within a support domain. In this study, the elastic-plastic analysis is applied to human head impact against a rigid wall. The acceleration of a particle can be represented as follows using the stress divergence:

$$a = \frac{1}{\rho} \nabla \cdot \sigma \tag{5}$$

where σ is Cauchy stress tensor and \mathbf{a} is acceleration. The acceleration of particle i is obtained as

$$a_i^I = -\sum_{J=1}^N m^J \sum_{j=1}^3 \frac{\sigma_{ij}^J}{\rho^I \rho^J} \frac{\partial W}{\partial x_j^J} \quad (6)$$

The variations of Eq. (6) are sometimes used. By using the stress tensor at point I , Eq. (6) becomes

$$a_i^I = -\sum_{J=1}^N m^J \sum_{j=1}^3 \left[\left(\frac{\sigma_{ij}}{\rho^2} \right)^I + \left(\frac{\sigma_{ij}}{\rho^2} \right)^J \right] \frac{\partial W}{\partial x_j^J} \quad (7)$$

As the above equation, the acceleration of any point in a stress field will be obtained. The interaction between particle I and particle J is equal. That is, the law of conservation of momentum is guaranteed exactly.

The velocity gradient is given using Eq. (4):

$$\left(\frac{\partial V_i}{\partial x_j} \right)^I = -\sum_{J=1}^N \frac{m^J}{\rho^I} V_i^J \frac{\partial W}{\partial x_j^J} \quad (8)$$

and

$$\left(\frac{\partial V_i}{\partial x_j} \right)^I = \frac{1}{\rho^I} \sum_{J=1}^N m^J (V_i^I - V_i^J) \frac{\partial W}{\partial x_j^J} \quad (9)$$

The latter relation has the advantage that the contribution to the strain rate tensor from particles I and J is zero if their relative velocity is zero. As Eq. (9), using the known particle positions and stress to seek acceleration at time, the velocity and position are as follows:

$$V_i^{I,n+\frac{1}{2}} = V_i^{I,n-\frac{1}{2}} + \frac{1}{2} \left(\Delta t^{n+\frac{1}{2}} + \Delta t^{n-\frac{1}{2}} \right) a_i^{I,n} \quad (10)$$

$$x_i^{I,n+1} = x_i^{I,n} + \Delta t^{n+\frac{1}{2}} V_i^{I,n+\frac{1}{2}} \quad (11)$$

The particle density at time t^{n+1} is

$$\rho(x) = \sum_{J=1}^N m^J W(x - x^J, h) \quad (12)$$

The strain rate tensor is obtained by the velocity gradient as the following equation:

$$\dot{\varepsilon}_{ij} = \frac{1}{2} \left(\frac{\partial V_i}{\partial x_j} + \frac{\partial V_j}{\partial x_i} \right). \quad (13)$$

The vorticity tensor is obtained as

$$\omega_{ij} = \frac{1}{2} \left(\frac{\partial V_i}{\partial x_j} - \frac{\partial V_j}{\partial x_i} \right) \quad (14)$$

2.2 Elastic-Plastic Analysis

SPH algorithm for elastic-plastic analysis method has been developed by the authors [12] in the case that strain rate effects are not into account in the elastic-plastic algorithm of the finite element analysis. In the finite element method, the yield judgment is performed at the numerical integration points of the element or the center point of element, while in the SPH method, yield condition is performed for each particle of the model.

The SPH method uses the yield condition which has been applied in the finite element method. A typical expression of the von Mises yield condition is the yield stress of a material.

Elastic-plastic problems always use deformation theory and incremental theory. The SPH method interpolates explicitly, which makes it easy to handle the incremental changes. So the authors use the incremental theory in elastic-plastic analysis too. In the elastic region,

$$\{d\varepsilon\} = \begin{Bmatrix} d\sigma_x \\ d\sigma_y \\ d\tau_{xy} \end{Bmatrix} = \frac{E}{1-\nu^2} \begin{bmatrix} 1 & \nu & 0 \\ \nu & 1 & 0 \\ 0 & 0 & \frac{1-\nu}{2} \end{bmatrix} \begin{Bmatrix} d\varepsilon_x \\ d\varepsilon_y \\ d\gamma_{xy} \end{Bmatrix} = [D_e] \{d\varepsilon\} \quad (15)$$

In the plastic region,

$$\{d\sigma\} = \begin{bmatrix} \frac{E}{1-\nu^2} - \frac{S_1^2}{S} & \frac{\nu E}{1-\nu^2} - \frac{S_1 S_2}{S} & -\frac{S_1 S_6}{S} \\ \frac{\nu E}{1-\nu^2} - \frac{S_1 S_2}{S} & \frac{E}{1-\nu^2} - \frac{S_1^2}{S} & -\frac{S_2 S_6}{S} \\ -\frac{S_1 S_6}{S} & -\frac{S_2 S_6}{S} & \frac{E}{2(1+\nu)} - \frac{S_6^2}{S} \end{bmatrix} \begin{Bmatrix} d\varepsilon_x \\ d\varepsilon_y \\ d\gamma_{xy} \end{Bmatrix} = [D_p] \{d\varepsilon\} \quad (16)$$

and stress-strain equation

$$\sigma_{ij} = D_{ij} \varepsilon_{ij} \quad (17)$$

Using the above equation, the authors can get the stress field.

3 Composite Material Analysis

3.1 Modeling of Composite Material

3.1.1 Generation of Particle Data for SPH Composite Material Analysis

The process of generating particle data in SPH analysis for composite materials using microscope photograph (original image) is described below [15].

As shown in Fig. 2, the original image distributed in each material tissue is represented by the brightness of the bitmap.

And if one particle is replaced with one unit (pixel), it will correspond to a point mass of the material tissue. This is similar to the technique of the finite element voxel method which places the normalized voxel in the space; the particle data just represents the point masses and do not have a mesh structure. That is, the composite material can be modeled as an assembly of the point masses.

However, since the entire image is constructed from the gray scale, if we apply the technique to represent the composite materials by setting the threshold of brightness directly, the boundaries between the resins and fibers of composite materials become ambiguous and then it is difficult to get particle data with high accuracy.

Therefore, in this study, we introduce basic image processing techniques in Sect. 3.1.2 to be able to generate more accurately the particle data of each material tissue.

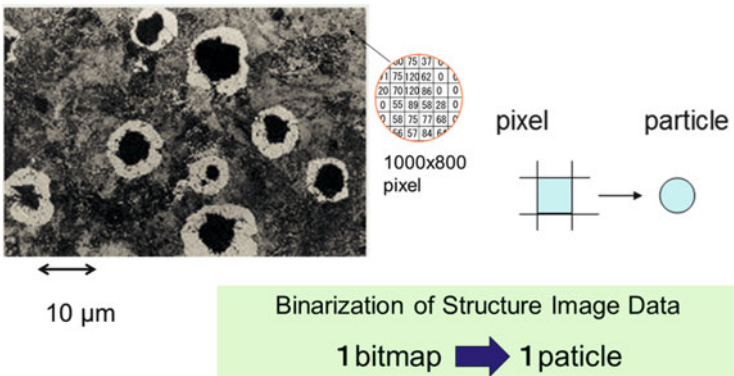


Fig. 2 Micrograph of spherical graphite

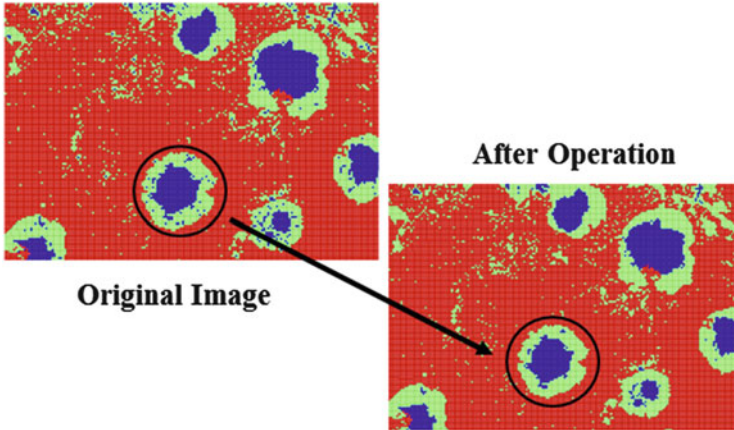


Fig. 3 Cutoff process in the basic image processing techniques

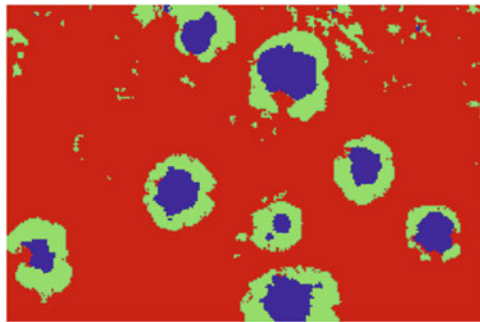


Fig. 4 An example of particle generation

3.1.2 Basic Image Processing Techniques

In order to make the image data resemble the composite material model, the following basic image processing techniques are applied in this study:

1. Cutoff process
2. Dilation and erosion
3. Edge detection

Cutoff is the process of removing the noise data in the image (see Fig. 3). Dilation is the process of replacing it with the white pixels if the white pixels surround the target pixel. On the other hand, erosion is the process of replacing it with a black pixel if the black pixels surround the target pixel. Edge detection is also the process of defining the outline of the image clearly.

Figure 4 shows an example of particle generation for spherical graphite cast iron using this basic image processing technique. It is the particle model which consists

Fig. 5 CT image of a composite material

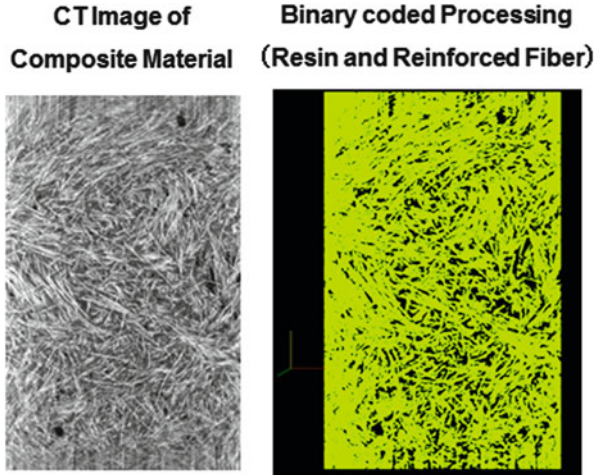
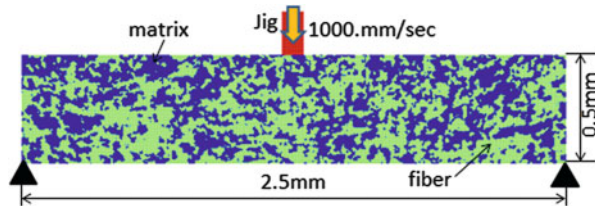


Fig. 6 The analysis model



of spherical graphite, cast iron, and intermediate tissue. The number of particles for spherical graphite, cast iron, and intermediate tissue is 5,253; 25,820; and 4,252, respectively, and the total number of particles is 35,325.

Using the basic image processing techniques, we can also generate the particle data for SPH analysis of composite materials. Figure 5 shows an example of the particle data which is generated from the CT image of a composite material.

3.2 Two-Dimensional Elastic Analysis of Composite Material

First, we have tried to analyze a 2D plain strain elastic analysis of composite material which is constituted from resin and fiber. Figure 6 shows the analysis model in which the composite material is applied by the steel jig with the constant velocity of 1000 mm/s. Using the image processing for composite material which is described in Sect. 3.1, we generate particle data for SPH analysis. Here a total of 50,800 particles with 0.0049 for the distance of two particles are used and the materials' properties in this analysis are shown in Table 1. Figure 7 shows the equivalent von Mises stress distributions of composite material at times of 0.0125 and 0.0625.

The high-stress areas of the composite material increased in accordance with the increase of the time. The maximum deformation at time 0.0625 was 0.01 mm. In

Table 1 Material properties

Material	Matrix	Fiber	Jig
Elastic modulus (Mpa)	100	100,000	210,000
Poisson ratio	0.33	0.33	0.33
Density (kg/mm ³)	1.00E-06	2.68E-06	7.80E-06

Fig. 7 von Mises stress distributions of composite material analysis

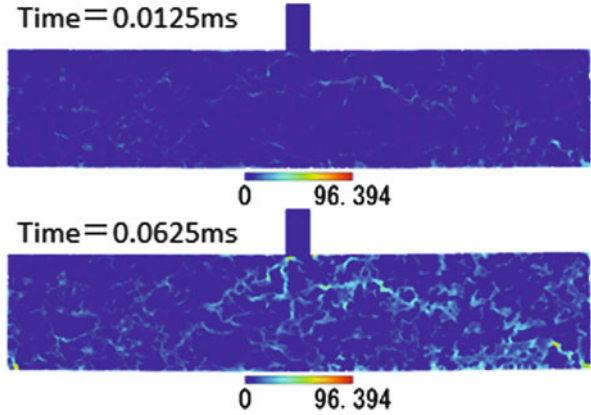
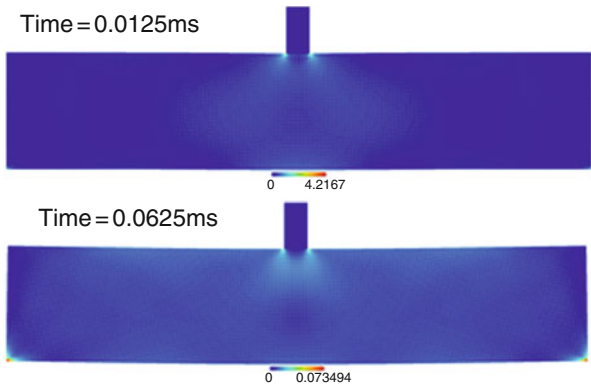


Fig. 8 von Mises stress distributions of resin material analysis



order to evaluate the results in the composite material analysis, we have analyzed the single-material model of resin under the same condition with the case of the composite material model. From the results in Fig. 8, the high-stress areas were given at the fixed points in this analysis; on the other hand, the high-stress area was in the fiber component in the case of composite material analysis.

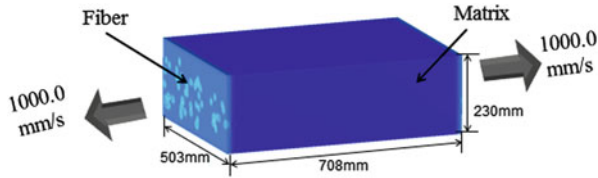


Fig. 9 3D analysis model of composite material

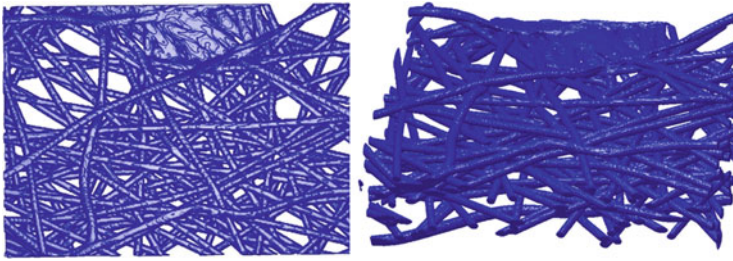


Fig. 10 Fiber model (Left: STL data, Right: Particle data)

Table 2 Material properties of composite material

<i>Material: fiber</i>			
Young modulus	125000.00 Mpa	Yield stress	500.00 Mpa
Hardening (h)	7.3731 Mpa	Poisson R.	0.33
Density	7.0000e-6 kg/mm ³		
<i>Material: resin</i>			
Young modulus	500.00 Mpa	Yield stress	500.00 Mpa
Hardening (h)	7.3731 Mpa	Poisson R.	0.33
Density	1.0000e-6 kg/mm ³		

3.3 Three-Dimensional Elastic-Plastic Analysis of Composite Material

Here we have solved the 3D elastic-plastic analysis of a composite material. Figure 9 shows the 3D composite material model which consists of resin and fiber. The tensile loads are applied at both sides with the constant velocity of 1000 mm/s. In order to generate particle data, we used the Standard Triangulated Language (STL) data for each component of fiber and resin. Figure 10 shows the STL and particle data generated from the STL data of fiber component.

And the material properties of composite material which is used in this analysis are shown in Table 2.

Figure 11 shows the variations of von Mises stress distributions in carbon fibers of a composite material with time. It is shown that the stress increases large along time gradually and the stress distributions are not uniform in the fibers. Apparently,

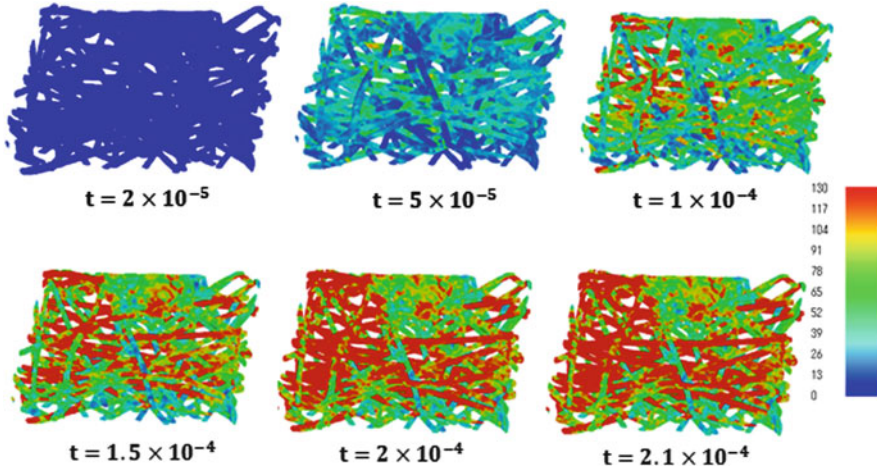


Fig. 11 von Mises stress at the fiber components

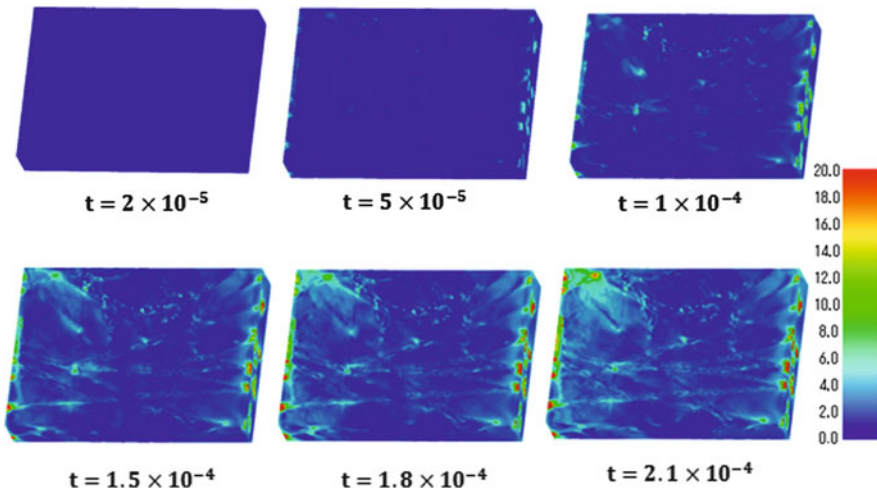


Fig. 12 von Mises stress at the resin components

the stresses are high at the both loaded ends and are relatively low at the center of the structure, where the density of fibers is high. It is clear that the density of fibers is important to strengthen the composite materials.

Figure 12 shows the variation of von Mises stress distributions in a matrix of a composite material. It is shown that the stress of a matrix attached to carbon fibers is high. By comparing Fig. 11 with Fig. 12, we can see that the strength of a composite is completely due to the strength of the fibers because the stress of the fibers is predominantly higher than the stress of a matrix.

Using the SPH method, the details of distributions of carbon fibers in a matrix are modeled by particles, and the elastic-plastic analysis is carried out with high accuracy. Moreover, it is expected that the microvoid between the matrix and fibers and the fracture of fibers and the matrix can be analyzed easily compared to FEM analysis. SPH analysis is very promising in investigating the strength and fracture of composite materials.

4 Conclusions and Further Works

1. SPH composite analysis using image processing such as CT/MRI and microscope photographs is convenient for evaluating the strength of composite materials.
2. Three-dimensional SPH composite analysis shows the details of stress distributions of carbon fibers as well as the matrix with high accuracy.
3. Delamination behavior between the fibers and matrix as well as fracture of matrix and fibers can be simulated using the SPH method and image processing techniques.

References

1. Lucy, L. B. (1977). A numerical approach to the testing of the fission hypothesis. *Astronomical Journal*, 82, 1013–1024.
2. Gingold, R. A., & Monaghan, J. J. (1977). Smoothed particle hydrodynamics: Theory and application to non-spherical stars. *Monthly Notices of the Royal Astronomical Society*, 181, 375–389.
3. Benz, W. (1989). *Smooth particle hydrodynamics: A review*. Harvard-Smithsonian Center for Astrophysics, Preprint 2884.
4. Monaghan, J. J. (1992). Smoothed particle hydrodynamics. *Annual Review of Astronomy and Astrophysics*, 30, 543–574.
5. Libersky, L. D., & Petschek, A. G. (1990). Smooth particle hydrodynamics with strength of materials. *Advances in the Free Lagrange Method, Lecture Notes in Physics*, 395, 248–257.
6. Johnson, G. R., Petschek, A. G., & Stryk, R. A. (1993). Incorporation of an SPH option in the EPIC code for a wide range of high velocity impact computations. *International Journal of Impact Engineering*, 14, 385–394.
7. Petschek, A. G., & Libersky, L. D. (1993). Cylindrical smoothed particle hydrodynamics. *Journal of Computational Physics*, 109, 76–83.
8. Sakai, Y., & Yamasita, A. (2001–2007). Study on the fundamental characteristics of structural analysis by particle method based on SPH. *Japan Society of Mechanical Engineers Series A*, 67(659), 1093–1102.
9. Koshizuka, S., Tamako, H., & Oka, Y. (1995). A particle method for incompressible viscous flow with fluid fragmentation. *Computational Fluid Dynamics Journal*, 4(1), 29–46.
10. Yamagata, N., Sakai, Y., & Marcal, P. V. (2006, July). Elastic-plastic and fracture analysis of mobile phones using SPH. In *Proceedings of ASME PVP*.
11. Kawashima, Y., Sakai, Y., & Yamagata, N. (2006, July). Large deformation analysis by smoothed particle hydrodynamics. In *Proceedings of ASME PVP*.

12. Song, M. S., Sakai, Y., & Yamasita, A. (2002). Elastic-plastic analysis by SPH method: 1st report, small displacement problem in 2-Dim. *Japan Society of Mechanical Engineers Series A*, 68(669), 772–778.
13. Uchibori, C., Sakuyama, S., Sakai, Y., Su-I, T., Watanabe, T., & Yamagata, N. (2014, April). Solder crack simulation using SPH method with sub-modeling technique. In *Proceedings of ICEP*.
14. Sakai, Y., Lu, X., Yamagata, N., & Marcal, P. (2012, July). *Human head impact simulation by SPH method*. WCCM12.
15. Sakai, Y., & Lu, X. (2012, October). Analysis of a micro structure of a metal by SPH method. *Japan Society of Mechanical Engineers*, 15.
16. Swegle, J. W., Attaway, S. W., Heinstein, M. W., Mello, M. W., & Hicks, D. L. (1994). *An analysis of smoothed particle hydrodynamics*. Report No. SAND93-2513-UC-705. Albuquerque, NM: Sandia National Laboratory.